Input Harmonic and Mixing Behavioural Model Analysis

A thesis submitted to Cardiff University in candidature for the degree of:

Doctor of Philosophy

By

James J. W. Bell, BEng.

Division of Electronic Engineering

School of Engineering

Cardiff University

United Kingdom

DECLARATION

This work has not been submitted in substance for any other degree or award at this or any other university or place of learning, nor is being submitted concurrently in candidature for any degree or other award.

Signed……(candidate) Date ……

STATEMENT 1

This thesis is being submitted in partial fulfillment of the requirements for the degree of PHD.

Signed……(candidate) Date ……

STATEMENT 2

This thesis is the result of my own independent work/investigation, except where otherwise stated.

Other sources are acknowledged by explicit references. The views expressed are my own.

Signed……(candidate) Date ……

STATEMENT 3

I hereby give consent for my thesis, if accepted, to be available for photocopying and for inter-library loan, and for the title and summary to be made available to outside organizations.

Signed……(candidate) Date ……

ABSTRACT

This thesis details the necessary evolutions to Cardiff University's HF measurement system and current CAD model implementation to allow for input second harmonic and mixing models to be measured, generated, and simulated. A coherent carrier distribution system was built to allow four Agilent PSGs to be trigger linked, thus enabling for the first time three harmonic active source- and load-pull measurements at X-band. Outdated CAD implementations of the Cardiff Model were made dynamic with the use of ADS' AEL. The move to a program controlled schematic population for the model allows for any type of model to be generated and input into ADS for simulation. The investigations into isolated input second harmonic models have yielded an optimal formulation augmentation that describes a quadratic magnitude and phase dependency. Furthermore, augmentations to the model formulation have to comprise of a model coefficient and its complex conjugate in order to maintain real port DC components. Any additional terms that describe higher than a cubic phase dependency are not recommended as average model accuracy plateaus, at 0.89%, from

the quartic terms onwards. Further model investigations into input and output harmonic mixing of coefficients has been detailed and shows that model coefficient mixing achieves better model accuracy, however, coefficient filtering is suggested to minimize model file sizes.

Finally, exercising the modelling process from measurement to design, a generated source- and load-pull mixing model was used to simulate an extrinsic input second harmonic short circuit, an intrinsic input second harmonic short circuit, and input second harmonic impedance that half-rectified the input voltage waveform with Class-B output impedances. The tests were set up to see the impact of input second harmonic tuning on drain efficiency. Efficiencies of 77.31%, 78.72%, and 73.35% were observed for the respective cases, which are approximately a 10% efficiency improvement from measurements with no input second harmonic tuning. These results indicate that to obtain performances at X-band close to theory or comparable to performance at lower frequencies input waveform engineering is required.

ACKNOWLEDGEMENTS

I would like to give my warmest thanks to my supervisor Professor Paul Tasker. He suffered my short-sightedness and floundering as a first year and through the years was a consistent source of intelligent conversation and an idea hub for inspiration. This man is a true force of nature in academia and it is my hope to, one day, emulate some of his drive and enthusiasm for the frontier of this science.

I am of course incredibly thankful for the financial support from all of my sponsors. The Engineering and Physical Sciences Research Council (EPSRC) and Selex Galileo being the main contributors. Selex must also be thanked for the industrial support that they provided and without their help I would not have had a consistent source of devices and information. In this regard Mesuro must also be acknowledged, as they have provided a commercial proving ground

for my implementation of the Cardiff Model and its surrounding concepts.

Thanks must also be extended to the Cardiff Centre for High Frequency Engineering group as a whole. My time at Cardiff University has only got better the longer I have been there and the years spent as a doctoral candidate were some of the most challenging and most fun. A big thank you to all in the trenches with me and I am sure bright things await all of you. Special mention needs to go to Dr. Randeep Saini and Dr. Simon Woodington, as their help, encouragement and insight into my challenge was tremendously helpful and I'm sure I owe them a pint or two.

Finally, I would like to acknowledge my wife and family. Who have provided perspective and reasoning for the problems that I have had and for their encouragement that spurred my tenacity.

LIST OF PUBLICATIONS

J. J. Bell et al. "Behavioral Model Analysis using Simultaneous Active Fundamental Load-Pull and Harmonic Source-Pull Measurements at X-Band," IEEE MTT-S International. Pg 1-4. 5th Jun 2011.

DOI: 10.1109/MWSYM.2011.5972803

J. J. W. Bell et al. "X-Band Behavioral Model Analysis using an Active Harmonic Source-Pull and Load-Pull Measurement System," Asia-Pacific Microwave Conference Proceedings. Pg 1430-1433. 5th Dec 2011.

R. S. Saini, J. W. Bell et al. "High Speed Non-Linear Device Characterization and Uniformity Investigations at X-Band Frequencies Exploiting Behavioral Models," 77th ARFTG Microwave Measurement Conference. Pg 1-4. 10th Jun 2011.

DOI: 10.1109/ARFTG77.2011.6034552

R. S. Saini, J. J. Bell et al. "*Interpolation and Extrapolation Capabilities of Non-Linear Behavioral Models,*" 78th ARFTG Microwave Measurement Symposium. Pg 1-4. 1st Dec 2011.

DOI: 10.1109/ARFTG78.2011.6183865

V. Carrubba, J. J. Bell et al. "*Inverse Class-FJ: Experimental Validation of a New PA Voltage Waveform Family,*" Asia-Pacific Microwave Conference Proceedings. Pg. 1254-1257. 5th Dec 2011.

OTHER CONTRIBUTIONS

J. R. Powell, M. J. Uren, T. Martin, A. McLachlan, P. J. Tasker, J. J. Bell, et al. "GaAs X-Band High Efficiency (65%) Broadband (30%) Amplifier MMIC Based on the Class B to Class J Continuum," IEEE MTT-S International. Pg 1. 5th Jun 2011.

DOI: 10.1109/MWSYM.2011.5973350

TABLE OF CONTENTS

LIST OF ABBREVIATIONS

1) CAD - Computer Aided Design.

2) IP - Intellectual Property.

3) LUT - Look-Up Table.

4) VNA - Vector Network Analyser.

5) IC - Integrated Circuit.

6) EMT - Electromechanical Tuners.

7) ETS - Electronic Tuners.

8) RF - Radio Frequency.

9) ADS - Agilent's Advanced Design System simulation software.

10) DRC - Design Rule Check.

11) PDK - Product Design Kit.

12) EM - Electromagnetic.

13) VIOMAP - Volterra Input Output MAP.

14) HF - High Frequency.

15) PHD - Poly-Harmonic Distortion.

16) HP - Hewlett Packard.

17) NA - Network Analyser.

18) UHF - Ultra High Frequency.

19) PA - Power Amplifier.

20) DUT - Device Under Test.

21) HB - Harmonic Balance.

22) DWLUT - Direct Wave Look-Up Table.

23) FDD - Frequency Domain Device.

24) MTA - Microwave Transition Analyzer.

25) ESG - Agilent's E-type Signal Generator.

26) LMS - Least Mean Squared.

27) PSG - Agilent's P-type Signal Generator.

28) HCC - High frequency signal generator carrier option.

29) SMA - A type of coaxial connector.

30) PLL - Phase Locked Loop

31) DAC - Data Access Component.

32) AEL - Application Enhancement Language.

33) GaAs - Gallium Arsenide.

34) pHEMT - pseudomorphic High Electron Mobility Transistor.

35) MMIC - Monolithic Microwave Integrated Circuit.

Chapter I
Introduction

Transistors today are designed, based on their application, to efficiently utilise the complex physical mechanisms between the different semi-conductive and conductive regions of the device to the advantage of the user. A satisfactory device geometry producing good electrical behaviour is, however, not converged upon on the first pass and successful processes can often be modified many times in the search for better operation or a new application. This ever changing device process scenario necessitates the usage of modelling to quickly gain an insight as to whether the process is good or not. There are, as a consequence of the many applications for transistors, different modelling processes that require varying measurement system configurations to obtain the data necessary for model calculation or extraction. This chapter will introduce the different modelling branches and discuss their usage before looking at the different measurement strategies associated with device modelling. Computer Aided Design (CAD) and its role in the measurement-to-design cycle will then be outlined followed by a section detailing the thesis

objective. Finally a brief chapter summary will follow for the reader's convenience.

1.1 MODELLING BRANCHES

There are two main umbrella terms that describe all transistor modelling efforts over the past fifty to sixty years; they are small-signal modelling and large-signal modelling.

Small-signal models are linear by virtue of the excitation signals being small in comparison to the nonlinearity of the device. They can be used to characterise the gain, stability, bandwidth, and noise of a device and therefore are a good tool for quickly assessing performance during device process iterations. When compared to large-signal models, they have an advantage in the fact that they are directly calculated, rather than iteratively extracted. Moreover, because small-signal models are inherently linear, simpler mathematics is directly applicable to them. S-parameters are the direct quantities that are measured for the models; however, these can be transformed into many other parameters.

Large-signal models can be further separated into three main branches: physical models, behavioural models, and table-based

models. Physical models, unsurprisingly, are models that are based on the physics of the device. The modelling process builds up a formulaic structure that closely approximates the physical phenomena exhibited by the transistor. However, as transistors over the years have become more complex, theses models take increasing lengths of time to create, hence tend to be utilised on existing devices with unchanging geometry. The most common physics-based models that are currently generated are compact models [1]. However, although compact models analytically approximate the device physics in the I-Q domain they often can become behavioural in nature if applied to specific device responses.

At the basic level, behavioural models attempt to just accurately fit a measured response and are not coupled to any physical interpretation. For example, a mathematical function just required to describe load-pull type measurements. The mathematical function arrived at from the data fitting procedure is key to the success of a behavioural model as its flexibility to application, interpolation accuracy, and ability to extrapolate need to be robust. However, current behavioural models are pushed too far when asked to extrapolate and hence produce erroneous simulation results. In contrast to physical models, behavioural models have no fundamental physics basis; as such they protect Intellectual Property (IP) since the modelling equation reveals nothing about the geometry

of a device. The device's behaviour in certain areas of the Smith Chart can be measured relatively quickly; therefore, behavioural modelling can be used to give detailed information on whether the device process is achieving its goals related to its application. This would be the next step after using small-signal modelling to choose appropriated process iterations for further performance optimization. Current behavioural models trying the establish usage in industry are Agilent's X-parameter model [2] and Cardiff University's Cardiff Model [3].

Table-based models are a type of Look-UP Table (LUT) model that consist of large numbers of device measurements stored in a compact format and indexed against the independent variables or operating conditions, i.e. bias, frequency, and input drive power. Model accuracy with this approach relies on the density of measurement points over the myriad measurement variables combined with the computer simulators ability to interpolate between measurement points. Therefore, if a simulator has no interpolation capabilities then an infinite number of measurement points are needed. The nature of these types of models also means that extrapolation is not possible; hence this functionality is, again, purely reliant on the capabilities of the CAD software. Table-based models can be used much like behavioural models are used in the process testing and design procedures; however, their tendency to rely on the CAD

software for help pushes the focus back to behavioural models for a solution. An example of this modelling technique can be seen in [4].

1.2 MEASUREMENT STRATEGIES

The modelling procedure being used is critical in deciding what measurements need to be performed in order to be able to extract a model. The modelling branches fall into two main types: small-signal, and large-signal. These branches clearly indicate the type of measurements that are being performed.

Small-signal measurements can be performed with Vector Network Analysers (VNAs), which will natively perform the measurements over the frequency bandwidth of the measurement apparatus. Depending on whether the device is fixture mounted or an Integrated Circuit (IC), the measurement system will be set up with either conecterized cables or with probes with bias-Ts for the application of DC. For S-parameters, small-signal measurements are usually performed as a function of bias in order to get performance at different operating conditions.

Large-signal measurements performed for model generation are typically load-pull measurements. Load-pull systems can be realised with impedances created passively, actively, or by using a hybrid combination of active and passive techniques. Passive load

termination is implemented by using either Electromechanical Tuners (EMTs), which rely on horizontal and vertical movement of probes along a transmission line to synthesize the load, or Electronic Tuners (ETs), which rely on electronic circuits that change their matching properties and thus present the matching conditions for the required load [5]. An example of a two harmonic passive measurement system setup is shown in figure 1.

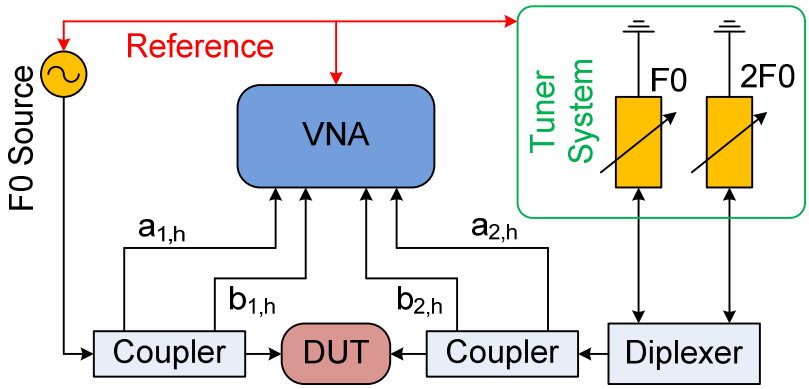

Figure I-1: A two harmonic passive load-pull measurement system.

In contrast, active load termination is achieved by injecting a signal to the output of the device so as to set up the desired a/b condition for the load. For comparison with figure 1, an example of a two harmonic active load-pull system is shown in figure 2. The difference between the two is time taken to converge upon a load. After the initial set-up of passive systems the user would only have to wait for the mechanical action of a tuner or the selection of the right matching circuit, which is relatively fast. Whereas, active systems iterate towards the desired load condition and depending on the

convergence algorithm, this process can be fast, slow, or never converge.

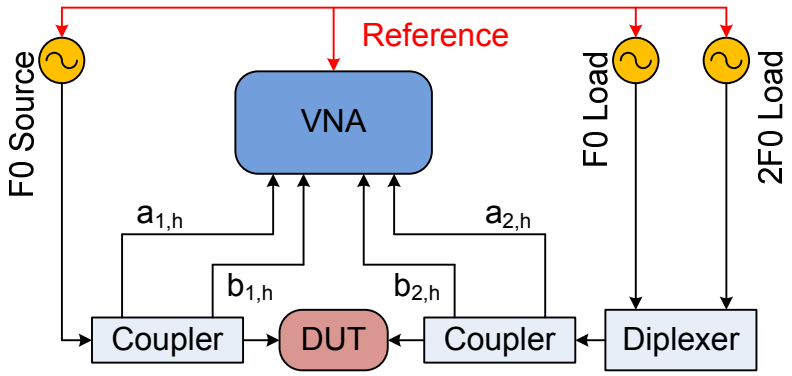

Figure I-2: A two harmonic active load-pull measurement system.

The advantage to having an active system is that for low power devices perfect short circuit and open circuit load conditions can be realised since system losses can be overcome, this is not the case in passive systems. Hybrid systems are used to overcome power issues for active load-pull systems when applied to high power devices. The passive load termination will allow the load to get near the edge of the Smith Chart and the active injection can then iterate out further. For more extensive models to be created, measurements need to be compiled for varying bias, frequency, input drive power, and temperature. Data sets over all of these operating conditions would be collected over time from a series of measurements rather than one exhaustive measurement.

1.3 COMPUTER AIDED DESIGN

CAD certainly has its place in the circuit design area of Radio Frequency (RF) and microwave engineering. Increasing complexity of the circuitry used to enable wireless communication over the years necessitated the development of early circuit simulators. The first available circuit simulator being the SPICE (Simulation Program with Integrated Circuit Emphasis) package developed at the University of California, Berkeley [6]. Since the seventies, the program has been modified and transferred to a new programming language, however, currently there are two more prolific microwave circuit simulators; Agilent's Advanced Design System (ADS) [7] and AWR's Microwave Office [8]. ADS and Microwave Office are competing simulation platforms that offer linear and nonlinear circuit simulation Design Rule Checking (DRC) and can import Process Design Kits (PDKs) from foundries. They also offer Electromagnetic (EM) analysis, which can be used to bolster results from circuit simulation for on wafer amplifiers.

1.4 THESIS OBJECTIVE

The objective of this thesis is to develop the framework for input and output harmonic behavioural modelling and provide the necessary modifications to existing measurement systems and CAD implementation solutions to enable an X-band measurement-to-CAD cycle. The limits, applicability, and implications of input/output

mixing models should be analysed and discussed. The thesis should also look to overcome exhaustive measurements by effectively covering device impedance spaces of interest, for Class-B to Class-J amplifiers, with source- and load-pull points therefore reducing the time needed for the measurement of the input and output behavioural models.

1.5 CHAPTER SUMMARY

This thesis details the analysis of input second harmonic behavioural models in isolation and the mixing necessary for input and output models up to the second harmonic. The measurement system and CAD implementation improvements necessary for the measurement and analysis of the models have been included. The following is a chapter-by-chapter summary of the contents.

Chapter II presents a literature review of the behavioural modelling techniques that have been employed in the past and present. Specifically mentioned and discussed are: S-parameters, Volterra Input Output MAP (VIOMP), hot S-parameters, X-parameters, and the Cardiff Model.

Chapter III outlines the creation of a bespoke coherent carrier distribution system; a necessary addition to the current High Frequency (HF) measurement system in order to perform source- and load-pull measurements.

Chapter IV details the improvements made to the CAD implementation of the Cardiff Model. It shows how the implementation was moved from a static power series equation concerning two output harmonics to a dynamic CAD solution able to manage any model measured over three harmonics on the input and output.

Chapter V contains the analysis of the input second harmonic models. The correct process for augmenting model formulations is highlighted before isolating an input second harmonic source-pull sweep and ascertaining its optimal coefficients in line with the augmentation process. Input and output mixing models are then examined for both input second harmonic and output fundamental measurement source- and load-pull sweeps, and input and output second harmonic source- and load-pull sweeps. Due to the large number for coefficients that can arise from mixing models, the methods for truncating model coefficients are discussed and advantages highlighted. Finally, the design and measurement implications resulting from performing input second harmonic source-pull sweeps are discussed.

Chapter VI concludes the thesis work before offering interesting suggestions for future efforts in this vein of transistor behavioural modelling.

1.6 REFERENCES

[1] J. B. King and T. J. Brazil, "*Equivalent Circuit GaN HEMT Model Accounting for Gate-Lag and Drain-Lag Transient Effects,*" IEEE Topical Conference on Power Amplifiers for Wireless and Radio Applications (PAWR). Pg 93-96. Jan. 2012.

[2] J. Verspecht and D. E. Root, "*Polyharmonic Distortion Modelling,*" IEEE Microwave Magazine, Volume 7. No. 3. Pg 44-57. Jun 2006.

[3] P. J. Tasker and J. Benedikt, "*Waveform Inspired Models and the Harmonic Balance Emulator,*" IEEE Microwave Magazine. Pg 38-42. Apr 2011.

[4] H. Qi, J Benedikt and P. J. Tasker, "A Novel Approach for Effective Import of Nonlinear Device Characteristics into CAD for Large Signal Power Amplifier Design," IEEE MTT-S International Microwave Symposium Digest. Pg 477-480. 2006.

[5] F. M. Ghannouchi and M. S. Hashmi, "*Load-Pull Techniques with Applications to Power Amplifier Design,*" Springer Series in Advanced Microelectronics 32. Pg. 29-30. 2013. ISBN: 978-94-007-4460-8

[6] L. W. Nagel and D. O. Paderson, "*SPICE (Simulation Program with Integrated Circuit Emphasis),"* Memorandum No. ERL-M382, University of California, Berkeley, Apr. 1973.

[7] Agilent Technologies, "*Advanced Design System ADS Home page,*" Downloaded from: http://www.home.agilent.com/en/pc-1297113/advanced-design-system-ads?nid=-34346.0&cc=GB&lc=eng

[8] AWR a National Instruments Company, "*Microwave Office Home page,*" Downloaded from: http://www.awrcorp.com/products/microwave-office

CHAPTER II
LITERATURE REVIEW

Mathematical modelling of any system is a useful and long term way to reduce the cost of, and perhaps eliminate, experimental prototyping. Diminishing the need for prototyping is attractive for small and large business alike, as employee time can be better spent designing with simulators, and the costing for prototype evolutions becomes unnecessary. It is therefore understandable that there has been a push in the modelling area, to make models more accurate, robust and integrate seamlessly with various CAD packages. In the RF and Microwave industries there have been many types of modelling that have been used, in the case of behavioural models, a short list would surely contain the following approaches: S-Parameters, Poly-Harmonic Distortion (PHD) modelling, X-Parameters and S-Functions, and more recently, the Cardiff Model. This chapter will address the aforementioned modelling approaches and assay their qualities. Where appropriate, the paradigms mentioned above

will be dealt with together. This is because there is significant overlap of theory, as early concepts spawned the later solutions.

2.1 S-PARAMETER MODELLING

S-parameters initially developed because of ambiguities arising from the concept of impedance when applied to microwave circuits [1]. This occurred when the wavelength of the operating signal became comparable to the size of the circuit components; hence inconsistencies in scalar voltage and current could be seen in sections of circuitry. This gave rise to the use of transmission line theory applied to microwave circuits, hence the travelling a-b waves and scattering coefficients, or S-parameters, were used.

2.1.1 S-Parameter Theory

Although S-parameters have been seen to be mentioned as far back as the 1920's it was not until the late 60's that they were popularized. This, in part, was due to Hewlett Packard (HP) releasing their HP8410A Network Analyser (NA) which applied the S-parameter theory from [2] in their Hewlett-Packard journal [3]. The theory in [2] defines the scattering waves as follows:

$$a_i = \frac{V_i + Z_i I_i}{2\sqrt{|Re\,(Z_i)|}} \qquad b_i = \frac{V_i - Z_i^* I_i}{2\sqrt{|Re\,(Z_i)|}} \qquad \text{(II-1 \& 2)}$$

Where 'i' indicates the port index, (*) indicates the conjugate, and $Re(Z_i)$ indicates the real component of the complex impedance Z_i. The ratio of the two scattering waves is then defined as the following:

$$S_{i_b i_a} = \frac{b_i}{a_i} \qquad \text{(II-3)}$$

Where subscripts 'i_b' and 'i_a' denote the respective 'b' and 'a' port indices. This is for one port analysis and does not take into account harmonic effects, however one must note that this work treats the scattering a-b waves as being in the frequency domain, hence they can have both port and harmonic indices when applied to non-linear systems (e.g. $a_{p,h}$). Extending these fundamentals in relation to a two

$$\begin{bmatrix} b_1 \\ b_2 \end{bmatrix} = \begin{bmatrix} S_{11} & S_{12} \\ S_{21} & S_{22} \end{bmatrix} \times \begin{bmatrix} a_1 \\ a_2 \end{bmatrix} \qquad \text{(II-4)}$$

port network, the equation below can be written:

Equation 4 is an important result as it allows for two port measurement analyses, whilst also being the backbone of early linear and non-linear device modelling [4-5]. The work performed in [4]

highlights the use of bias dependent small-signal S-parameters in calculating equivalent circuit component values for a F.E.T device. Whereas [5] extends the design techniques for use with small-signal S-parameters to large-signal S-parameters and successfully utilizes them in the design of a Class-C Ultra High Frequency (UHF) Power Amplifier (PA). In the case of [5] it has to be noted that the selectivity of the device's package parasitic network meant that the observed waveforms were nearly sinusoidal in Class-C operation, hence had negligible harmonic components, and could be considered reasonably linear. Normally, the small conduction angle of Class-C amplifiers results in an over-half-rectified output voltage waveform, which has considerable harmonics. Although this is a specific case where large-signal S-parameters have been used in amplifier design the methods do not exactly translate to other amplifier modes. The two practices, previously mentioned, were commonplace in amplifier and mixer design and the use of the small-signal linear parameters in describing systems in the seventies and eighties was abundant.

2.1.2 Measurement of S-Parameters

This will be discussed whilst only considering two port active devices, as these are the types of systems that resemble transistors operated as amplifiers or oscillators. These concepts can easily be extended to multi-port systems, in fact many current VNAs provide for multi-port S-parameter measurements.

The forward and reverse VNA measurement scenarios are shown in figures 1 and 2. The forward measurement should be performed with matched source and load impedances to ensure there is no reflection a_2 from the terminated port 2. Using this measurement S_{11} and S_{21} can be computed using the following formulas:

$$S_{11} = \left.\frac{b_1}{a_1}\right|_{a_2=0} \qquad S_{21} = \left.\frac{b_2}{a_1}\right|_{a_2=0} \qquad \text{(II-5 \& 6)}$$

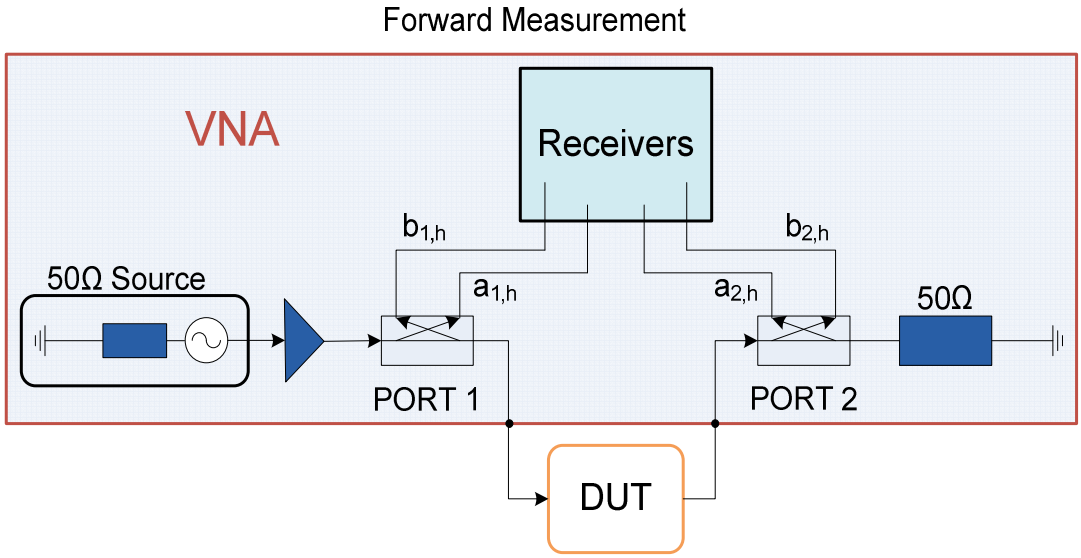

Figure II-1: A 2-port forward VNA measurement on a DUT.

The reverse measurement should also be performed with matched source and load impedances, this time, to ensure that there is no reflection a_1 from the terminated port 1. This measurement enables S_{22} and S_{12} to be computed by the use of the following:

$$S_{22} = \frac{b_2}{a_2}\Big|_{a_1=0} \qquad S_{12,h} = \frac{b_1}{a_2}\Big|_{a_1=0} \qquad \text{(II-7 \& 8)}$$

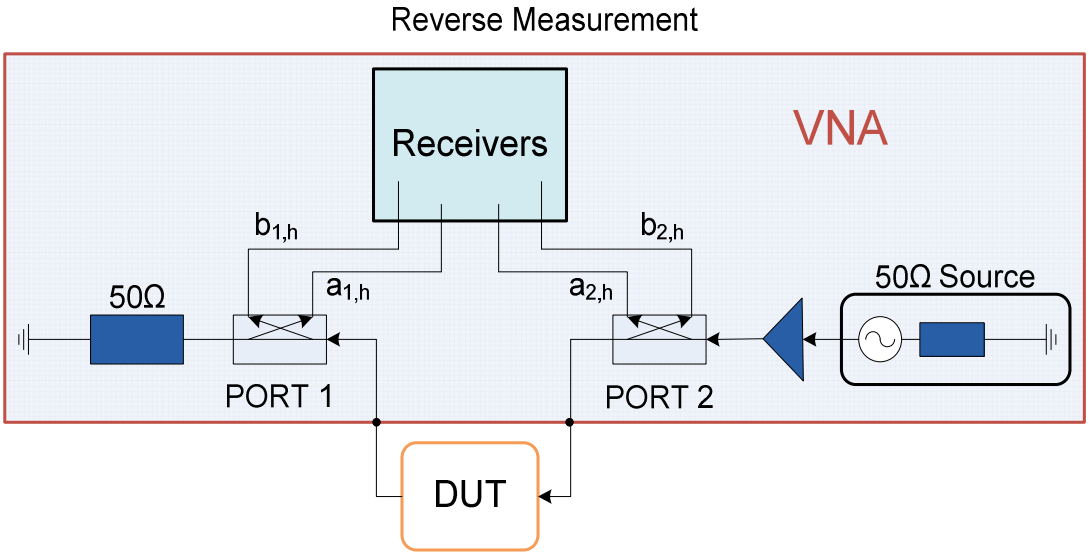

Figure II-2: A 2-port reverse VNA measurement on a DUT.

Usual S-parameter measurements are small-signal, bias dependent and swept over frequency. Since the measurements alone get the required quantities for the aforementioned quotients there is no need for a further extraction process.

2.1.3 S-Parameter Discussion

The S-parameter modelling approach certainly has its advantages with respect to linear systems and in some specific ways can be used with non-linear devices. However, S-parameters are formulaically linear and despite certain modifications and extrapolations there is

no getting away from this fact. Harrop and Claasen [4] show the usefulness of S-parameters when attempting to extract an equivalent circuit model, however there were still some non-linear components left un-described and the effort made by Leighton et al. [5], with large signal S-parameters showed their selectivity to applications, hence their significant limitations as a non-linear modelling solution. With that said, the modelling community sought to rectify behavioural modelling issues in the nineties by introducing the Hot S-parameter, PHD and X-parameter concepts, but before addressing these solutions the VIOMAP concept needs to be introduced [6-9].

2.2 VOLTERRA INPUT OUTPUT MAP MODELLING (VIOMAP)

The VIOMAP provides an extension to S-parameters for use with weakly nonlinear RF and microwave devices, as seen in [6]. It deals with nonlinearities in terms of signal harmonic mixing in relation to the chosen, or observed, degree of system nonlinearity. Previous work has shown that VIOMAPs can be measured like S-parameters, are able to predict the behaviour of cascaded systems [6], can be used to enhance prediction of spectral regrowth and predistortion [7], can be used to reduce conventional load-pull time and predict gain contours over the whole Smith Chart [8], and by substituting VIOMAPs for orthogonal polynomials the concept can be applied to stronger device nonlinearities [9].

2.2.1 VIOMAP Theory

[6-9] consider the Device Under Test (DUT) from a black-box perspective where the system responses $b_{p,h}$ are a product of its inputs $a_{p,h}$ and the systems transfer function H, as displayed in figure 3. The 'a' and 'b' quantities have subscripts denoting port and harmonic index respectively.

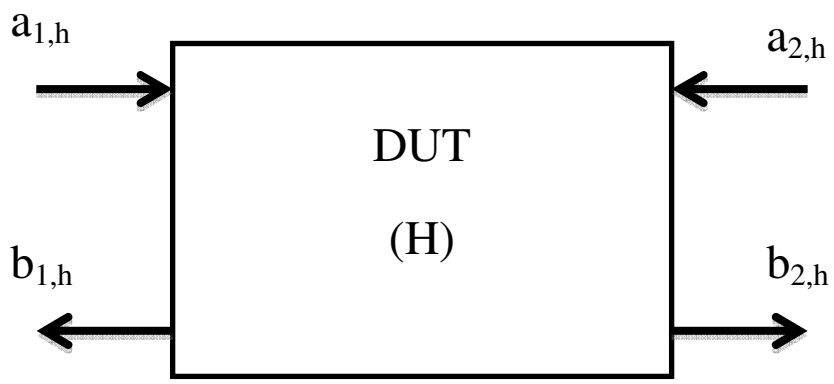

Figure II-3: A two-port device and system representation. H represents the system's transfer function and subscripts h represents harmonic index.

The system transfer function 'H', termed VIOMAP kernel in [6], is defined as: $H_{n,ji1,i2...in}(f_1,f_2,...,f_n)$ related to a fundamental frequency f_0, where j is the input port, 'i' is the output port and 'n' is the n^{th} degree of system nonlinearity. Here 'H' has the argument of frequency. Hence the output is a summation of all relevant products of 'H' and 'a' with respect to harmonic frequency. Although the VIOMAP transfer function 'H' is a lot like the S-matrix in equation 4 it is not

limited to two terms. Verbeyst an Bossche [6] make the observation that when a system is linear the first order VIOMAP kernel is the same as S-parameters, notwithstanding the difference in notation.

The VIOMAP solutions all use Volterra theory; however, none of the papers detail the inner workings of the models and the generation of the polynomials. The underlying time-domain Volterra theory will now be covered. Starting with the Volterra series of N^{th} degree:

$$y(t) = \sum_{n=1}^{N} \int_{-\infty}^{\infty} H(\tau_1, \dots, \tau_n) x(t-\tau_1) \dots \dots x(t-\tau_n) d\tau_1 \dots d\tau_n \quad \text{(II-9)}$$

If $H_n(t_1,\dots,t_n) = a_n\delta(t_1)\delta(t_2)\dots\delta(t_n)$, the power series would be obtained:

$$y(t) = a_1 x(t) + a_2 x(t)^2 + \cdots + a_N x(t)^N \quad \text{(II-10)}$$

The VIOMAP solution is obtained when the chosen order of polynomial N is large enough that the polynomial approximates the nonlinear system. The difference between the above equations and the ones that would be employed in [6-9] is that they operate in the time domain and the measured travelling waves have arguments of frequency. The formulation examples in [6-9] clearly show the

Volterra series summation of signal component powers, mirroring the process in equation 10.

2.2.2 Measurement of VIOMAPs

The measurement scenarios in [6-9] detail different measurement equipment configurations; this is due to measurement being tailored to the specific modelling application and the apparent lack of equipment. The measurement solution in [8] represents a load-pull system, which is the same as approaches that will be presented later on in this chapter, so it shall be used as an example of the type of measurement setup necessary for VIOMAP measurement. The determination of a two port device's VIOMAP requires measurements that exercise the device the desired impedances, e.g. load-pull. Fundamental output load-pull behaviour is being explored in [8], hence a measurement system is required that can stimulate a DUT at both input and output ports simultaneously at the fundamental frequency. In their case a single source is used to achieve phase coherence, however, the same can be achieved with active load-pull measurement systems that use two phase coherent sources.

The measurement system in Figure 4 [8] is based around the HP8510B Network Analyzer [10] and a HP8515A [11] S-parameter test set. The measurement sequence for load-pull was not rigorous.

The model was calculated from a set of 100 impedance points acquired over a range of powers from -7dBm to 8dBm. Each time the power level was changed the variable attenuator and line stretcher, governing the position of the load impedance, were set randomly a few times.

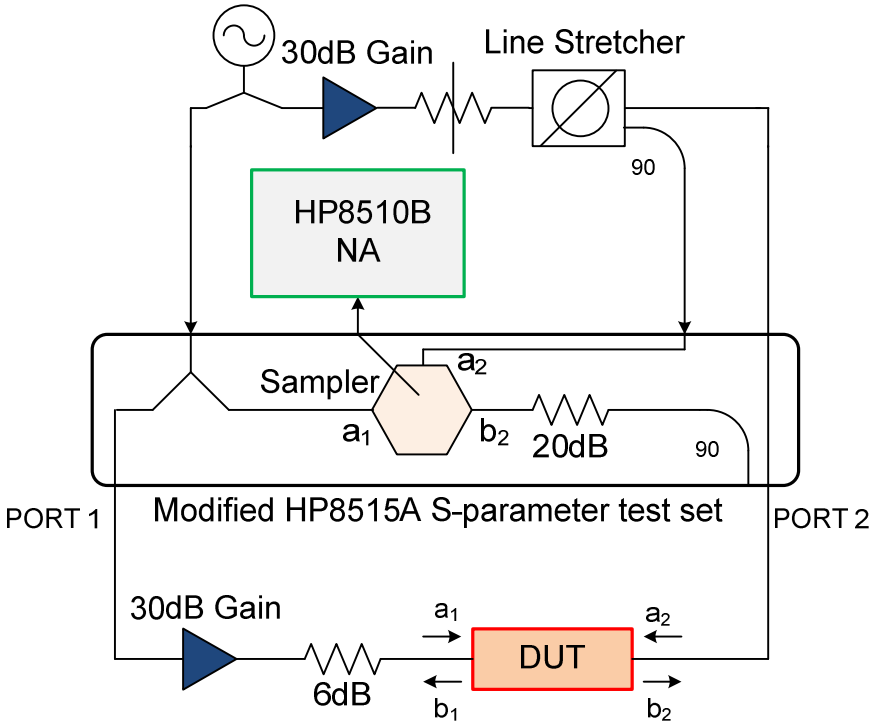

Figure II-4: The block diagram of the measurement setup for fundamental load-pull and VIOMAP determination [8].

A VIOMAP was extracted from the measurements that required a 5th order polynomial to describe the distortion of the output fundamental tone as a function of the separate input powers at port 1 and port 2. Another 3rd order polynomial was also required to describe the

distortion of the output fundamental tone as a function of a combination of the input powers at ports 1 and 2 [6]. The model comprised of 10 coefficients and was sufficient to model the load-pull measurement data, with modelled and measured power plots differing within 0.2dB.

2.2.4 VIOMAP Discussion

The VIOMAP solutions proved promising. However, they were not widely accepted in the RF and microwave design community as a valid solution to the modelling problem. This is possibly because, although theoretically sound, there were issues with the understanding of the selection of the VIOMAP polynomials, as this was not intricately detailed. Also, the practicalities of the advanced extraction procedures are questionable. Furthermore, despite the sound theory [12], there were problems with the overly complicated computation necessary for the orthogonal polynomial approach [9], which was necessary for characterization of devices operated in their strongly non-linear regions. The approach, however, does have a lot of similarities with the Hot S-parameter, X-parameter, and Cardiff Model approaches, notwithstanding the fact that these approaches are formulaically simpler and this may explain why they are perhaps more favourable to the measurement-design scenarios of today.

2.3 HOT S-PARAMETER MODELLING

Hot S-parameters, also known as large-signal S-parameters, allow for a black-box frequency domain behavioural model that protects intellectual property. The technique is derived from S-parameters; however, the S-parameter type measurements are performed when the device is being actively stimulated.

2.3.1 Hot S-Parameter Theory

The work in [13] quite nicely surveys the hot S-parameter works of the time. It shows how hot S-parameters were applied to predicting stability and distortion. The two applications use a variant of the S-parameter matrix equation in section 1:

$$\begin{bmatrix} b_1(f_{s/c}) \\ b_2(f_{s/c}) \end{bmatrix} = \begin{bmatrix} hotS_{11} & hotS_{12} \\ hotS_{21} & hotS_{22} \end{bmatrix} \begin{bmatrix} a_1(f_{s/c}) \\ a_2(f_{s/c}) \end{bmatrix} \quad \text{(II-11)}$$

The difference in the above equation is that the scattering wave quantities 'a' and 'b' have the argument of frequency. The frequency subscript 's/c' is meant to deal with the stability and distortion variants of equation 11, which have exactly the same formulation. The equation only containing subscript 's' is used for stability calculations, as this is the frequency at which the hot S-parameter

stability measurements are being performed. In [14] the argument of frequency (f_S) is swept from 300MHz to $F_0/2$, where F_0 is the fundamental frequency that a_{11} is set to. This changes equation 11 to that of a conversion matrix [14]:

$$\begin{bmatrix} b_1^*(KF_0 - f_s) \\ \vdots \\ b_1(f_s) \\ \vdots \\ b_1(KF_0 + f_s) \\ b_2^*(KF_0 - f_s) \\ \vdots \\ b_2(f_s) \\ \vdots \\ b_2(KF_0 - f_s) \end{bmatrix} = [S] \begin{bmatrix} a_1^*(KF_0 - f_s) \\ \vdots \\ a_1(f_s) \\ \vdots \\ a_1(KF_0 + f_s) \\ a_2^*(KF_0 - f_s) \\ \vdots \\ a_2(f_s) \\ \vdots \\ a_2(KF_0 - f_s) \end{bmatrix} \quad \text{(II-12)}$$

In equation 12 the [S] matrix contains the hot small signal S-parameters and relates the [a] and [b] matrices at the frequencies ($KF_0 \pm f_S$) at each of the swept perturbation frequencies f_S, where K is the harmonic multiplier. If it is assumed, for a system with fixed drive and bias levels, that there are known constant terminations at the F_0 and ($KF_0 \pm f_S$) frequencies it is possible to concentrate on the input and output probing waves at the swept frequencies f_S and the equation reduces again to that shown in equation 11. Stability assessments are undertaken in the same way as with S-parameters

and are centred around the calculation of the relevant 'hot' stability parameter(s).

The subscript 'c', in equation 11, applies when it is concerning the prediction of system distortion characteristics. In this variant, the energy of the system is only expected in the fundamental frequency and harmonic signal components, therefore the interaction between the a-b scattering waves can be viewed in the limited frequency set defined by $k.f_C$, where k is a positive integer that reflects the harmonic number. This can be done because there are a few assumptions that are taken into account: the application is for narrowband use, hence the input signal is thought of as a one-tone carrier that can be modulated by a frequency less than the carrier frequency; the DUT is being operated at near matched conditions, consequently, signal energy is expected at the fundamental and harmonic frequencies only.

The different subscripts for frequency in equation 9 naturally highlight, in view of a priori assumptions, differences in the equation's relation to a_1. The incident $a_1(f_S)$ is linear and the incident $a_1(f_C)$ is non-linear, however, both variations of equation 9 are linear with respect to a_2. The work in [15] shows, for $hotS_{22}$, that equation 11 is really a basic functional description of a device's nonlinearity. It

details, through the use of “smiley faces”, the impact of hot S-parameters, extended hotS_{22} and quadratic hotS_{22}. The importance of the work concerns the phase relationship between a_1 and a_2 or 'P', as it is termed in [15], because this is the term that provides the necessary deformation to the “smiley face” and results in better agreement between measurements and model.

$$\begin{bmatrix} b_1(f_c) \\ b_2(f_c) \end{bmatrix} = \begin{bmatrix} hotS_{11} & hotS_{12} \\ hotS_{21} & hotS_{22} \end{bmatrix} \begin{bmatrix} a_1(f_c) \\ a_2(f_c) \end{bmatrix} + \begin{bmatrix} T_{12} \\ T_{22} \end{bmatrix} e^{j2\varphi(a_1(f_c))} conj(a_2(f_c)) \quad \text{(II-13)}$$

In equation 13 the a_h and b_h matrices are functions of harmonic frequency f_C and the hot S-parameters are the same as before. The 'T' matrix consists of model coefficients that relate to the conjugate of the output perturbation $a_2(f_C)$, hence why they are output only 'T' terms. As such, equation 13 is the extended hot S-parameter equation from [13], where the exponential part equates to the constant 'P' in [15], the phase difference between a_1 and a_2. The addition of the 'T' terms and their association with a_2 is because at higher degrees of nonlinearity the phase difference between a_{11} and a_2 becomes important to the accuracy of the model. The interpretation of the 'T' terms, suggested in [13], is usually problematic but can be looked at in terms of stability hot S-parameters. If equation 11 is considered and the probing measurement frequency f_S is allowed to

approach the fundamental frequency f_C the responses to the a_1 and a_2 inputs would have two terms near the fundamental tone responses f_C: a direct mapping of frequency f_S and a mixing product at a frequency $(2f_C-f_S)$, see figure 5.

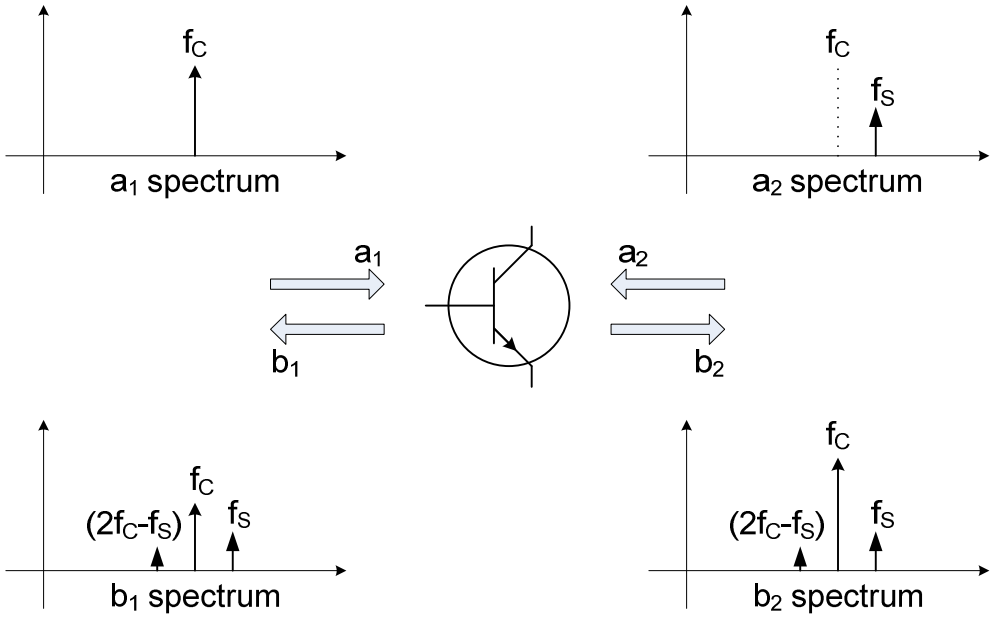

Figure II-5: Spectra of the scattering waves for the frequencies f_C and f_S, where f_S is approaching f_C [13].

If f_S approaches f_C then the mixing product $(2f_C-f_S)$ will get close to f_C and cannot be neglected. In [13] the conjugate operator is associated with the mixing formulations $(2f_C-f_S)$, as it is an image mixing product.

2.3.2 Measurement of Hot S-Parameters

The measurement of these parameters depends on the application. If the hot S-parameters are being used for stability measurements there is one scenario and if they are being used for non-linear characterisation there is another scenario. The difference mainly relies on the necessary assumptions. For stability measurements the probe frequency 'f' can be swept as shown in [14] and is usually much lower than the drive frequency F_0 and since stability is being investigated at the lower frequency the mixing products ($KF_0 \pm f$) are not considered. For predicting a device's distortion characteristics, the assumptions allow for the probe frequency to be at the fundamental or a harmonic frequency (F_0 or $k.F_0$).

Figure 6 shows a block diagram of a measurement system setup that would be required to extract hot S-parameters. It shows that, for a correctly biased device, an input drive is applied to the DUT at a frequency F_0 the output tuner would then converge on a suitable load (e.g. near the device's optimum power point) before the second source, at a lower frequency 'f', switches between sending its probing S-parameter measurement tones in the forward and reverse directions. The forward measurement obtains hotS_{11} and hotS_{21} and the reverse measurement obtains hotS_{12} and hotS_{22}. The extraction of the stability hot S-parameters is the same as the one necessary for

S-parameters, hence the appropriate travelling wave quotients are used.

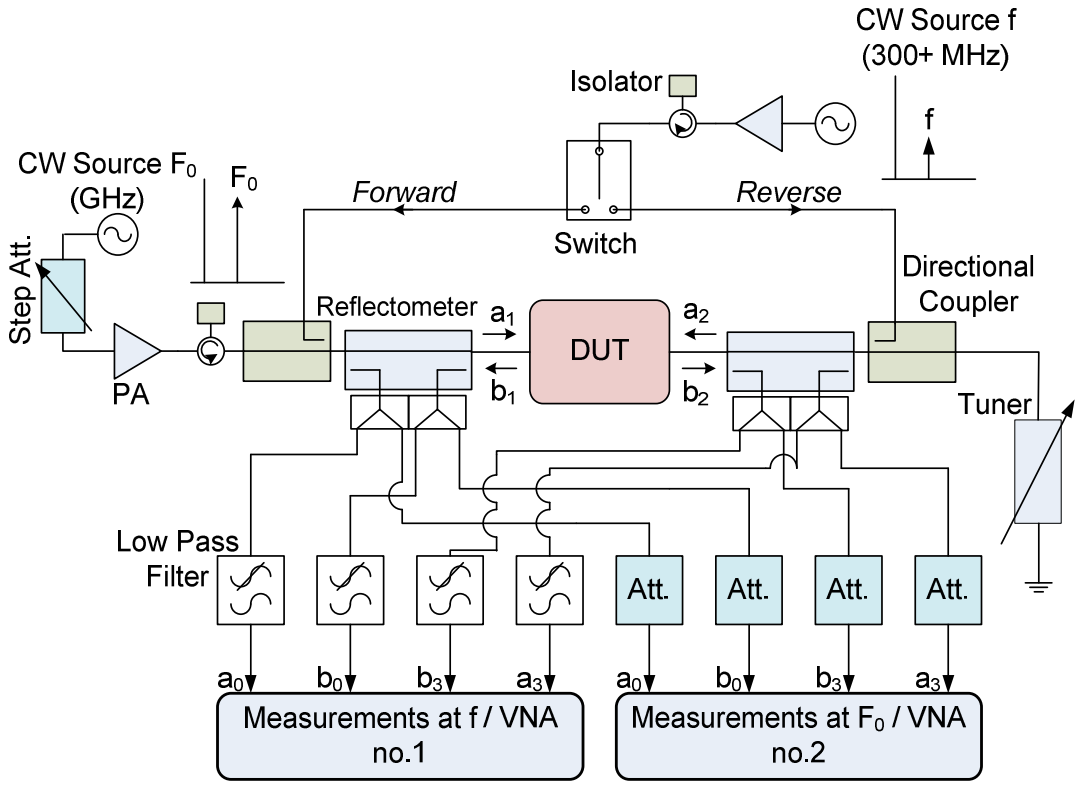

Figure II-6: Measurement system block diagram [14].

2.3.3 Hot S-Parameter Discussion

There are various types of hot S-parameter and the application is the main driver behind what type is used. The measurement procedure is, understandably, different in comparison to the standard S-parameter or the VIOMAP approaches. With regards to measurements, the user must be aware of the necessary assumptions that accompany the type of hot S-parameter before deciding upon the setup. In general, the measurement setups are more complicated

than the other modelling approaches; hence, they require more equipment and can cost more. The formulaic structure and augmentations to it can be seen in the X-parameter and Cardiff model solutions that follow, so it was definitely a step in the right direction. It was the growth in popularity of X-parameters that probably saw diminishing usage of hot S-parameters, as the measurement setup was easier (with Agilent's PNA-X) and the model structure was rigid, as there were three terms that needed to be extracted for the model.

2.4 X-PARAMETER MODELLING

This school of thought will be treated alone, rather than with the S-function paradigm, as there are great similarities between the two in the model measurement, extraction, and only small differences in model formulation. In practice though, X-parameters, having been backed by Agilent Technologies, are more widespread and used more often in the RF and Microwave industry. It is by virtue of this that X-parameters will be the paradigm analysed and discussed in this section.

2.4.1 X-Parameter Theory

X-parameters are a superset of S-parameters and the modelling process, like the hot S-parameter approach, is a frequency domain black-box behavioural modelling concept. X-parameters are based on the Poly-Harmonic Distortion work in [16-17], where, for the case where a system is stimulated by an $A_{1,1}$ and all the generated harmonics are small in comparison to that $A_{1,1}$, the harmonic superposition principle is used. Figure 7 shows how distortion enters the output spectrum when applying the harmonic superposition principle to the input spectrum.

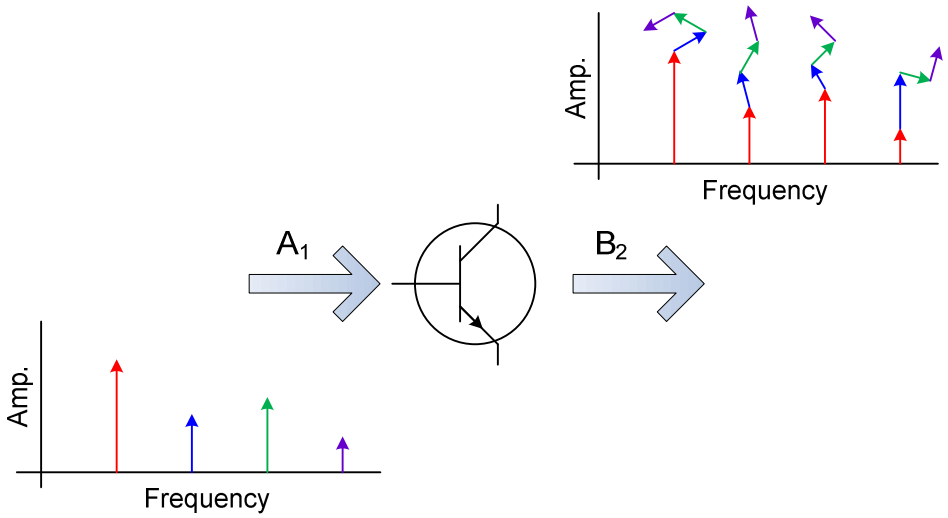

Figure II-7: A visual representation of the harmonic superposition principle [18].

The case in figure 7 is a simplified one only concerning the input $A_{1,h}$ and output $B_{2,h}$ signals and neglecting the $A_{2,h}$ and $B_{1,h}$ signals. If at first the $A_{1,1}$ component is considered alone, as an input to the system, then that would result in the first four frequency components

of $B_{2,h}$. Then the second $A_{1,h}$ component can be considered and this would result in the first summation/deviation to the output $B_{2,h}$ spectrum. It follows then that the third and fourth $A_{1,h}$ components ($A_{1,3}$ and $A_{1,4}$ respectively) result in the third and fourth summations/deviations to the output $B_{2,h}$ spectrum. As stated in [17] "the harmonic superposition principle holds when the overall deviation of the output spectrum B_2 is the superposition of all individual deviations." It should be noted that the experimental verification of the principle in [19] holds true for the practical amplifier modes. The harmonic superposition principle utilised in the X-parameter format gives the following equation:

$$B_{mk}^{N} = \sum_{nh} X_{S\,mknh}(A_{11}^{N})A_{nh}^{N} + \sum_{nh} X_{T\,mknh}(A_{11}^{N})A_{nh}^{N^*} \tag{II-14}$$

Equation 14 [20] is a generalised equation that shows the phase-normalized output B^N waves as being the linear summation of the input A^N waves and their conjugates (represented by the asterisk (*)). Equation 14 is linear in all but one component namely A_{11} which is assumed to be the only large signal frequency component. As such the superposition principle cannot apply. The functions X_S and X_T, which have magnitude and phase, are scattering functions as opposed to scattering parameters. Note that the two have the subscripts 'mknh': 'm' and 'k' correspond to the respective port and harmonic index of the output 'B' wave being considered; 'n' and 'h'

correspond to the respective port and harmonic index of the input 'A' wave being considered. By virtue of this notation, the scattering functions allow for multi-harmonic interactions to be characterised. For example the effects of the input second harmonic A_{12} on the output B_{21} component can be characterised as well as any manor of relevant combinations, as long as the system is stimulated with the correct A_{ph} signals. A more practical case, concerning more familiar scattering quantities, would be to observe the changes in B_{21} (output fundamental component) as a function of A_{11} (input fundamental drive) and A_{21} (output reflected fundamental). In this case the general equation 14 becomes more specific:

$$B_{21} = X_{S_{2111}}(|A_{11}|) + X_{S_{2121}}(|A_{11}|)A_{21} + X_{T_{2121}}(|A_{11}|)P^2 conj(A_{21}) \quad \text{(II-15)}$$

Equation 15 provides a case that would be needed by most amplifier designers, because it concerns the output of a system, B_{21}, in response to an input A_{11} and A_{21} (i.e. fundamental load-pull). Note that the product $X_{S2111}A_{11}$ is often termed X_{F21}. It is a distinct element because it is the term that deals with the large-signal A_{11} that is outside the harmonic superposition principle. It should be clear that to be able to do any analysis on B_{21} at least three quantities must be known:

1. $X_{S_{2111}}(|A_{11}|)A_{11}$ // $X_{F_{21}}(|A_{11}|)A_{11}$

2. $X_{S_{2121}}(|A_{11}|)A_{21}$

3. $X_{T_{2121}}(|A_{11}|)P^2 conj(A_{21})$

This requires that at least three measurements be made so as to have sufficient data to extract the three quantities.

2.4.2 Measurement of X-Parameters

There are two ways of obtaining X-parameter models. The first, that will be discussed, is the 'on-frequency' method. The second is the 'off-frequency' method. The principles in both techniques are the same.

The 'On-Frequency' Method:

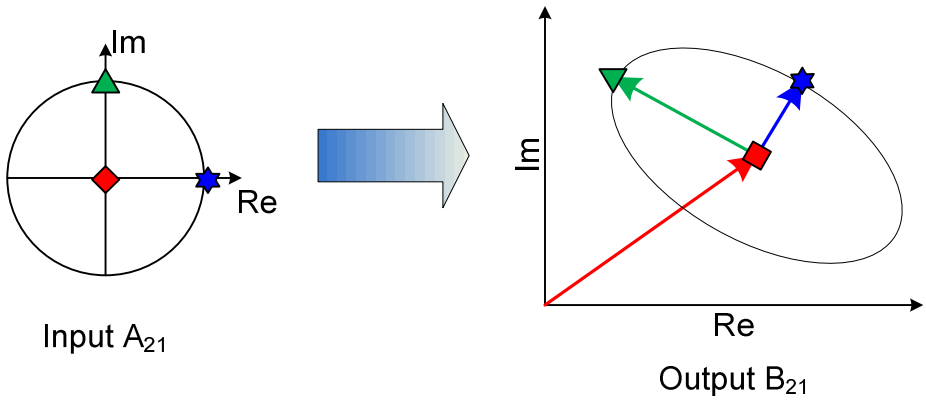

Figure II-8: Simple diagram of the parameter extraction procedure [17].

To extract the necessary parameters in equation 14 the basic set of three measurements that need to be performed are shown in figure 8. Firstly, an A_{11} signal is applied and kept constant for the rest of the measurement (shown as the square in figure 8). This initial condition allows for the extraction of the $X_{S2111}(|A_{11}|)A_{11}$ term. The next step is to perform two independent orthogonal perturbations of the term A_{21}. This is done by applying an A_{21} signal with θ° phase then applying an A_{21} with a (θ±90)° phase (represented by the star and triangle respectively in figure 8). These last two measurements allow for the extraction of the $X_{S2121}(|A_{11}|)$ and $X_{T2121}(|A_{11}|)P^2$ terms. A typical measurement system configuration that would allow for the aforementioned measurements is shown in figure 9.

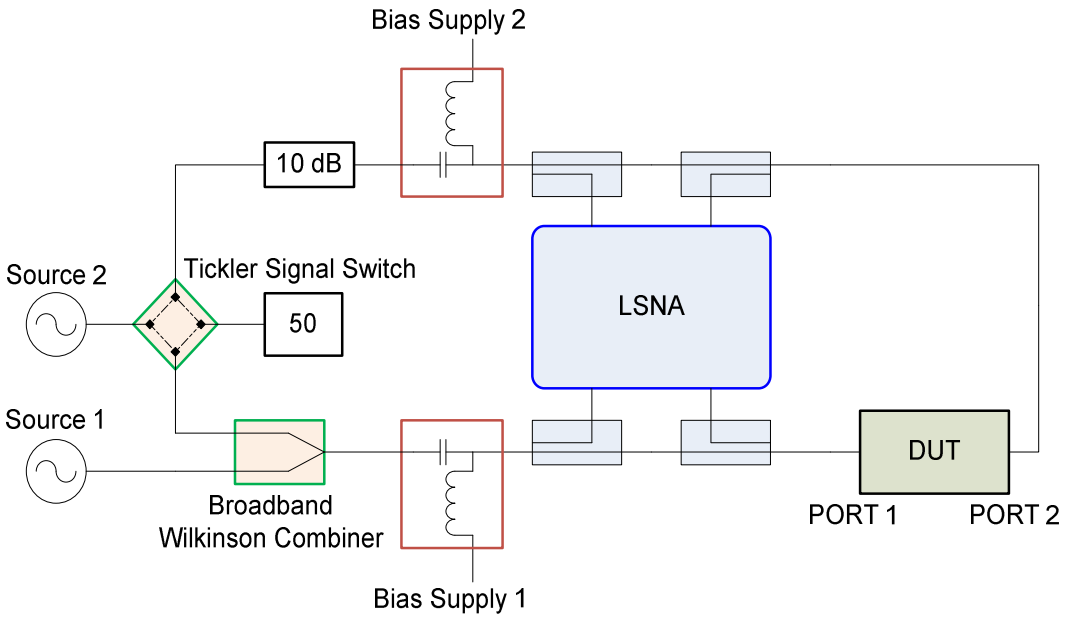

Figure II-9: Block diagram of a typical measurement setup [17].

In figure 9, source 1 is used for the generation of the large-signal A_{11} and source 2, combined with a switch, is used for the generation of the small-signal A_{ph} orthogonal tones, termed 'tickler signals' in [17]. An interesting point with the set of measurements is that, although the minimum number of measurements is three, if a multitude of measurements are performed the redundancy gained presents opportunities in terms of system characterisation and, from this redundancy, data can be collected on noise and model errors [17].

The drawback of the above scenario is that the measurements are based around matched impedances. Therefore, the ability to characterize the whole Smith Chart is entirely reliant on the extrapolation capabilities of the localized model measured in a 50Ohm environment. This would put unnecessary strain on the extrapolation capabilities of a model that is best used for interpolation. Moreover, because deviating from a match can cause large variations in a_{21}, it would not be small when compared to a_{11}; hence, the harmonic superposition principle would not hold. This violation of the harmonic superposition principle should provide erroneous responses. The work in [19] recognises that most high power devices have optimal performances far from 50Ohm. Furthermore, it is asserted that the acquisition of X-parameters over a large area of the Smith Chart is a necessity for the model to remain

valid over the range of impedances it would meet in design applications.

Figure 10 shows that the measurement system used in [19] is based around Agilent's PNA-X [21], which has the NVNA and X-parameter options. With this system, X-parameters can be measured at each impedance point on a load-pull grid. These localised, impedance dependant, X-parameters, provide separate models around each impedance point. Collectively, all the gathered models would provide enough information over the load-pull area for an accurate model to be extracted.

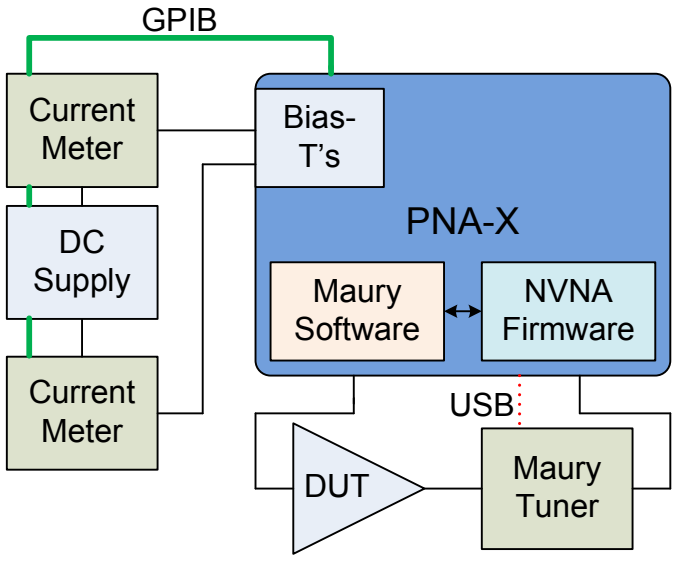

Figure II-10: Block diagram of the load dependent X-parameter measurement setup [19].

The 'Off-Frequency' Method:

This method is in principle the same as the 'on frequency' method. However, the generation of the orthogonal 'tickler signals' is achieved differently. They are generated by injecting a perturbation at a frequency offset to the fundamental A_{11} drive frequency. This can be compared to the measurements performed to obtain hot S-parameters. There is an issue of increased hardware and complication of measurement approach needed to perform the off-frequency measurement, which is why some might prefer the on-frequency method.

2.4.3 X-Parameters Discussion

X-parameters are currently the most prolific behavioural modelling parameters being used. By virtue of their development being 'in-house' at Agilent, their operation and form are composed with ADS's Harmonic Balance (HB) simulator in mind. When this is coupled with Agilent's hardware, PNA-X, the user has a complete measurement to simulation-design path. Perhaps at first this is attractive for industry. However, there will always be pitfalls when you try and make a whole industry buy your measurement solution if they want to measure X-parameters.

The model itself has been shown to characterize load-pull data [19], incorporate long-term memory effects [22], and be used predict broad-band responses [23]. In terms of equation complexity, however, it is limited to three parameters X_F, X_S, and X_T; solutions to which are converged upon with linear regression techniques. These equate to the S_{ph} and T_{ph} terms in equation 13 in section 2.3.1 about hot S-parameters. The issue with having a rigid formulaic structure is that it is inflexible when presented with increasing degrees of nonlinearity. The observed gains in model accuracy with the hot S-parameter approach when quadratic terms were added are not available to the rigid X-parameter structure. It is supposed that this can be solved by increasing the density of measurement points, to take the strain off the X-parameter formulation by having load points situated inside the interpolation region of a local X-parameter model. Although, this solution is flawed, due to the fact that more measured impedance points means more impedance-dependent X-parameters yielding a larger X-parameter data file. Admittedly, ADS handles large X-parameter data files well. However, current trends in measurement and design have been focusing on output fundamental and second harmonic load terminations. When the measurement and design community want models over more power, bias, and frequency levels accompanied with more harmonic data, the file sizes would become too great for most desk-top PC's to cope with any type of simulation. This file size problem is inherent for all potential modelling solutions. However, behavioural model formulations allow

for efficient measurement data compression and X-parameters only go part of the way.

2.5 THE CARDIFF MODEL

Over the past several years, the Cardiff Model has undergone a metamorphosis. It began as a Direct Wave Look-Up Table (DWLUT) approach ("truth look-up model" [24]) and changed to a polynomial based behavioural model. The DWLUT was created to allow for quick access to measurement data in CAD. However, the accepted pitfalls of the DWLUT approach were overcome with an equation based descriptive behavioural model approach. Both approaches are detailed by Qi in [24]. This section will look at the two approaches separately, beginning with the DWLUT approach.

2.5.1 The Cardiff DWLUT Model Theory

The Cardiff DWLT model is table based and utilises admittance, as a function of the operating conditions, to relate a device's extrinsic measured port currents and voltages. Below is a simplistic block diagram from the systems perspective.

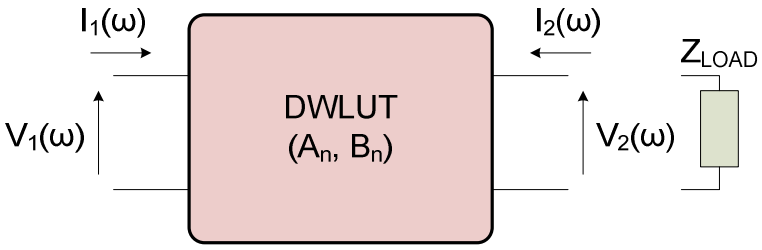

Figure II-10: DWLUT system.

In figure 10 the port currents $I_1(\omega)$ and $I_2(\omega)$ are treated as the responses of the system caused by the application of the voltages $V_1(\omega)$ and $V_2(\omega)$. A_n and B_n are the systems port 1 and port 2 transfer functions, respectively. The different port currents and voltages at specific load impedances Z_{LOAD} are related by equations containing A_n and B_n [25]:

$$I_1(\omega) = A_0 \cdot \delta(\omega) + \sum_{n=1}^{m} A_n \cdot V_{IN}^n \cdot \delta(\omega - 2\pi \cdot n \cdot f_0) \quad \text{(II-16)}$$

$$I_2(\omega) = B_0 \cdot \delta(\omega) + \sum_{n=1}^{m} B_n \cdot V_{IN}^n \cdot \delta(\omega - 2\pi \cdot n \cdot f_0) \quad \text{(II-17)}$$

Where V_{IN} is the input voltage signal, 'n' is the harmonic number, f_0 is the fundamental frequency, and A_0 and B_0 are the DC components. The current and voltage spectra are functions of the many operating

conditions, hence so too are A_n and B_n. With the former being considered the following are obtained:

$$A_n = \frac{I_1(nf_0)}{V_{IN}^n(nf_0)} = F_1(|V_{IN}|, \Gamma_{LOAD}, V_{DC\ IN}, V_{DC\ OUT}) \quad \text{(II-18)}$$

$$B_n = \frac{I_2(nf_0)}{V_{IN}^n(nf_0)} = F_2(|V_{IN}|, \Gamma_{LOAD}, V_{DC\ IN}, V_{DC\ OUT}) \quad \text{(II-19)}$$

Equations 18 and 19 [25] are thus using the input and output port admittances to relate the currents and voltages at those ports. The above equations equate A_n and B_n to functions with the arguments of input drive voltage, load reflection coefficient, and the input and output bias conditions. This modelling process makes use of the port current and voltages because the resulting A_n and B_n models fit the measurement data irrespective of whether the scattering a-b waves or the currents and voltages are used. The advantage to using the I-V waves becomes apparent when the model data is transported to CAD, namely Agilent's ADS [26]. Here the implementation uses a Frequency Defined Device (FDD) as the 'go-between' for the DWLUT and the simulation circuit. Since this component directly computes with current and voltage, the initial decision to work with them makes the CAD implementation easier.

2.5.2 Measurement of the DWLUTs

Reference [24] concentrates on fundamental load-pull measurements over a range of swept power levels. Figure 11 shows the measurement system, developed by Benedikt et al [27] at Cardiff University, which was used to perform the measurements.

In figure 11, the use of switches 'A' and 'B' are to overcome the problem of a two channel Microwave Transition Analyser (MTA) [28] needing to behave like a four channel instrument in order to perform the measurements. In this configuration, channel 1 would measure the incident travelling waves, a_1 and a_2, and channel two would measure the reflected travelling waves, b_1 and b_2. In relation to the figure: switch 'A' handles a_1 and a_2 and switch 'B' handles b_1 and b_2. The problem with this is that there can be a loss of synchronisation between the travelling waves. A systematic switching strategy and a phase handover measurement solves the synchronisation problem and allows for the travelling waves to be correctly measured.

Figure 11 shows that active load-pull is used to present the desired impedance environment to the DUT. Unlike passive load-pull, active load-pull utilises convergence algorithms to iteratively converge upon the desired reflection coefficient. Once the error tolerance between desired load and actual load is small enough the system will measure

and store the travelling waves. Providing that the load-pull grid is sufficiently dense, travelling waves for each load-pull point on the grid can be collected, without raising concerns of poor interpolation within the CAD environment. The data table can be expanded when uniform load-pull measurements are done at varying power levels.

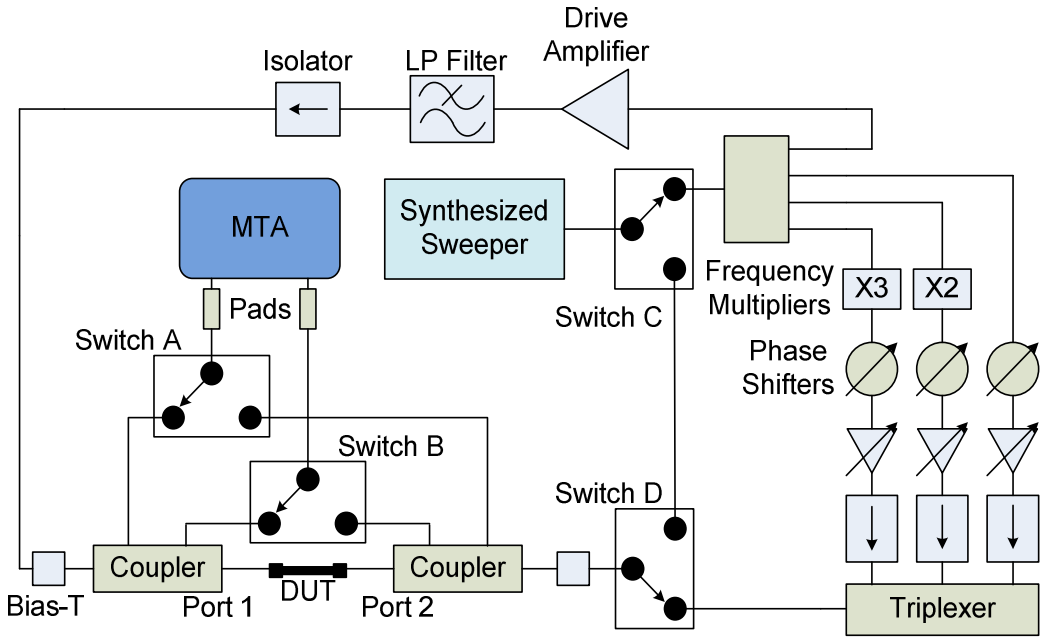

Figure II-11: Block diagram of the Cardiff waveform measurement system [27].

The extraction of the parameters is virtually nonexistent, since the travelling waves are used to compute the currents and voltages which are then substituted in the ratios of equations 15 and 16 to obtain the relative A_n and B_n admittance quantities. This process halves the amount of data contained when compared with the measurement file, as one value of admittance is stored to represent an I-V pairing.

2.5.3 DWLUT Discussion

The main aim of the DWLT approach was to enable the import of load-pull measurement data into the CAD environment for simulation. From this perspective it was very successful. It fails as an overall modelling solution because it does not generate a relationship between a device's inputs and outputs. The approach handles one measurement at a time as a look-up parameter, therefore does not compress the measurement data much, and does not aim to describe the system response as a whole. It also does not have any native interpolation or extrapolation capabilities and for this it relies on CAD and its mathematical ability to compute unknown quantities within-grid data points (interpolation) and beyond-grid data points (extrapolation). It is shown in [25] that CAD has the ability to accurately interpolate between measurement points, providing that the data points are not too sparsely situated. Extrapolation is not as good. The fundamental extrapolation holds under a 1% error when a data point is chosen just outside the measurement grid. However, when the load is pushed further away from the measurement grid larger discrepancies in the DC components are generally observed and harmonic errors quickly exceed 10% [25].

2.5.4 The Cardiff Behavioural Model Theory

The earliest work in this area was performed by Qi [24]. The DWLUT model had proved useful as a tool for observing load-pull data in the CAD environment, however, the DWLUT approach does not yield a relationship between the input and output characteristics.

In [24] there is analysis of the PHD model [16-17], mentioned earlier. As a model formulation the PHD model is good, but it relies on the harmonic superposition principle. In examples where a device is terminated with a 50Ohm impedance, the harmonic superposition principle holds. However, in [25] the models are necessary for characterizing load-pull data from high power devices. Since optimum power, gain, and efficiency impedance points are usually located far from 50Ohm and involve large variation in a_2 the harmonic superposition principle does not hold.

The work in [24] links the DWLUT work with its provision of the necessary extension to the poly-harmonic distortion work, in [16], no longer limited by the superposition principle to allow for large variations in a_2. The polynomial formulation deals with the travelling waves as opposed to the port currents and voltages considered in the DWLT approach. It treats the responses, b waves, as functions of a_1 and a_2:

$$b_1 = f(a_1, a_2) \quad b_2 = g(a_1, a_2) \qquad \text{(II-20 \& 21)}$$

The functions, f( ) and g( ), are then distributed between their arguments to present the assumption that if b_p is a function of both a_1 and a_2, then b_p is also a function of a_1 multiplied by a function of a_2:

$$b_1 = f_1(a_1)f_2(a_2) \quad b_2 = g_1(a_1)g_2(a_2) \qquad \text{(II-22 \& 23)}$$

The paper then approximates the functions to 3rd order polynomials and reformulates them so that they resemble the PHD formulations in [16]. The difference between the equations in [24] and the PHD equations is that they are a function of both a_1 and a_2.

$$b_1 = S_{11}a_1 + T_{11}a_1^*Q^2 + S_{12}a_2 + T_{12}a_2^*P^2 \qquad \text{(II-24)}$$

$$b_2 = S_{21}a_1 + T_{21}a_1^*Q^2 + S_{22}a_2 + T_{22}a_2^*P^2 \qquad \text{(II-25)}$$

The components P and Q in the above equations represent the phase vectors $e^{-j\omega(a1)}$ and $e^{-j\omega(a2)}$ respectively. This approach only concerns the fundamental output impedance behaviour and was the first step in the Cardiff behavioural modelling formulation.

A noted point for extraction in [24] was that high-power PAs normally have low values for their maximum power impedance points. This

finding results in large values of a_2, which would normally require a high order polynomial for the purpose of a_2 modelling. To be able to reduce observed strong nonlinearities, impedance renormalization was used on the I-V data in its conversion to a-b-data:

$$a_{Renorm} = \frac{V + Z_{opt} I}{2} . \frac{\sqrt{Re(Z_{opt})}}{|Z_{opt}|} \qquad \text{(II-26)}$$

$$b_{Renorm} = \frac{V - Z_{opt} I}{2} . \frac{\sqrt{Re(Z_{opt})}}{|Z_{opt}|} \qquad \text{(II-27)}$$

Equations 26 and 27 demonstrate a pseudo-wave based renormalization and the resulting renormalized impedance will be complex.

The work by Qi was extended by Woodington in his doctoral thesis and papers [30-32] and Cardiff's measurement and modelling efforts were summarized by Tasker in [33]. The predominant goals of the works [30-32] were to extend the harmonic complexity of Qi's behavioural model platform and define the coefficient structure that output harmonic models frequently exhibited. There was slight modification, in [31], of equations 24 and 25:

$$b_1 = S_{11}|a_1|P + T_{11}|a_1|Q.\frac{Q}{P} + S_{12}|a_2|Q + T_{12}|a_2|P.\frac{P}{Q} \quad \text{(II-28)}$$

$$b_2 = S_{21}|a_1|P + T_{21}|a_1|Q.\frac{Q}{P} + S_{22}|a_2|Q + T_{22}|a_2|P.\frac{P}{Q} \quad \text{(II-29)}$$

These equations introduce the relative phase vectors P/Q and Q/P, or displayed in exponential form: $P/Q = e^{-j\omega(a1-a2)}$ and $Q/P = e^{-j\omega(a2-a1)}$. The work highlighted that each 'S' and 'T' coefficient now had a unique phase vector and if load-pull measurements were performed on loci of constant $|a_1|$ and $|a_2|$ with swept relative phase then the extraction of the 'S' and 'T' coefficients could be extracted independently by integrating the respective measured b-waves after multiplying them by the correlated phase operators. For example:

$$S_{11}|a_1| = \frac{1}{n}\sum b_1.{}^{1}/_{P}\ , \quad T_{11}|a_1| = \frac{1}{n}\sum b_1.{}^{P}/_{Q^2} \quad \text{(II-30 \& 31)}$$

This work also uses impedance normalization, like [24], to improve model accuracy. However, it should be noted that the renormalization in [24] was for a high-power device, whereas in [31]

the device is rated a 0.5W. This means that any increase in model accuracy would be slight, as low power devices output power optimums are usually near 50Ohms.

The results found that modelling with the polynomials in equations 24 and 25 was insufficient and that there were observable differences between modelled and measured b_2 responses. The reason was because of the polynomials only accounting for nonlinear behaviour up to 3rd order mixing between a_1 and a_2. However, considering the $(P/Q)^n.P$ and $(Q/P)^n.Q$ phase vectors it was seen that when n=3 the phase complexity accounted for 7th order mixing and was enough to accurately predict the response of the load-pull contours.

The work in [32] extended the harmonic complexity of the Cardiff Model, to account for fundamental and second harmonic load-pull measurements, and provided a more generalized formulaic expression:

$$b_{p,h} = P_1^h \sum_n \sum_r \left\{ G_{p,h,n,r}\left(|a_{1,1}|, |a_{2,1}|, |a_{2,2}|\right) \left(\frac{Q_1}{P_1}\right)^n \left(\frac{Q_2}{P_1^2}\right)^r \right\} \quad \text{(II-32)}$$

In equation 32, subscripts 'p' and 'h' are the familiar port and harmonic indices. The 'n' and 'r' scripts denote the model order or complexity. The 'G' term denotes the extractable coefficient. It is shown to be a function of the magnitudes of the driving signals for the system; however, it is also a function of other fundamental operation parameters, namely bias and frequency.

Tasker better defines the model mixing order in [33], where a generalised model equation is formulated to encompass any number of harmonics in the load-pull measurements:

$$b_{n,h} = P_1^h . \sum_{m_r=-(w_r+1)/2}^{m_r=+(w_r+1)/2} \cdots \cdots \sum_{m_1=-(w_1+1)/2}^{m_1=+(w_1+1)/2} K_{n,h,m_1,\ldots,m_r} \cdot \left(\frac{Q_1}{P_1}\right)^{m_1} \cdots \cdots \left(\frac{Q_r}{P_1^r}\right)^{m_r} \quad \text{(II-33)}$$

This equation represents the functional expression of 'G' in equation 32 as the parameter 'K'; the meaning is the same however.

2.5.5 Measurement of the Cardiff Behavioural Model

The work by Woodington et al [31] and [32] draws reference to the measurement system developed by Tasker [34]. This system was expanded in order to perform two harmonic load-pull CW

measurements. A generic multi-harmonic load-pull measurement system, based around a four channel receiver, is shown in figure 12. The receiver's channels are attenuated for protection; often the input attenuation is lower than the output attenuation, due to the power necessary at each side of a device. The receiver and ESG signal generators are connected, in daisy-chain arrangement, with a 10MHz reference signal. This provides a coherent trigger for measurement, thus allows for phase coherent measurements. In the path of the signal sources there needs to be sufficient amplification and phase rotation for reflection coefficients to be generated covering the whole Smith Chart. A load-tuner and PA combination can be used, with the same effect; however, this approach should really be used on high power devices where load-pull amplifier power is lacking.

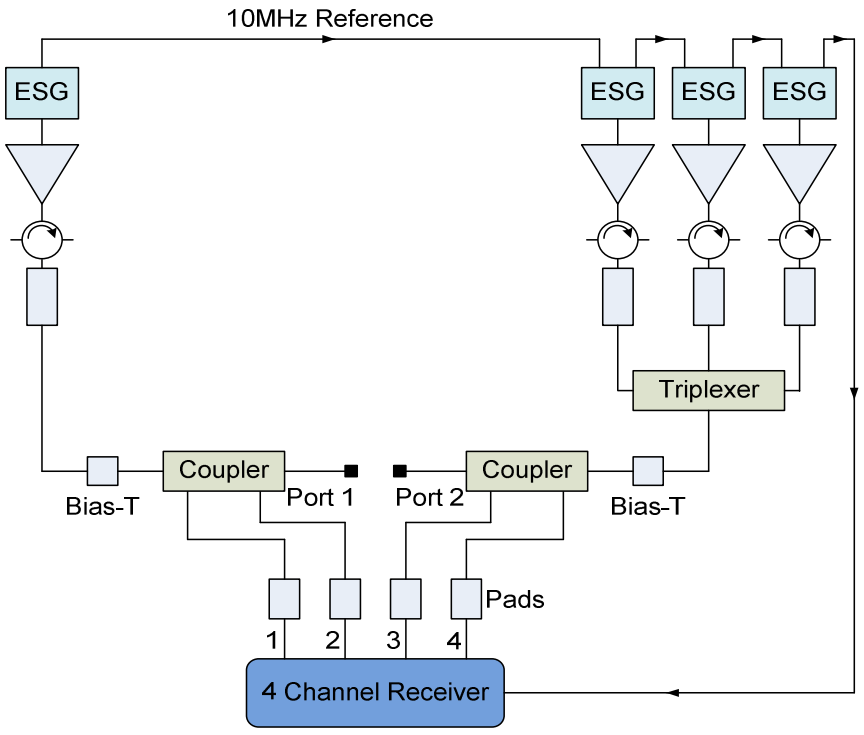

Figure II-12: Nonlinear network analyser "waveform" measurement system [30].

The measurements required for model extraction are, simply, load-pull measurements. The works [30-32] utilise impedance points located on concentric circles, as they provide a clear base for observational analysis of distortion on the load-pull grid. In [30] and [32] the analysis of fundamental models and second harmonic mixing models requires two harmonic load-pull to be performed. Taking [32] as the example, a circle of fundamental impedance points, and another circle of second harmonic impedance points were imported into load-pull software, developed by Saini [35]. The software took all the points and iterated round the circles, measuring once per iteration, to produce a fundamental impedance circle of second harmonic impedance circles. The normalized travelling-wave measurement data for the aforementioned nested load-pull measurement scenario are shown in figure 13. Figure 13 shows how the $b_{2,h}$ waves respond to the nested injections of $a_{2,h}$. The $a_{2,1}$ and $a_{2,2}$ traces show fuzzy dots, this is a result of performing nested load-pull because when $a_{2,2}$ is varied for a specific $a_{2,1}$ that $a_{2,1}$ point is affected slightly when iterating through points of $a_{2,2}$ and vice-versa.

Measurements do not simply provide the operator with a model. An extraction procedure is necessary to converge on a best fit model and so the collected data can be used inside CAD via a representative polynomial.

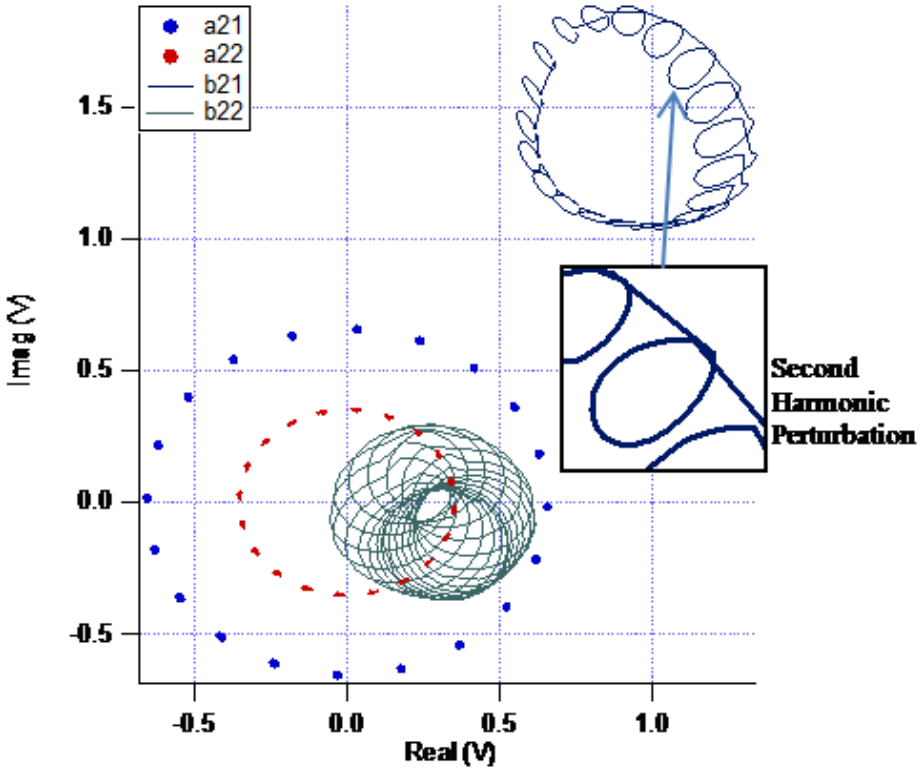

Figure II-13: A sample of the recorded travelling-waves from the nested load-pull measurement sequence [30].

2.5.6 Extraction of the Cardiff Model

It would be natural to think that after the measurement of a model the extraction of the parameters is self evident; this thought aligns itself with the DWLUT approach. However, to converge on a polynomial capable of a global fit of the data some computation is necessary. Previously it has been seen that enough data is collected with load-pull to extract 3rd order phase models. In fact it is usual to perform load-pull over vast impedance grids so there is potential for extracting higher order models. In all cases a mathematical algorithm is utilised, in order to reduce the error in the model to a minimum.

$$[B] = [A].[R]$$

$$[A]^H.[B] = [A]^H[A].[R] \quad \text{(II-34, 35 \& 36)}$$

$$[R] = ([A]^H[A])^{-1}.[A]^H.[B]$$

Equations 34 to 36 show the derivation of the Least Mean Squares (LMS) algorithm that is tailored to suit this type of modelling. It is a type of adaptive equation used to change the coefficient weighting, in this case R, of an equation to produce the least mean squares of an error. By using this algorithm a model of best fit can be converged upon giving the best global accuracy for the provided data.

Once the coefficients are computed the [B] matrix can be calculated from the [A] and [R] matrices and it can be compared to the measured [B] to give a model error of B. The factors that drive this error are model complexity and measurement quantity. These two are not mutually exclusive, in that the measurement quantity directly affects the maximum complexity. If there are more coefficients than measurement data points the LMS algorithm will not converge due to their being more unknown quantities than known quantities.

2.5.7 The Cardiff Model Discussion

Although the Cardiff model initially began as a way to quickly transport measurement data into CAD for observation it grew into a usable behavioural modelling solution that efficiently compressed measurement data. The work in [24] shows a specific case of the model being applied to a high power device and raises the importance of impedance renormalization. Woodington extended the scope of the model and introduced more generalized model formulations in [30-32]. The investigations into output fundamental and second harmonic models showed that mixing of the harmonic model coefficients was needed to describe the device's harmonic interactions. The change in application and device process saw that the fundamental coefficient space needed to be increased to account for 7^{th} order mixing. The necessity and effectiveness of the renormalization can be questioned, as the works by Woodington et al are based on relatively low power devices when compared to the devices Qi et al were using.

Unlike X-parameters, the Cardiff model approach does not need to perform specific X-parameter-type measurements and simple load-pull is sufficient. The model formulation is flexible to allow for future changes to normal device processes and device design. This can be seen as similar to that of hot S-parameters, except the measurement procedure is simpler. The flexible formulation essentially means that

X-parameters can be a subset of the Cardiff model coefficients or if there are three model coefficients, the Cardiff model equates to X-parameters. The relative ease of measurement and flexible nature of the model is promising. However, current CAD implementations are not as flexible as the model formulations and would need improving if the Cardiff model could be mentioned alongside X-parameters. Moreover, the harmonic scope of the measurement system does not cater for the control of more than three sources, which limits model analysis of input harmonics, and higher harmonics.

2.6 REFERENCES

[1] E. W. Mathews, "*The Use of Scattering Matrices in Microwave Circuits,*" IRE Transactions – Microwave Theory and Techniques. Pg 21-26, Apr. 1955.

[2] K. Kurokawa, "*Power Waves and the Scattering Matrix,*" IEEE Transactions on Microwave Theory and Techniques. Pg 194-202, Mar. 1965.

[3] "*HEWLETT-PACKARD JOURNAL,*" Technical Information from the Laboritories of the Hewlett-Packard Company, Volume 18, Number 6. Pg 13-24, Feb. 1967.

[4] P. Harrop and T. A. Claasen "*Modelling of an F.E.T Mixer,*" Electronics Letters, Vol. 14, No. 12. Pg 369-370. Jun. 1978.

[5] W. H. Leighton, R. J. Chaffin, J. G. Webb "*RF Amplifier Design with Large-Signal S-Parameters,*" IEEE Transactions on Microwave

Theory and Techniques, Volume 21, No. 12. Pg 809-814. Dec. 1973.

[6] F. Verbeyst and M. V. Bossche, *"VIOMAP, the S-Parameter Equivalent for Weakly Nonlinear RF and Microwave Devices,"* IEEE Transactions on Microwave Theory and Techniques, Volume 42, No. 12. Pg 2531-2535. Dec 1994.

[7] F. Verbeyst and M. V. Bossche, "VIOMAP, 16QAM and Spectral Regrowth: Enhanced Prediction and Predistortion based on Two-Tone Black-Box Model Extraction," 45th ARFTG Conference Digest-Spring, Volume 27. Pg 19-28. May 1995.

[8] F. Verbeyst and M. V. Bossche, *"The Volterra Input-Output Map of a High-Frequency Amplifier as a Practical Alternative to Load-Pull Measurements,"* IEEE Transactions on Instrumentation and Measurement, Volume 44, No. 3. Pg 662-665. Jun 1995.

[9] F. Verbeyst and M. V. Bossche, *"Using Orthogonal Polynomials as Alternative for VIOMAP to Model Hardly Nonlinear Devices,"* 47th ARFTG Conference Digest-Spring, Volume 29. Pg 112-120. Jun 1996.

[10] Hewlett Packard, "*Microwave Network Analyzers, 45 MHz to 100 GHz,*" Downloaded from: www.mrtestequipment.com/getfile.php?s = Agilent...Data...

[11] Hewlett Packard, "*Network Analyzers Test Sets 8510 Series,*" Downloaded from: http://www.equipland.com/objects/catalog/ product/ extras/33812_HP_8516a.pdf.

[12] G. E. Forsythe," Generation and Use of Orthogonal Polynomials for Data-fitting with a Digital Computer," Journal of the Society of Industrial and Applied Mathematics, Volume 5, No. 2. Pg 74-88. June 1957.

[13] J. Verspecht, D. Barataud, J-P. Teyssier and J-M Nébus, "*Hot S-Parameter Techniques: 6 = 4 + 2,*" 66th ARFTG Conference. Dec 2005.

[14] T. Gasseling et al. "Hot Small-Signal S-Parameter Measurements of Power Transistors Operating Under Large-Signal Conditions in a Load-Pull Environment for the Study of Nonlinear Parametric Interactions," IEEE Transactions on Microwave Theory and Techniques. Volume 52, No. 3. Pg 805-812. Mar 2004.

[15] J. Verspecht, "*Everything you've always wanted to know about Hot-S22 (but we're afraid to ask),*" IMS workshop: Introducing New Concepts in the Nonlinear Network Design. 2002.

[16] J. Verspecht, “Black Box Modelling of Power Transistors in the Frequency Domain,” Presented at the 4th workshop on INMMC. 1996.

[17] J. Verspecht and D. E. Root, "*Polyharmonic Distortion Modelling,*" IEEE Microwave Magazine, Volume 7. No. 3. Pg 44-57. Jun 2006.

[18] J. Verspecht, "*Large Signal Network Analysis - 'Going Beyond S-Parameters',*" 62nd ARFTG Conference Short course Notes. Dec 2003.

[19] G. Simpson, J. Horn, D. Gunyan and D. Root, "Load-pull + NVNA = Enhanced X-Parameters for PA Designs with High Mismatch and Technology-Independent Large-Signal Device Models," 72nd ARFTG Microwave Measurement Symposium. Pg 88-91. Dec 2008.

[20] J. Wood, D. E. Root et al. "*Fundamentals of Nonlinear Behavioral Modeling for RF and Microwave Design,*" Chapter 5. Artech House Inc 2005. ISBN: 1-58053-775-8.

[21] Agilent Technologies, "*Agilent 2-Port and 4-Port PNA-X Network Analyzer,*" Downloaded from: http://cp.literature.agilent.com/litweb/pdf/N5242-90007.pdf. Sept 29, 2011.

[22] J. Verspecht et al, "Extension of X-parameters to Include Long-Term Dynamic Memory Effects," IEEE MTT-S International Microwave Symposium Digest. Pg. 741-744. Jun. 2009.

[23] D. E. Root et al, "Broad-Band Poly-Harmonic Distortion (PHD) Behavioral Models from Fast Automated Simulations and Large-Signal Vectorial Network Measurements," IEEE Transactions on Microwave Theory and Techniques, Vol. 53, No. 11. Pg. 3656-3664. Nov. 2005.

[24] H. Qi, "Nonlinear Data Utilization: Direct Data Look-Up to Behavioural Modelling," Doctoral Thesis, Cardiff University. Feb 2008.

[25] H. Qi, J Benedikt and P. J. Tasker, "A Novel Approach for Effective Import of Nonlinear Device Characteristics into CAD for

Large Signal Power Amplifier Design," IEEE MTT-S International Microwave Symposium Digest. Pg 477-480. 2006.

[26] Agilent Technologies, "*Advanced Design System ADS Home page,*" Downloaded from: http://www.home.agilent.com/en/pc1297113/ advanced-design-system-ads?nid=-34346.0&cc=GB&lc=eng.

[27] J. Benedikt, R. Gaddi, P. J. Tasker and M. Goss, "*High-Power Time-Domain Measurement System with Active Harmonic Load-Pull for High-Efficiency Base-Station Amplifier Design,*" IEEE Transactions on Microwave Theory and Techniques. Volume 48, No. 12. Pg 2617-2624. Dec 2000.

[28] Agilent Technologies, "*HP 71500A Microwave Transition Analyzer,*" Downloaded from: http://cp.literature.agilent.com/ litweb/pdf/5091-0791E.pdf

[29] H. Qi, J. Benedikt and P. J. Tasker, "*Novel Nonlinear Model for Rapid Waveform-based Extraction Enabling Accurate High Power PA Design,*" IEEE MTT-S International Microwave Symposium Digest. Pg 2019-2022. 2007.

[30] S. Woodington, "*Behavioural Model Analysis of Active Harmonic Load-Pull Measurements,*" Doctoral thesis submitted to Cardiff University. 2012.

[31] S. Woodington et al, "A Novel Measurement based Method Enabling Rapid Extraction of a RF Waveform Look-Up Table Based Behavioural Model," IEEE MTT-S International. Pg 1453-1456. Jun 2008.

[32] S. Woodington et al, "*Behavioural Model Analysis of Active Harmonic Load-Pull Measurements,*" IEEE MTT-S International. Pg 1688-1691. May 2010.

[33] P. J. Tasker and J. Benedikt, "*Waveform Inspired Models and the Harmonic Balance Emulator,*" IEEE Microwave Magazine. Pg 38-42. Apr 2011.

[34] P. J. Tasker, "*Practical Waveform Engineering,*" IEEE Microwave Magazine. Volume 10, No. 7. Pg 65-67. Dec 2009.

[35] R. S. Saini, "*Intelligence Driven Load-pull Measurement Strategies,*" A Doctoral Thesis submitted to Cardiff University. 2013.

CHAPTER III
MEASUREMENT SYSTEM DEVELOPMENT

The HF measurement systems at Cardiff University have been under constant improvement over the past decade. The challenges of research often call for new improvements of hardware and new procedures or autonomy in software. It was shown in chapter II that the platform for the measurement systems used for modelling was based on the work by Benedikt et al [1]. In order for further model explorations to be conducted, where a device is stimulated by more than the output fundamental and second harmonic signals, the measurement system needs to be updated.

3.1 INTRODUCTION

The measurement system used by Woodington and Saini provided the basis for model investigations concerning the output fundamental and second harmonic frequency dimensions. In order to further analyse harmonic relations in the model formulation, the addition of

one or more signal source was necessary. The previous measurement system did not permit the addition of any more sources because it lacked adequate number of coherent carrier distribution ports. Also the set-up did not permit source locking at all frequencies thus only specific frequencies were previously chosen for operation and it was impossible to perform X-band load-pull measurements.

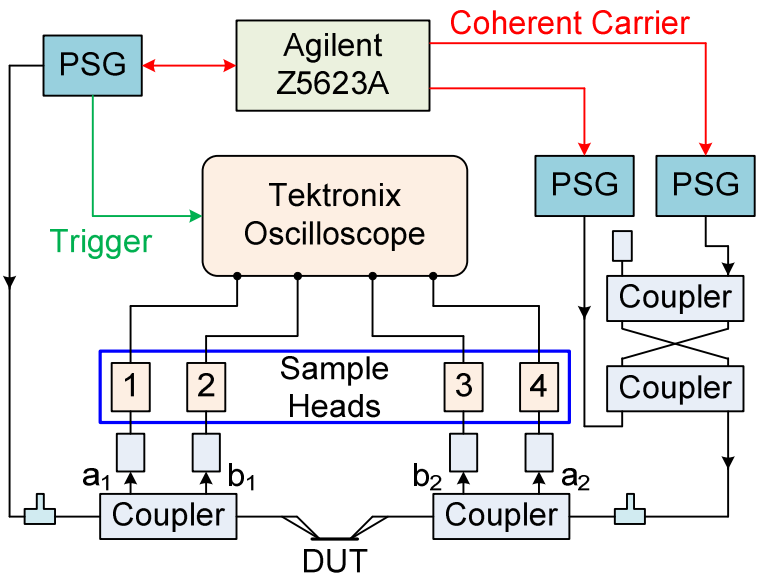

Figure III-1: Two harmonic load-pull measurement system block diagram.

The measurement system in figure 1 is based around the Tektronix DSA8200 sampling oscilloscope [2] for travelling wave measurement and the Agilent Z5623AK07 [3] distribution amplifier, for the distribution of the coherent carrier. The PSGs are from Agilent's E8267D [4] range and have the HCC option, which is important for the coherent carrier set-up as its 3.2-10GHz range allows for a larger

band of stable phase coherence necessary for X-band measurement. The 10MHz references of the PSGs are not suitable for X-band measurements, as at the desired operation frequency of 9GHz the PSGs will drift over time in relation to one another and hence the phases will not be locked.

The importance of having a coherent carrier is that measurements require traceable phase relationships between stimulating signals, if there is no coherent phase relationship the measurement of models becomes impossible. To take the example of the phase vectors Q and P in [5], if there was no common carrier between signal sources then there is no reference for phase and hence the Q/P phase vectors would vary from measurement to measurement for a single load-pull point. Consequently, and importantly, it is crucial for model extraction that there be phase coherence between all sources. Figure 2 shows the master-slave structure of the signal sources and the coherent carrier. This configuration allows all sources the use of the master source's local oscillator; also its coupling with the oscilloscope provides a consistent trigger from signal master to measurement. In this case the attenuated coupled port is connected to the oscilloscope, as it can still be triggered despite 6dB attenuation.

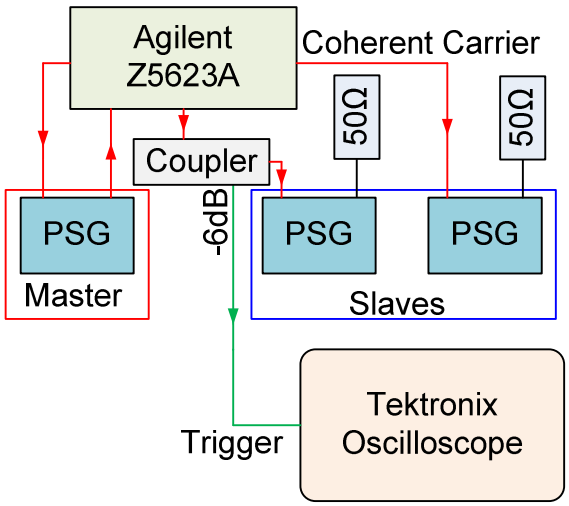

Figure III-2: The Master-slave source configuration.

For the addition of an extra source, to the measurement setup, the Agilent Z5623AK07 needs to be replaced with a carrier distribution system capable of handling more sources.

3.2 Coherent Carrier Distribution Design

The fundamental area of developing the coherent carrier distribution system is ensuring the master source has the same power and fidelity of its phase locked loop (PLL) signal, whilst also delivering the right power to the slave signal generators, as it does when operating alone. The power level of the reference signal to the PLL is important in terms of device safety; as if the signal is too large the PSG can be damaged. The fidelity of the signal is also important as poor signal quality and stability will result in phase jitter that does not allow the

sources to be locked. In principle, the carrier distribution system needs to take the output signal from the master and split it into four signals with the same power as the input, then connect one of the signal ports back to the master, leaving the remaining ports for three additional signal sources. In order to do this the block diagram in figure 3 was used as a design platform.

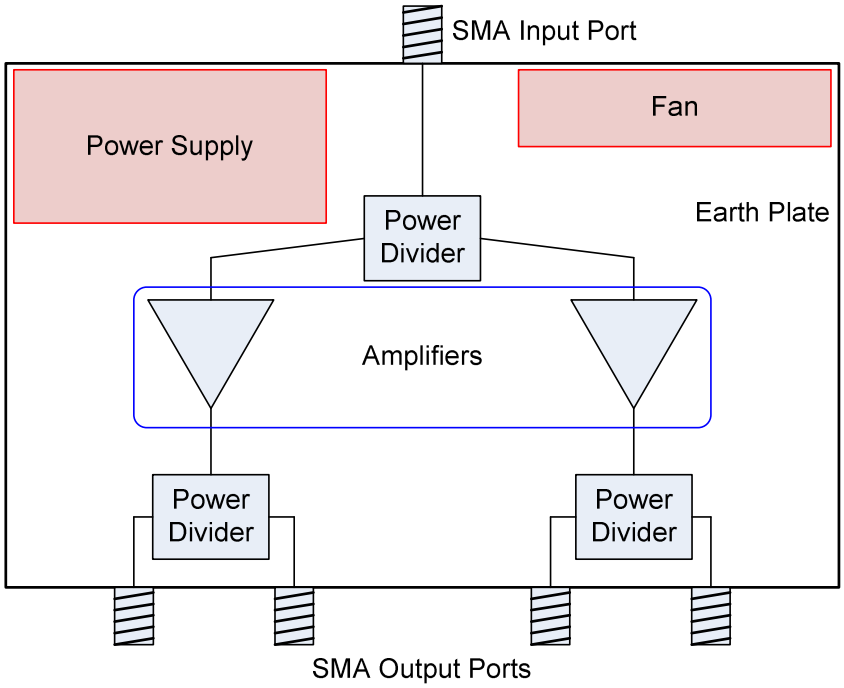

Figure III-3: Block diagram of the coherent carrier distribution system.

Three DC-18GHz ZFRSC-183-S+ power dividers [6], two 700MHz-18GHz ZVA-183-S+ amplifiers [7], and attenuators were procured from Mini-Circuits; there were already multiple fans and power supplies available from old test equipment. The power dividers and amplifiers needed to be procured with the frequency of operation in mind. Due to the HCC PSG option the frequency bandwidth was 3.2-

10GHz, hence the two devices amply cope with the requirement. For the amplifiers, the requirements were an operating supply voltage of 12V and a gain greater than 15dB in linear operation. These allowed for standard 24-12V transformation, which a lot of power supplies do, and the gain would allow for any loss in the final system. The amplifiers should be operated in their linear region and have small stable harmonics so that phase jitter does not occur and ruin the locking of the sources. Some attenuators were procured so that power in the signal paths could be optimised for operation, for this their attenuation values ranged from 1-10dB. All the signal connectors were SMA and made in-house from rigid copper cable with a loss of 1dB at 10GHz.

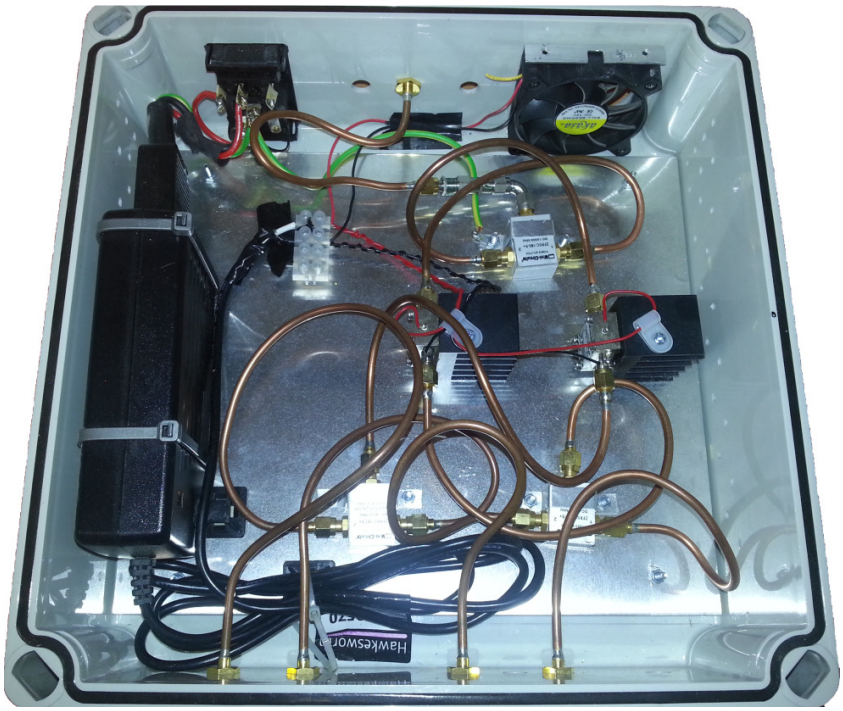

Figure III-4: Block diagram of the coherent carrier distribution system.

Figure 4 shows the completed build of the distribution system. The SMA copper cables had to be bent in that fashion to fit inside the box with its lid on. The bending of the cables resulted in them having more loss than the 1dB measured result at 10GHz.

3.3 COHERENT CARRIER DISTRIBUTION TESTING

The carrier distribution system was tested in three ways. Firstly, it was connected to a PSG and the power was individually measured at two of the output ports in order to test the two amplifiers. This experiment was repeated three times at 3.2GHz, 6GHz, and then 9GHz to observe any differences or irregularities in the gain plots. Secondly, a quick check was performed with a spectrum analyser to make sure the outputs were not distorted by large unstable harmonics. Thirdly, the carrier distribution system was integrated into the full measurement system with all PSGs connected so that any adjustments to signal power, discrepancies between PSGs etc, could be solved. This test was to validate whether all the PSGs could be locked, hence consisted of an instrument display check and any "UNLOCK" notification would constitute failure. Further to this test two PSGs, operating at 9GHz and 18GHz, were combined through a 90degree hybrid coupler and measured directly with the scope. A waveform capture at time zero and one approximately 4 hours later were performed to observe any discrepancy in the phase relationship between the fundamental and second harmonic signal.

Figures 5 and 6 show the gain plots for the both amplifiers over frequency. The amplifiers were driven to approximately the 1dB compression point. The port 1 and 2 amplifier can be seen to have a bigger spread in the measured gains than the port 3 and 4 amplifier. This is not a problem, as the spread in gain of both amplifiers is within the ±5dB tolerance of the input reference [8]; however it is worth using to decide upon the required input attenuation.

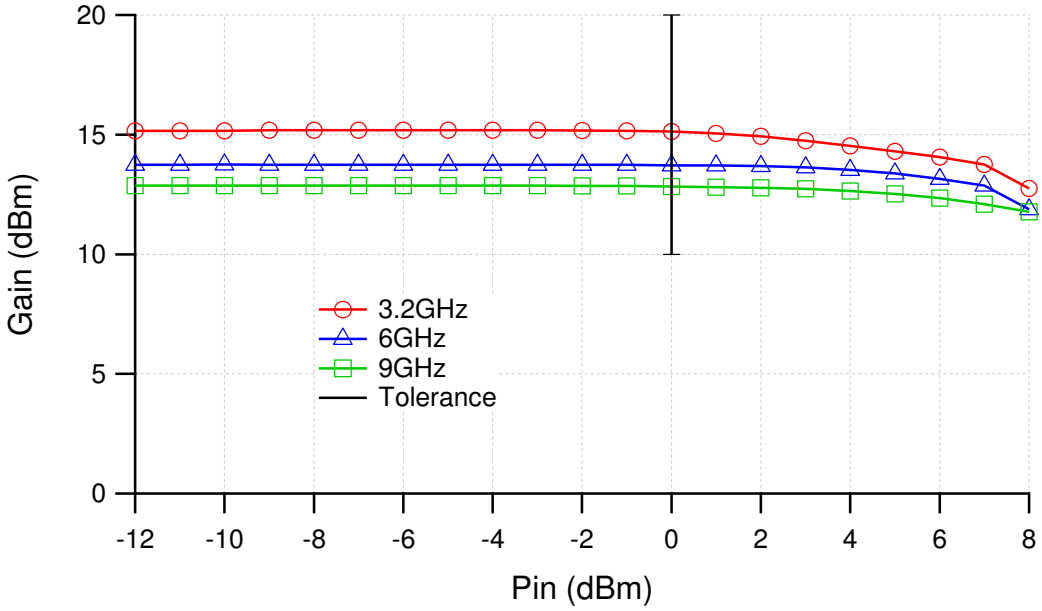

Figure III-5: Gain versus Pin plot for the port 1 and port2 amplifier and 10dB dynamic range (tolerance) of HCC input.

The measured power from the HCC option was approximately 15.3dBm over the whole frequency band, except at 10GHz where the power fell to 14.37dBm. Although this drop was unexpected it does fall in the ±5dB range of its own input reference [8]. In relation to the distribution amplifiers, this meant that a Pin of 0dBm or 1dBm would

have sufficed if there was no loss in the signal path after the amplifier.

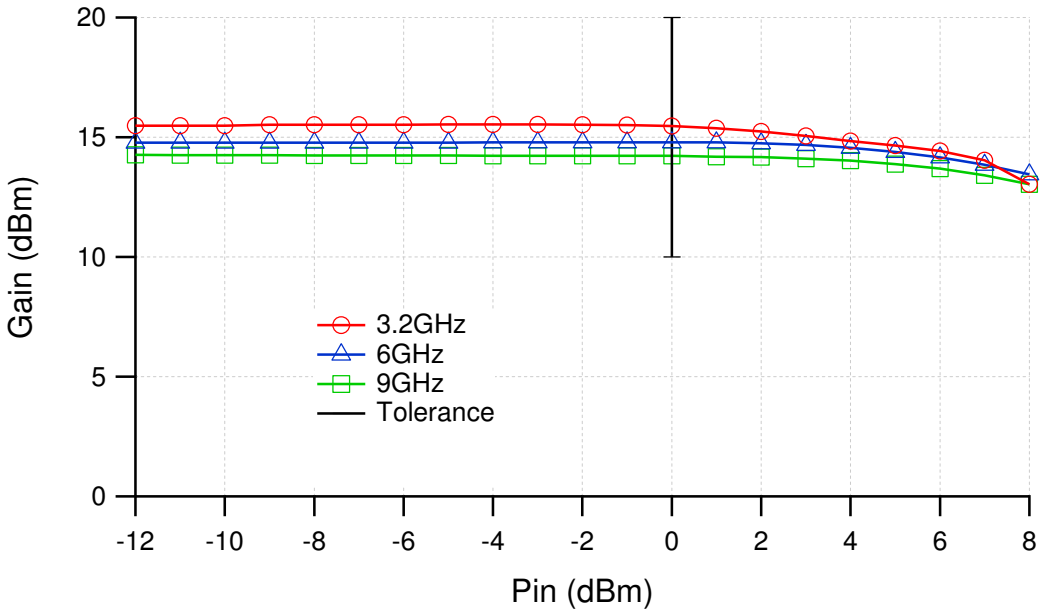

Figure III-6: Gain versus Pin plot for the port 3 and 4 amplifier and 10dB dynamic range (tolerance) of HCC input.

The distribution system was driven at 0dBm and 1dBm into a spectrum analyser for both amplifiers. In this test port 1 and port 4 were used so as to exercise both PAs. The harmonic content in both cases was below 20dBc of the fundamental output power.

Figure 7 shows a ±2dBm variation in the outputs of the distribution system until 9GHz. At 9GHz and 10GHz there is a drop in power with the lowest point being 10.68dBm. This, however, was not sufficient to cause any of the PSGs to become unlocked in the test condition. When measurements were performed it was noticed that

the PSG connected to port 4 became unlocked for some but not all of the measurement points. This discovery resulted in a reduction of the input attenuation of 1dB which resulted in consistent, stable carrier locking.

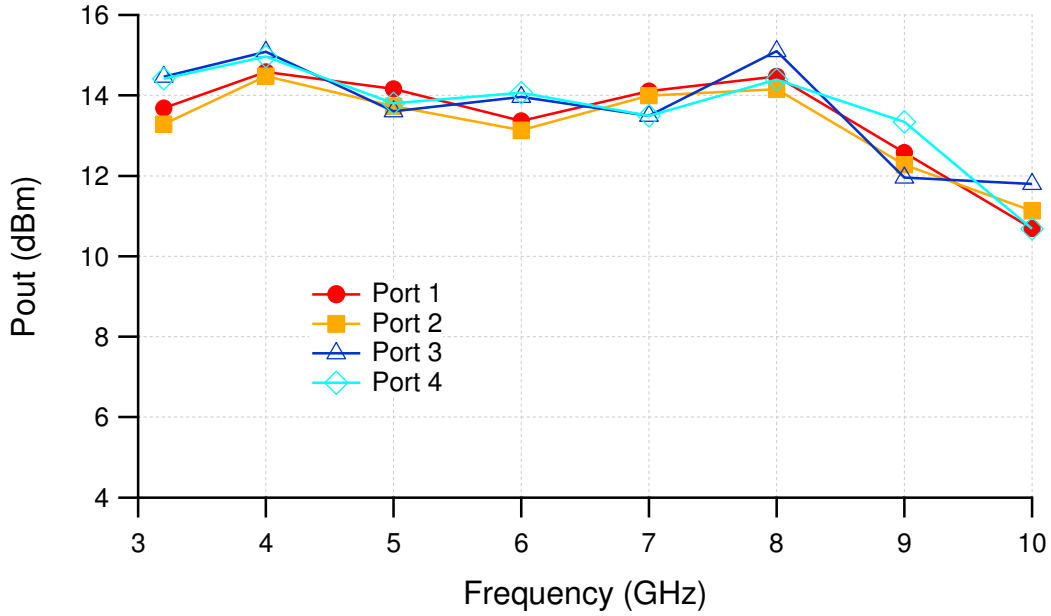

Figure III-7: Pout variation over frequency for the four ports of the distribution box.

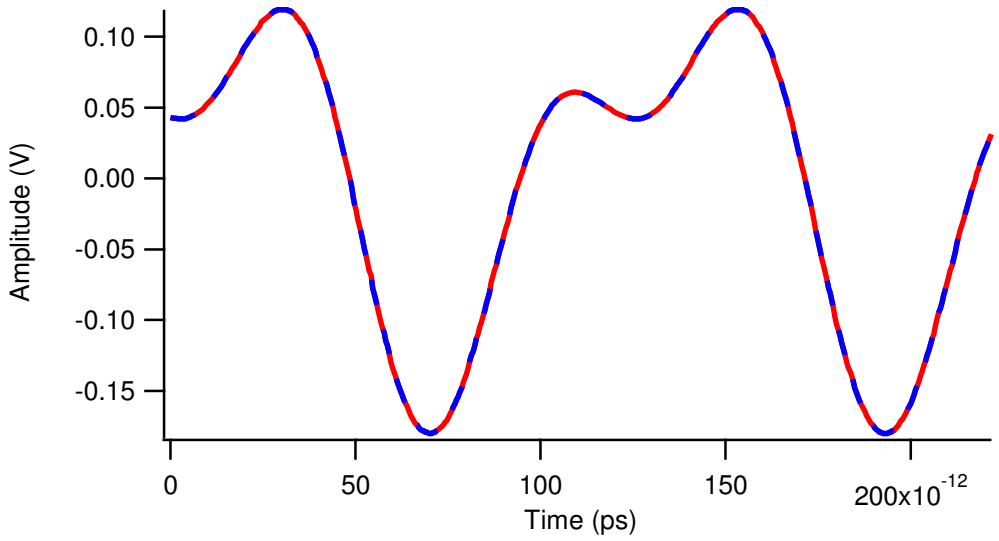

Figure III-8: A 9GHz and 18GHz combined signal captured at time = 0 (red trace) and 4 hours later (blue dashed trace).

Figure 8 shows the good alignment of the two traces take over a 4 hour period. The 9GHz and 18GHz signals have stayed locked in their phase relationship proving the carrier distribution system works over time.

3.4 SUMMARY

In order to be able to perform more complex load-pull device measurements additional signal sources needed to be added to the system. The most cost effective way of adding a signal source, was to make, in-house, a coherent carrier distribution system which could link four sources. Using a simple design platform the system was made from Mini-Circuits power dividers and amplifiers. Necessary padding was applied at the input due to the amplification of the Mini-Circuits amplifiers.

The carrier distribution system was tested with varying input power at 3.2GHz, 6GHz, and 9GHz to check that the amplifiers were performing correctly over the PSG's HCC option frequency bandwidth and input dynamic range. Furthermore, the system was tested with a spectrum analyser and the harmonic components were found to be lower than 20dBc for both PAs. The carrier distribution system was implemented in the measurement systems and test measurements were performed to observe whether the 'unlock' warning on any of the

PSGs appeared. The PSG connected to port 4 was noticed to become unlocked for some measurements not all. This finding resulted in a 2dB attenuation reduction and yielded reliable source locking. One further practical test was performed by combining two signals from the PSGs, one at 9GHz and one at 18GHz, and observing the change in the waveform over a 4 hour period. The test showed good alignment of the start and end waveforms hence device measurements over time would not suffer phase drift between harmonics. The inclusion of the coherent carrier system in the HF measurement system allowed for the first time harmonic load-pull to be performed at X-band.

The drawback of a hardware project like this is that they tend to be short term solutions and in this case future hurdles are obvious, since the coherent carrier distribution system only links a maximum of four signal sources. However, if one extrapolates upon the inner workings of figure 3, the addition of more and more sources will soon become costly, as more power dividers and amplifiers will be needed to expand the signal divide-and-amplify 'tree'. For future measurement system iterations it is suggested that signal source and measurement hybrid solutions be considered, Agilent's four-channel PNA [9] is a good example of what to aim for. However, addition of more sources would still be sought after although seven is an estimated maximum necessary for decades of research. Seven

sources would allow for three input and four output injections, or any other input/output configuration.

3.5 REFERENCES

[1] P. J. Tasker and J. Benedikt, "*Waveform Inspired Models and the Harmonic Balance Emulator,*" IEEE Microwave Magazine. Pg 38-42. Apr 2011.

[2] Tektronix "*Digital Serial Analyzer Sampling Oscilloscope DSA8200 Data Sheet,*" Downloaded from: http://www.tek.com/sites/tek.com/files/media/media/resources/85W_17654_20.pdf

[3] Agilent Technologies "*Z5623A Option K07 User's and Service Guide,*" Downloaded from: http://www.home.agilent.com/upload/cmc_upload/All/Z5623AK07Usersguide.pdf

[4] Agilent Technologies "*Agilent E8267D PSG Vector Signal Generator Configuration Guide,*" Downloaded from: http://www.cnam.umd.edu/anlage/Microwave%20Measurements%20for%20Personal%20Web%20Site/5989-1326EN.pdf

[5] S. Woodington et al, "A Novel Measurement based Method Enabling Rapid Extraction of a RF Waveform Look-Up Table Based Behavioural Model," IEEE MTT-S International. Pg 1453-1456. Jun 2008.

[6] Mini-Circuits "*Coaxial power Splitter/Combiner ZFRSC-183+,*" Downloaded from: http://217.34.103.131/pdfs/ZFRSC-183+.pdf

[7] Mini-Circuits "*Super Ultra Wideband Amplifier ZVA-183+,*" Downloaded from: http://217.34.103.131/pdfs/ZVA-183+.pdf

[8] Agilent Technologies "*Agilent E8267D PSG Vector Signal Generator Data Sheet,*" Downloaded from: http://www.keysight.com/en/pd-680840-pn-E8267D/rear-panel-connections-for-multi-source-phase-coherency-special-option?cc=GB&lc=eng

[9] Agilent Technologies "*N5242A PNA-X Network Analyzer,*" Downloaded from: http://www.home.agilent.com/en/pd-867173-pn-N5242A/pna-x-microwave-network-analyzer?&cc=GB&lc=eng

CHAPTER IV
CAD IMPLEMENTATION IMPROVEMENT

The investigations by Woodington et al [1-3] were predominately concerned with analysis of the model structure and accuracy with respect to fundamental only and fundamental and second harmonic load-pull measurements. There was some effort to implement a usable CAD implementation; however, the end result had a rigid formulaic structure in Agilent ADS that would only simulate with a particular file containing a specific number of coefficients. This chapter will detail the process of implementing a dynamic model solution within the CAD environment that was necessary to prevent future model-simulator integration problems arising from the myriad models that can be generated with a flexible model extraction procedure.

4.1 INTRODUCTION

The Cardiff Model has been developed, over the years, to be as flexible as possible. The relevant contrast to this being Agilent's, X-parameter, approach that uses a fixed formulaic structure. Chapter II mentioned that the synergy between X-parameter data files and Agilent's ADS harmonic balance simulator was good. The Cardiff model has yet to reach the usability or the speed of simulation exhibited by Agilent's X-parameter solution.

Figure 1 shows the core of a current iteration of the ADS implementation of the Cardiff model. It utilises a four port Frequency Domain Device (FDD) to extract and compute the port incident and reflected travelling waves. The FDD has four ports because it needs to perform operations on the DC current and AC voltage and ADS does not support single ports that can do operations on both quantities simultaneously.

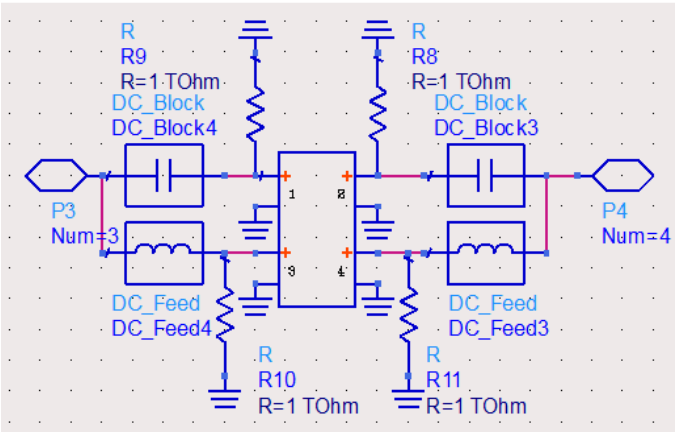

Figure IV-1: FDD core of the model schematic.

```
FDD4P
FDD2P1
I[3,0]= real(OutputXParam(Q1,r00I10,r10I10,rn10I10,r01I10,mag_a21))
V[1,1]= Vp11+OutputXParam(Q1,r00b11,r10b11,rn10b11,r01b11,mag_a21)*P1
V[1,2]=Vp12+OutputXParam(Q1,r00b12,r10b12,rn10b12,r01b12,mag_a21)*P1*P1
V[1,3]=Vp13+OutputXParam(Q1,r00b13,r10b13,rn10b13,r01b13,mag_a21)*P1*P1*P1
I[4,0]= real(OutputXParam(Q1,r00I20,r10I20,rn10I20,r01I20,mag_a21))
V[2,1]=+( Vp21+OutputXParam(Q1,r00b21,r10b21,rn10b21,r01b21,mag_a21)*P1)
V[2,2]= (Vp22+OutputXParam(Q1,r00b22,r10b22,rn10b22,r01b22,mag_a21)*P1*P1)
V[2,3]=(Vp23+OutputXParam(Q1,r00b23,r10b23,rn10b23,r01b23,mag_a21)*P1*P1*P1)
```

Figure IV-2: The FDD port equation set.

A Data Access Component (DAC) is used to read the generated model file and assign coefficient values in the file to their respective ADS variables. In this iteration there are 8 variables in the file over four harmonics for two ports, yielding a total of 64 variables. Any changes to the file need to be repeated in the schematic layout in ADS and vice versa otherwise the simulator will not converge.

Figure IV-3: The DAC and file variable layout.

The equations highlighted in figure 2 reconstruct the harmonic waveform components from the model coefficients and the renormalized FDD port values. The equation sets that are used, as well as the file's coefficient composition, are rigid and hence do not permit any other model type or complexity.

The rigid CAD implementation poses significant problems for anyone wishing to increase model complexity and if three harmonics are used to create a model the equations would get cumbersome to implement by hand. The solution to these problems was native to the model generation software; however, there was no obvious way to implement the IGOR Pro [4] code in Agilent's ADS. This chapter will now demonstrate the process of creating a dynamic CAD implementation of the Cardiff Model within ADS.

4.2 Creating a Dynamic CAD Model Solution

Fundamentally, the only thing wrong with the old solution was that developing ADS templates for the many instances of different model implementations was impractical and could be prone to error. The solution is to perform the long-hand power series summation calculation using matrix formations, this way there would be a specific number of variables in the CAD schematic window, but they

could be changed more easily than rewriting the long-hand equations.

4.2.1 AEL in ADS

AEL is ADS' Application Extension Language (AEL). Agilent describe it as a general purpose programming language modelled on C. Similar to C, AEL has sets of native functions to handle file I/O, database queries, mathematics, lists, and string manipulation. The way AEL is integrated with ADS means that it has different functionality in the various windows you can access. The model implementation will only occur in the schematic window; hence the function set specific to this window will be the one that can be used.

By virtue of AEL being a tool used to add extra functionality and aesthetics to the core ADS program AEL procedures cannot be called and run whilst the simulator is performing calculations see figure 3. This flow diagram seems sound to begin with, however for an AEL script to interact with an ADS simulation in this way ADS' flow diagram would have to be structured differently. As it is, when the user hits 'run simulation' all the data in the schematic hierarchy gets written to a Netlist that the simulator uses in its operations before stopping and creating a data set for the data display window to use. Therefore, the AEL script cannot be used to do parallel work during

simulation, however, it can be used to populate the schematic window with the appropriate functions for the harmonic balance simulator to use itself.

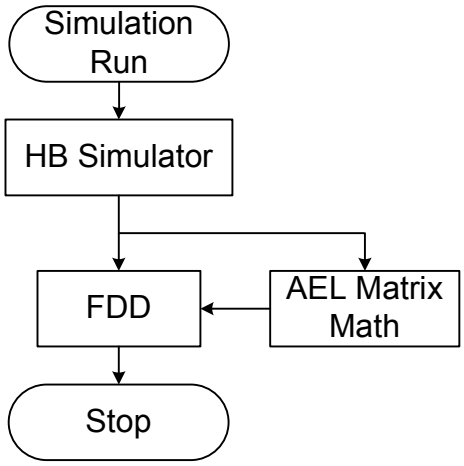

Figure IV-3: Flow diagram of ADS-AEL simulation.

4.2.2 The Cardiff Model File

The model file format used by Woodington does the job for two types of model, namely the ones shown in [3]. The file output program did not support any other type of model hence needed to be upgraded so that it could be more flexible and more in line with the qualities displayed by the model formulation.

The file type was structured in a way that for each header name there was a specific value in the data. With this structure ADS can easily

assign variables that point to the specific header, which in turn has its own data. The issue that presented itself here is that whilst the file header names were specific they were not index-friendly and were essentially hand typed and written to the file. This meant a more general index-based header name would have to be used, e.g. R21_0. In this case 'R' is just the letter for all the model coefficients '21' indicates port and harmonic respectively, and '_0' then denotes the index, or the line number. This header type can be used by ADS in retrieving data, provides position in a 2D data space, and can be written to a file by using a programming loop. Whilst it can be helpful for the user to know which coefficient is which, a computer does not need to know this and it can introduce unnecessary complexity. Nevertheless, for the user's sake, a separate file could be written that indicates what the indexed coefficients are in terms of the model. Table I shows, for an X-parameter scenario, what the output second harmonic column and its description would look like.

Table IV-I: Example dataset and description for the output second harmonic.

Description	**Example Dataset**
XF21_0	R21_0
XS21_1	R21_1
XT21_1	R21_2
	(Complex Number)_0
	(Complex Number)_1
	(Complex Number)_2

It is not assumed that this is the final and best iteration of the model file; rather, it is a step in the right direction. It is clear that as more complex models are made more coefficients will be created. With the header to data ratio being 1:1, that means for a single data block half of the file size is allocated just for headers; this is without consideration of the data block headers. This is not ideal but it provides a solution to file interactions with the schematic window in ADS.

4.2.3 Designing the AEL Script

Knowing that AEL could be used to populate the schematic window was useful; however, it did not immediately present a solution to the problem of a dynamic model implementation. AEL has functions to operate on lists and arrays, which can both be multidimensional. However, mathematical operations, akin to matrix algebra, can only be performed on arrays and via heuristic testing it was found that the schematic window did not support arrays, hence matrix algebra could not be performed in the schematic window. The solution to this, given the way AEL can be applied to ADS, is to use AEL to populate the model schematic window with long-hand formulas and functions that can execute the matrix calculations, albeit in a long winded way. The AEL script can now be thought of as a by product of a schematic design for the model. Therefore, after having decided on the functions and variables that will be necessary for operation, ADS'

command line window can be used to find the code necessary to draw schematic objects onto the window.

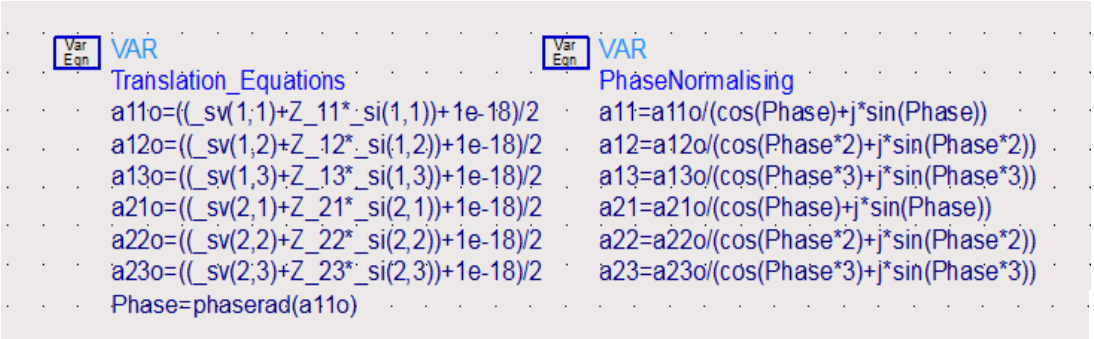

Figure IV-4: V-I to a-b translation equations and equations for phase normalisation.

Figure 5 shows the equations for extracting the scattering wave components from the ports of the FDD and the required renormalization to bring the phase of $a_{1,1}$ to zero. It should be noted that the $1x10^{-18}$ is in the translation equations to eliminate the occurrence of zeros in future calculations, hence eliminate the computation of NaNs (Not a Number) when division or indices are being applied. It is not then taken out of future equations as its value introduces an error far less than measurement error.

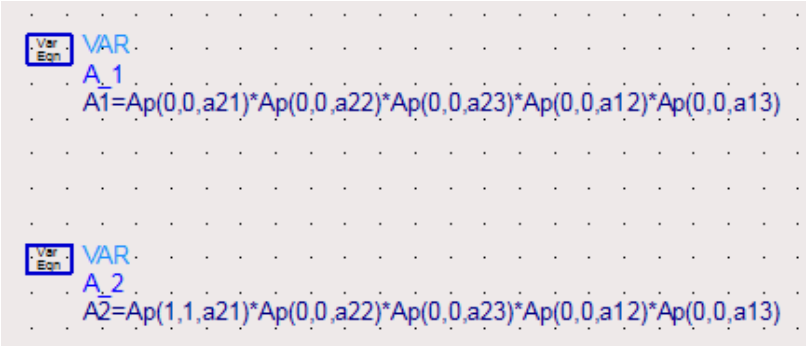

Figure IV-5: A-element calculations.

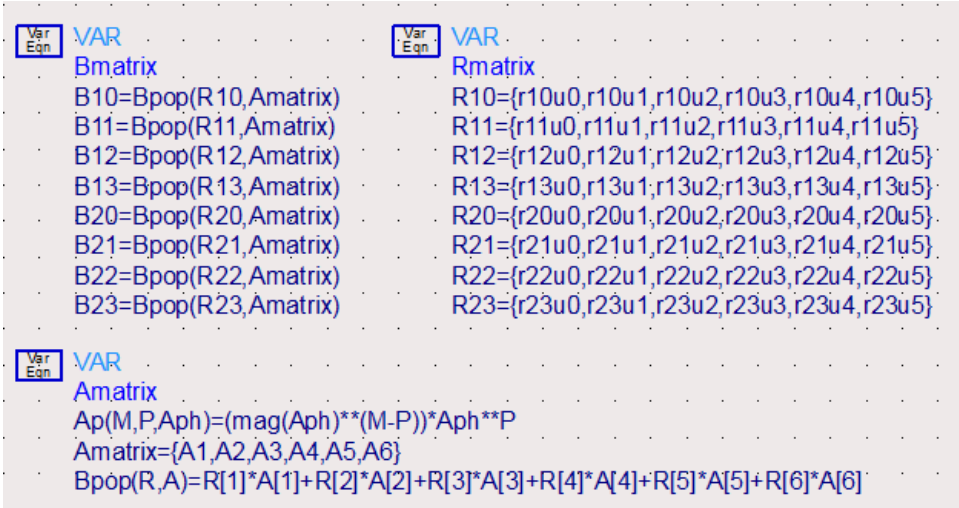

Figure IV-6: Construction of the B matrix using the R matrix, and A matrix equations.

Figures 6 and 7 show the equations that allows for the ultimate, simple, operation of [B] = [R] x [A] to be able to calculate the response of the model for the applied stimuli. The elements of the Amatrix are calculated by taking the phase-normalised incident waves and raising them to the power of the same magnitude and phase powers of the intended coefficients. The coefficients are read from a '.txt' file and used to populate the first two elements of the Ap(M,P,Aph) function in figure 6. Each element in the Amatrix list relates to a different model coefficient. The lists in the Rmatrix variable denote columns in the model file being read by the DAC. The Amatrix and Rmatrix composition means that the function of Bpop(R,A) is to simply execute a power series multiplication and summation of terms.

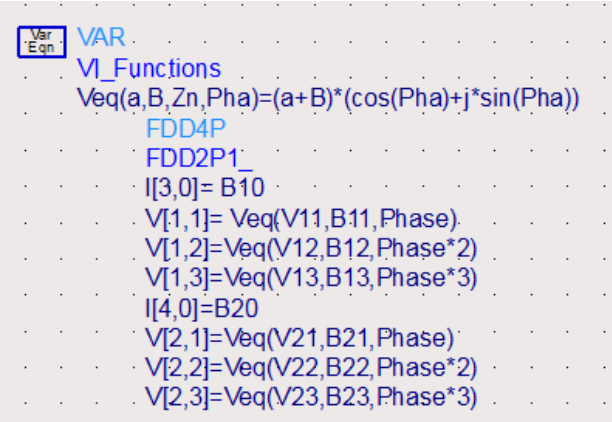

Figure IV-7: The FDD functions.

After the waveforms have been constructed by the power series all that is left is the addition if the phase of $a_{1,1}$ to de-normalize the end result. The V[p,h] and I[p,h] FDD variables in figure 7 apply calculated quantities to the respective port 'p' and harmonic 'h' of the FDD. The Veq(a,B,Zn,Pha) function calculates the port voltages and adds the phase of $a_{1,1}$ back into the response, therefore undoing the phase normalization seen in figure 4.

It was mentioned before that the ADS command line window could be used to find the code for drawing and editing objects on the schematic window. When the command line window is open the user can view the code that is linked to all the operations performed on the schematic window and the contained objects. This made the schematic-population code much easier to implement.

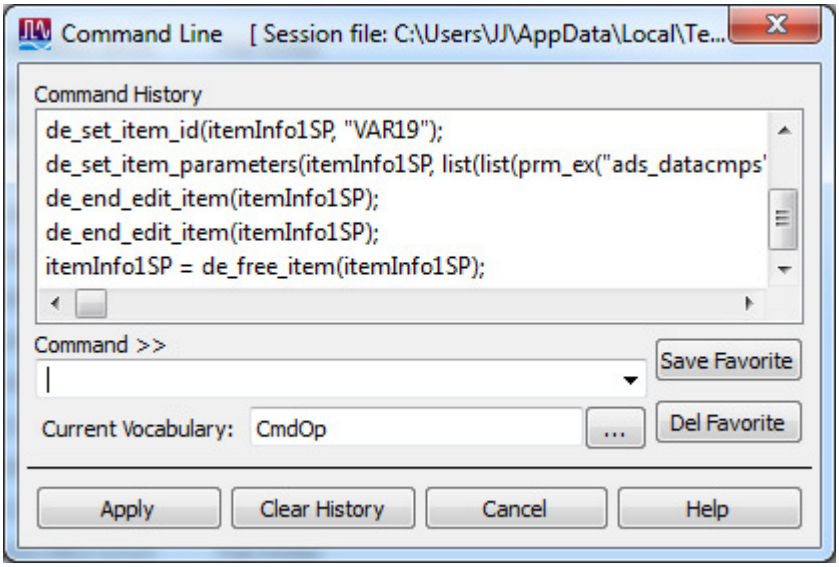

Figure IV-8: The command line window displaying code that sets schematic variables

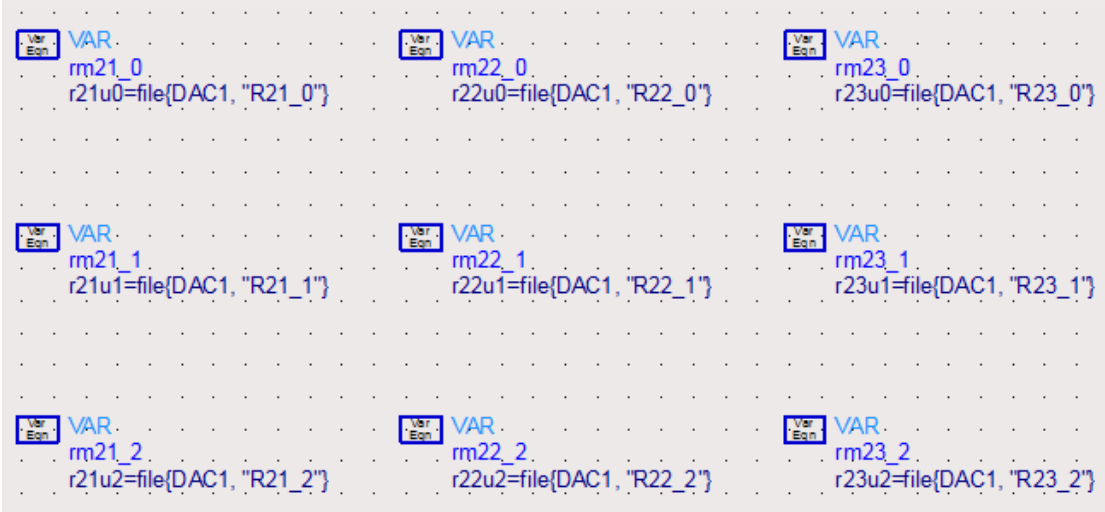

Figure IV-9: Data access file variable layout.

The utilization of the command line window enabled planning when it came to the layout of the data access variables. In principle there is not a problem with combining each variable in the VAR blocks, in

figure 9, so that the harmonic access variables are grouped. However, the function used to write the VARs to the schematic window is inherently a long string and each access variable that is added would make it longer and more unusable. This issue is a sticking point as the programming environment allows for string variables but not if the string variable represents a function, or part of a function, that writes to the schematic window. A solution, presented in figure 9, would be to loop the schematic write process and only write one variable to each VAR.

4.2.4 Testing the AEL Script

The testing procedure was laborious since ADS is not a programming environment, rather a simulator, hence a text based program was used to write the code, and with that semantics checks had to be left until run-time. Nevertheless, functions were written for loading the coefficient, model, and impedance files into arrays, as well as a function to operate on the data and write it to the schematic window. Each function was run via a load command in the command line window (load("testAEL.ael")). The AEL debugger was used by calling it in the AEL script at the end; this allowed the programme to be stepped through which made pinpointing any errors easier.

Apart from debugging functions within the code, crude comparison was made between an X-parameter simulation and a Cardiff Model simulation for the same model complexity. Although simulation within the modelled area was achieved by both approaches there was a difference in simulation time. The harmonic balance simulator, once operating, seemed to iterate through the calculations in both cases at the same rate. The time discrepancy can therefore be attributed to a loading time necessary for the simulator to retrieve the data in the model file via the DAC component into a Netlist prepared for simulation. The loading time is rather obvious, as the X-parameter simulation would begin in less than two seconds, whereas the Cardiff Model simulation would begin at about ten seconds. By virtue of the delay being attributed to a file load, the associated loading time is directly proportional to the model file size; meaning that very large model files would have very long loading times before the simulator could perform any calculations. A solution to this, in the future, would be to directly write the Netlist of the model schematic, thus simultaneously performing the time consuming file load ahead of run-time and once only. The most annoying trait of the simulations is the cumulative waste of time that builds up over a period of simulator use. However, the Netlist solution would be the next organic progression because without a schematic of a working dynamic solution, one cannot be certain of the form of the Netlist. The model implementation was also tested with a model file that had 215 coefficients; this was to see if there would be any issue in

computer memory for writing the ADS schematic window. The resulting issue was not memory related; rather, it was related to the Bpop(R,A) power series function. The string that needed to be populated to the schematic somewhere in either the AEL program or when it is written to the schematic window caused ADS to unexpectedly close down with no error. Since the Bpop(R,A) function only performed multiplication and summation operations it was split up into multiple functions with 50 or less summations, which solved the crash problem.

4.3 SUMMARY

This chapter has detailed the process and rationale behind the development of the Cardiff model implementation. The conversion to a dynamic solution presented challenges both inside and outside the CAD environment. The root problems lie in the model file structure and the formulaic representation of the model in ADS; however, the two were not entirely separate entities. The model file was changed so that index-based headers were used, which allowed for easier file writing in IGOR Pro, and file reading in AEL. The AEL program was initially designed in a top-down way so that the schematic window's functions could be tested and so an appropriate layout could be obtained via the command line window. After the basics had been finalised the intricacies of the implementation were examined and improvements were made in the way the program handles the long

power series summation string. In terms of simulation, the model solution is slower than the X-parameter model block that has been optimised for ADS. The difference in speed is due to the different file processes the two methods go through. Since the X-parameter blocks have the data pre–loaded into memory it can operate on the data almost immediately. However, for the Cardiff model, the data has to be read into the schematic each time a simulation is run, which results in a loading time, proportional to the size of the model file, before ADS can do any operations on the data. This model implementation consequently has shown a disadvantage of using DACs. A possible solution to this, which could be implemented in the future, is to compile a Netlist for the model schematic using AEL. This way all the data would be contained in the Netlist and the process would not necessitate additional loading of data.

4.4 REFERENCES

[1] S. Woodington et al, "A Novel Measurement based Method Enabling Rapid Extraction of a RF Waveform Look-Up Table Based Behavioural Model," IEEE MTT-S International. Pg 1453-1456. Jun 2008.

[2] S. Woodington et al, "*Behavioural Model Analysis of Active Harmonic Load-Pull Measurements,*" IEEE MTT-S International. Pg 1688-1691. May 2010.

[3] S. Woodington, "*Behavioural Model Analysis of Active Harmonic Load-Pull Measurements,*" Doctoral thesis submitted to Cardiff University. 2012.

[4] WaveMetrics "*IGOR Pro Product page,*" Downloaded from: http://www.wavemetrics.com/products/igorpro/igorpro.htm

CHAPTER V
SOURCE- AND LOAD-PULL BEHAVIOURAL MODEL ANALYSIS

Recently, it has been common to generate models for output fundamental load-pull data only. Sometimes, the procedure is stretched to include output second harmonic load-pull for applications such as amplifiers operating in the Class-B to Class-J continuum. These are modes of amplifier that have and optimum fundamental impedance and short circuit second harmonic impedance. The work in this chapter goes even further by investigating the required model necessary to describe input second harmonic variations and then its relationship with the output fundamental and second harmonic models. In addition, coefficient truncation is investigated with the aim of potentially reducing model file sizes for model types describing multi-harmonic interactions. Furthermore, the models are used in ADS for the analysis of input

second harmonic shorting and other cases that have an impact on future HF measurements and design.

5.1 INTRODUCTION

In chapters III and IV it was shown how the measurement system was augmented to accommodate second harmonic source-pull along with fundamental and second harmonic load-pull, as well as detailing the improvements to the CAD implementation. In this chapter, a Gallium-Arsenide (GaAs) pseudomorphic High Electron Mobility Transistor (pHEMT), operated at a frequency of 9GHz, will be used to demonstrate model relationships between the input second harmonic and output harmonic load-pull data sets.

5.2 MEASUREMENT OF SOURCE- AND LOAD-PULL MODELS

The investigations performed by Woodington et al in [1-3] utilised measurement points on concentric circles to extract the relative phase relationship between the stimulating signals. Taking a fundamental only load-pull power sweep case as an example, the coefficients that would be extracted can be seen as a function of the varying operating conditions.

$$R_{p,h} = P_1^h . G_{p,h}\left(|a_{1,1}|, |a_{2,1}|, \frac{Q_1}{P_1}\right) \quad \text{(V-1)}$$

Where $R_{p,h}$ are the model coefficients that are a function of the phase normalised the measurement parameters, having subscripts 'p' and 'h' denoting port and harmonic index respectively. P_1 is the phase of $a_{1,1}$ and Q_1 is the phase of $a_{2,1}$.

In equation 1 the bias and frequency are left out because they would be constant for the entire sweep. If the arguments of G, in equation 1, are broken down into measurement iterations the equation can be simplified to:

$$R_{p,h} = P_1^h . G_{p,h}\left(\frac{Q_1}{P_1}\right) \quad \text{(V-2)}$$

Where equation 2 now represents static $|a_{1,1}|$ and $|a_{2,1}|$, and the final argument left is the relative phase response of the system for a given drive power and output fundamental power. Now, if it is supposed that the iterations of phase Q_1 coincide with iterations with output fundamental power. The $|a_{2,1}|$ argument now becomes part of equation 2:

$$R_{p,h} = P_1^h . G_{p,h}\left(\frac{|a_{2,1}|Q_1}{P_1}\right) \qquad \text{(V-3 \& 4)}$$

$$or \quad R_{p,h} = P_1^h . G_{p,h}\left(|a_{1,1}|, \frac{a_{2,1}}{P_1}\right)$$

Essentially, this reverses the component segmentation performed in [1-3]. From a graphical point of view, this operation represents a spiral of load points, whereas before concentric circles were used. The equations 3 and 4 still show that the relative phase relationship can be extracted on its own and hence create the phase related polynomials of $R_{p,h}$.

The motivation behind this move from concentric circles was that spirals would more efficiently cover impedance areas of interest. This would reduce the number of points necessary to complete a harmonic data set and a reduction in points scales with measurement time, hence less time would be needed to complete the measurements. A time reduction is necessary as the addition of the input second harmonic to a measurement sequence increases the number of measurements multiplicatively.

5.2.1 Measurement Sequence

The measurement software used at Cardiff University, developed by Saini [4], could cope with single harmonic grids well. The functionality for two harmonic load-pull was also sound when using Newton-Raphson impedance convergence, which is a way of iteratively computing a better approximation to the roots of a function. The issue presenting this work was that there was no inbuilt utility for spiral $a_{p,h}$ grids. As a result, a supplementary piece of software was written that would create a measurement procedure data table that would be executed by the measurement software. It contained all the injected a-wave quantities for the whole sweep as well as the fundamental operating conditions: bias and frequency. The file could be loaded into the Cardiff measurement software and run like a normal grid, except the grid was unable to be viewed. This disconnect between the two programs lead to the authors adherence to a specific methodology in order to converge upon the correct measurement test. The measurements were prioritised so that more a-wave grids were performed at the higher harmonics on the input and output when compared to $a_{2,1}$. Moreover, in the case where just $a_{1,2}$ and $a_{2,2}$ were perturbed, the device was more sensitive to movement of $a_{1,2}$ therefore the measurement was designed so that it was in the outer iterative loop in figure 1. When the focus is on $a_{1,2}$ and $a_{2,2}$ this is sensible, although there are many other measurement scenarios where this is not the case.

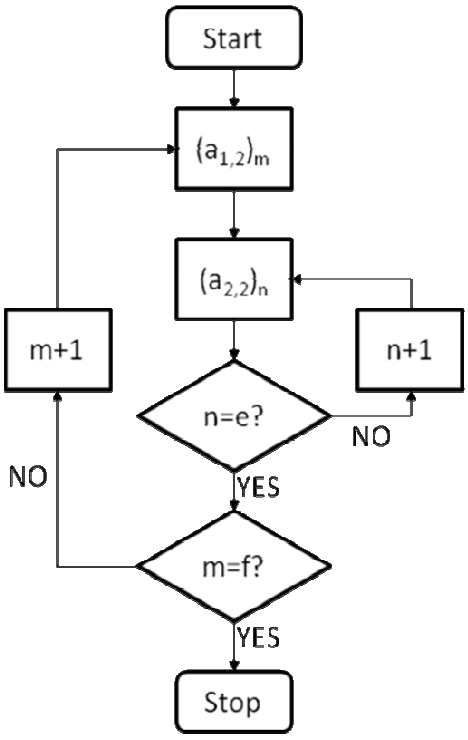

Figure IV-1: A flow diagram of the measurement methodology.

Figure 1 describes the nested a-injection measurement sequence for input and output second harmonic perturbations. For $a_{2,2}$ 'n' iterates until 'e', which is the number of points in the $a_{2,2}$ grid. From there, 'm' is iterated once and 'n' resets to zero before iterating to 'e' again. This whole process is repeated until m=f, as this is where all points in the $a_{1,2}$ spiral have been measured. The number of measurements form this process is therefore 'e' multiplied by 'f'. The a-injections can be replaced by any combination of input and output harmonic perturbations to obtain variants of the same nested measurement scenario.

5.3 ANALYSIS OF THE INPUT SECOND HARMONIC MODEL

Previous work has shown the development of the Cardiff model formulation, different to the X-parameter approach, so that more accurate behavioural representations can be achieved when measuring performance at high mismatched states. This predominantly involves the introduction of a coefficient that accounts for quadratic variation of magnitude. The introduction of the input second harmonic in to the model needs to be investigated progressively. At first, in terms of model expansion, the Input second harmonic will be looked at on its own. However before this, the expansion of the model formulation will be looked at.

5.3.1 Augmenting Model Formulations

The work in [1-3] shows, in detail, the significance of the terms in the model formulation past the three terms at the beginning, which are the X-parameter terms. Most importantly is the introduction of the X_F^2 term that accounted for an observed centre shift of the data. However, the addition of more coefficients in the model, although increasing model accuracy, can have consequences.

The problem lies in the DC components of the model. Since DC is important, especially if one is to calculate efficiency from modelled

data, it is important that errors are prevented. The fundamental component of a GaAs pHEMT has been modelled in two ways in order to exemplify correct model augmentations. Figures 2(a) and 2(b) represent the model coefficients with phase exponents (n) in the output fundamental plane. These 'dot-graphs' are useful to see the coefficient complexity and coefficient importance over many harmonic dimensions. They show two cases for the output fundamental coefficient distribution; here the size of the dot represents the coefficient's significance in the model. When modelling strong nonlinearities, one might require the addition of more coefficients to get the accuracy of fit to an acceptable level. Asymmetry of the coefficients in the phase domain, however, is to be avoided. An asymmetric model formulation can be defined as a model formulation whose maximum phase exponent is not equal to the absolute maximum conjugate phase exponent. The input and output ports DC are displayed in figures 3 (a), (b), (c), and (d).

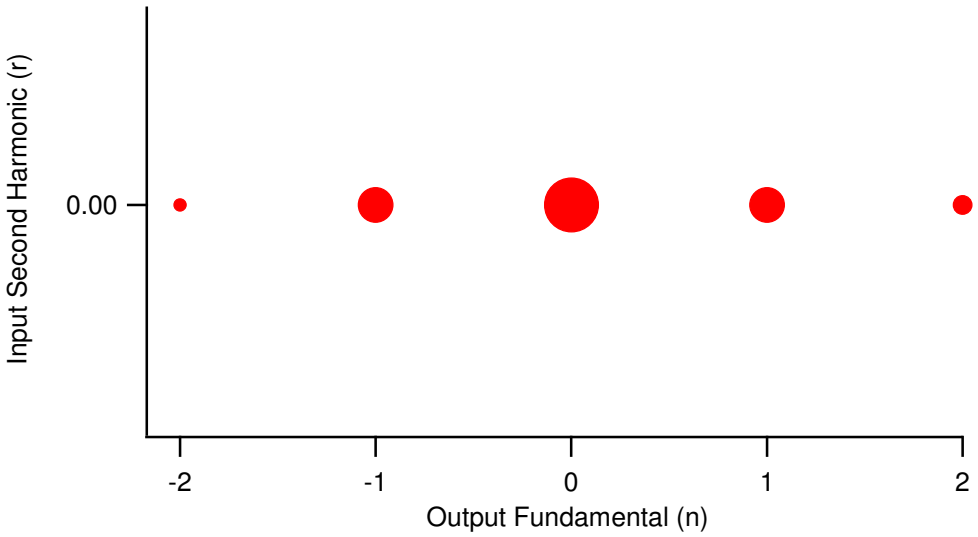

Figure IV-2(a): Symmetric-in-phase coefficient distribution.

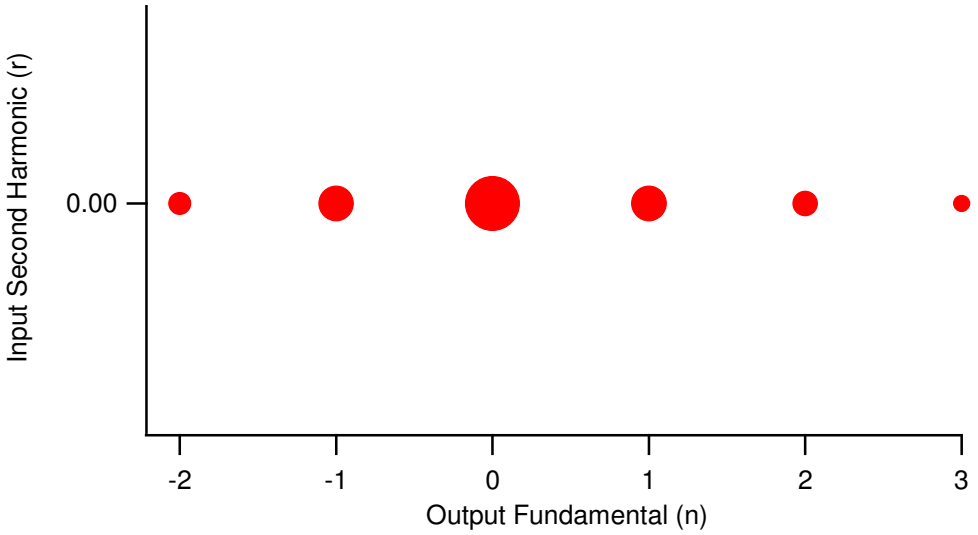

Figure IV-2(b): Asymmetric-in-phase coefficient distribution.

It can be seen that a symmetry-in-phase coefficient distribution results in a DC model with conjugate pairs that, in a power series, have imaginary components that cancel leaving a real DC component.

Asymmetric coefficient distributions must be avoided, as they yield imaginary DC components.

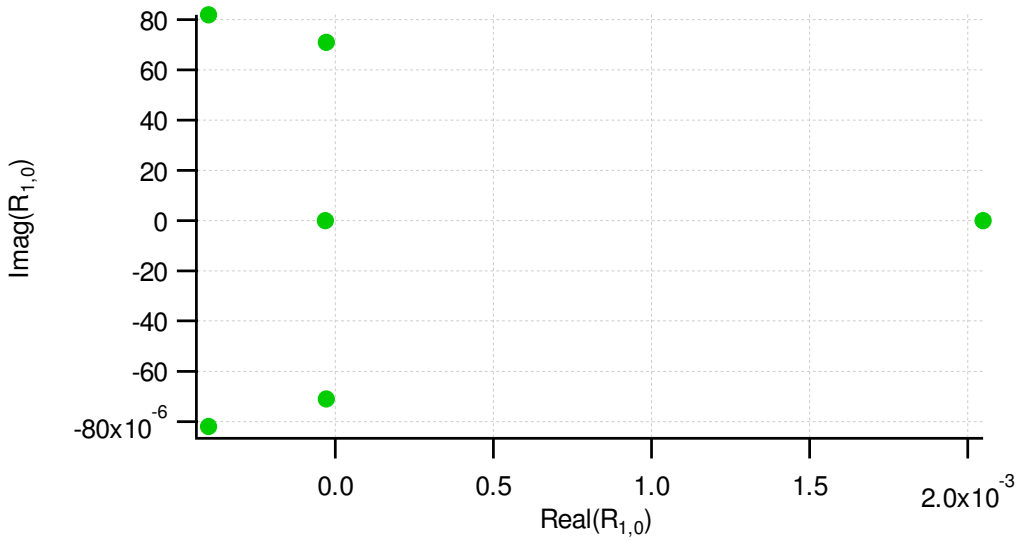

Figure IV-3 (a): Input symmetric DC coefficient data.

It can be seen that if the values in figures 3(b) and 3(d) were summed the result would have and imaginary component, whereas the imaginary components in figures 3(a) and 3(c) are symmetric about the real axis hence cancel leaving only a real component.

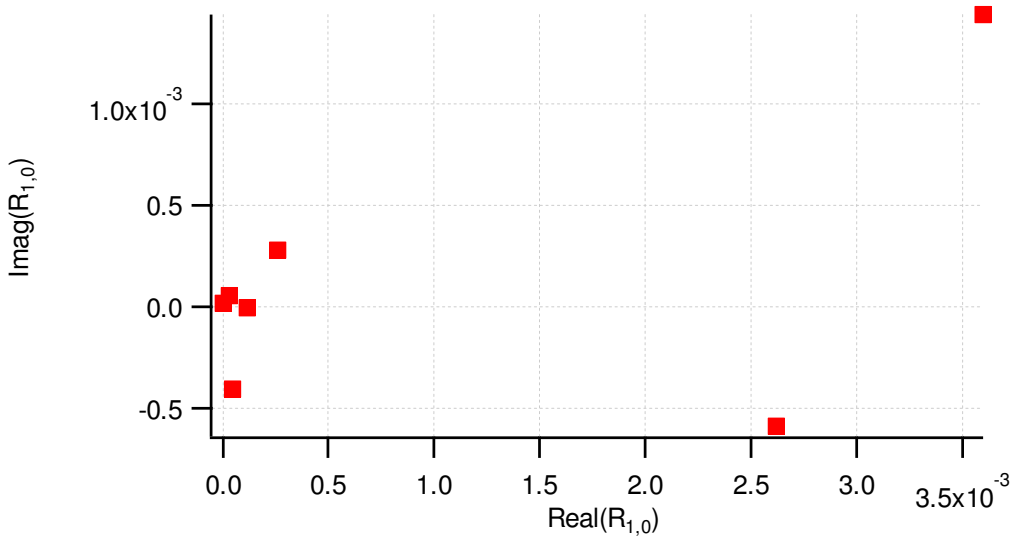

Figure IV-3 (b): Input Asymmetric DC coefficient data.

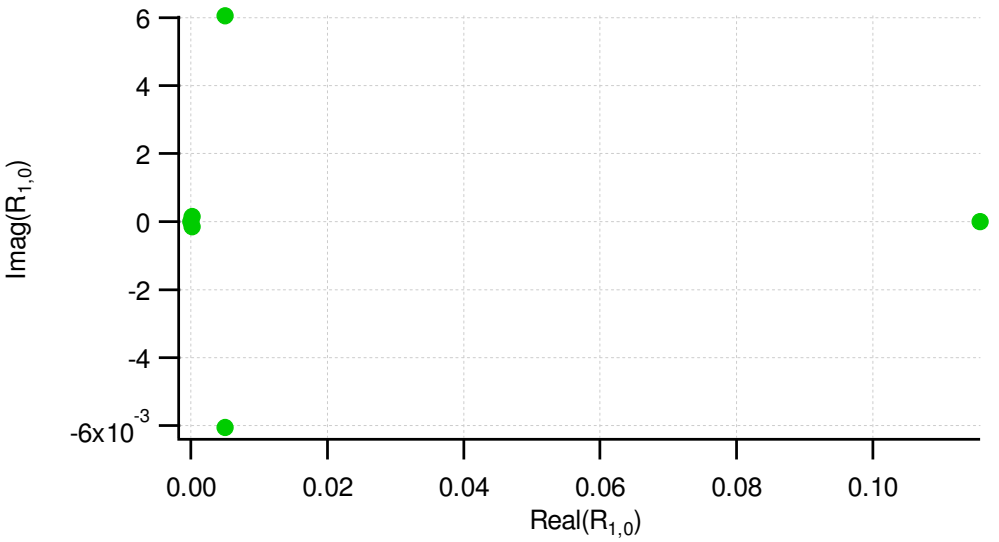

Figure IV-3 (c): Output symmetric DC coefficient data.

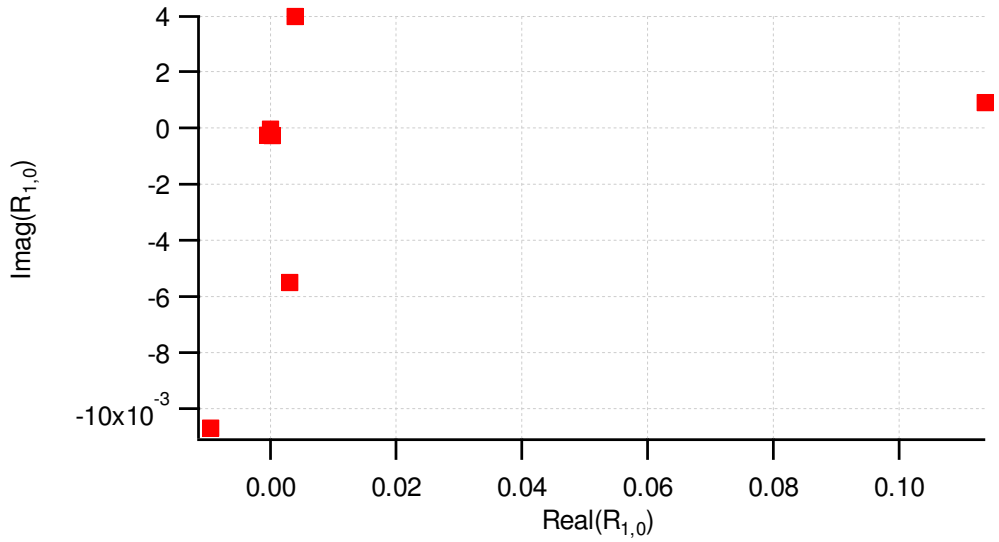

Figure IV-3 (d): Output Asymmetric DC coefficient data.

The same is true for the output cases and hence a phase coefficient and its conjugate should always be added to the model formulation if increased accuracy is required.

5.3.2 Isolation of the Input Second Harmonic

This investigation will utilise measurement data collected for a fundamental output and input second harmonic model. The input second harmonic component has been isolated in the data by filtering the data for a specific magnitude of a_{21}. The question that needs answering is: what input second harmonic model complexity is sufficient at modelling the device's response? In the following equations and figures the model formulation will be augmented and the associated model fit to the measured $b_{p,h}$ data will be shown so that improvements to model fit can be observed.

$$b_{2,1} = R_F\left|a_{1,1}\right| + R_S\left(a_{1,2}\right) + R_T\left(a_{1,2}{}^*\right) \qquad \text{(V-5)}$$

Equation 5 represents the X-parameter coefficients set, where R_F=X_F, R_S=X_S, and R_T=X_T when equating model coefficients. The asterisk (*) signifies the complex conjugate. In terms of the input second harmonic response, the model fit is good. Figure 4 shows good agreement between the modelled and measured responses and this is true for the b_{11} and b_{22} responses.

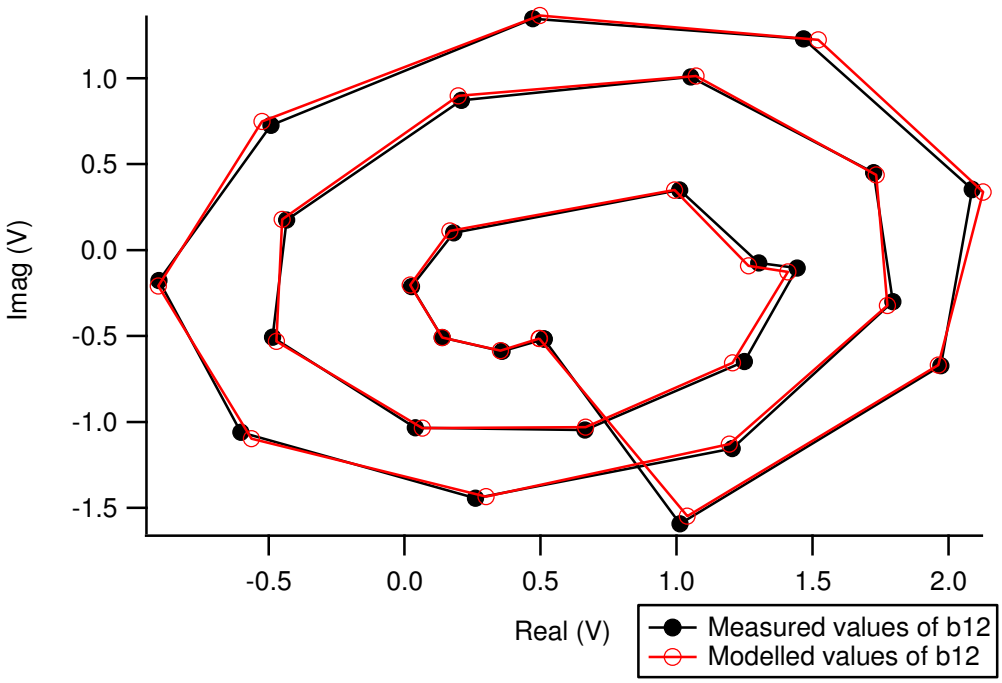

Figure IV-4: Measured versus modelled b_{12} responses from a set of harmonic source- and load-pull measurements.

The b_{21} response, on the next page, does not present a good fit. In Figure 5, the modelled response can be seen as elliptical and hence typical of the type of nonlinearities expected to be modelled by an X-parameter coefficient set. Augmentations to the model formulation should result in the shape of the b_{21} measured data being better described by the model.

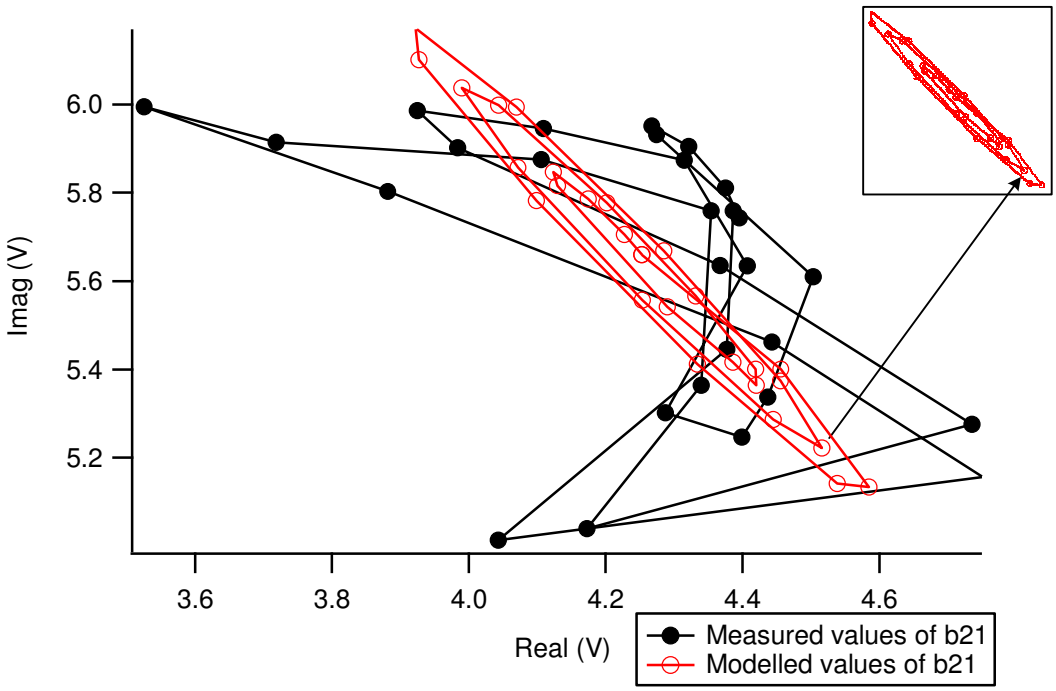

Figure IV-5: Measured versus modelled b_{21} responses from a set of harmonic source- and load-pull measurements.

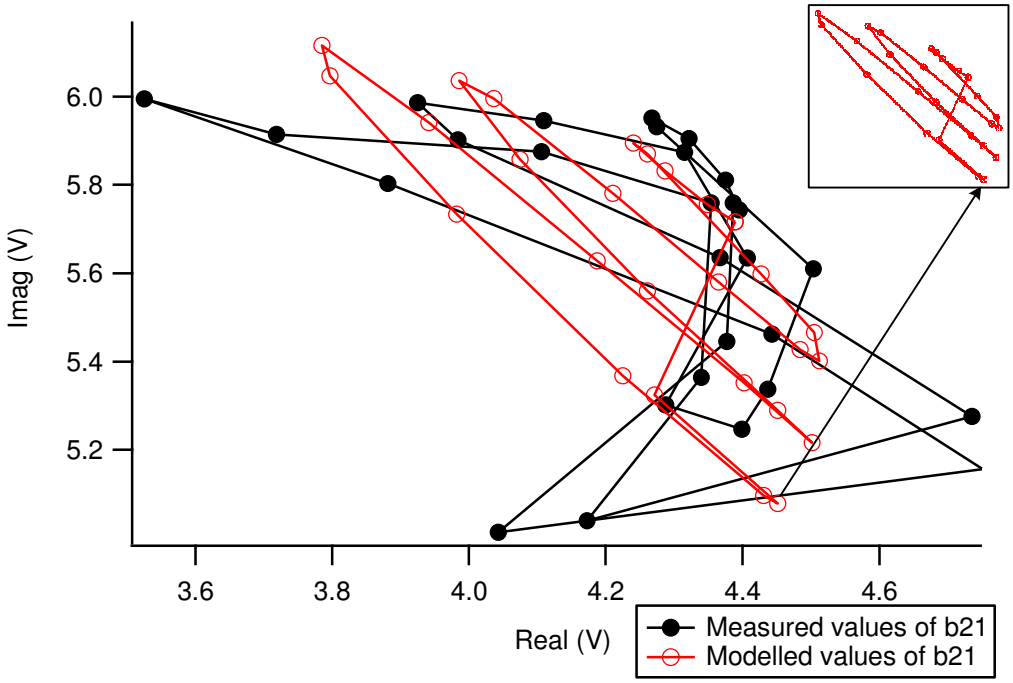

Figure IV-6: Measured versus modelled b_{21} responses from a set of harmonic source- and load-pull measurements.

Figure 6 shows the b_{21} measured and modelled responses for a model including the magnitude squared term:

$$b_{2,1} = R_F|a_{1,1}| + R_S(a_{1,2}) + R_T(a_{1,2}^*) + R^2|a_{1,2}|^2 \quad \text{(V-6)}$$

This has the effect of stretching out the spiral, as the model has a quadratic dependence on $|a_{12}|$.

Figure 7 illustrates further model progression toward the measured response. It should be noted that the other b-wave models only improve in accuracy along with the b_{21} response.

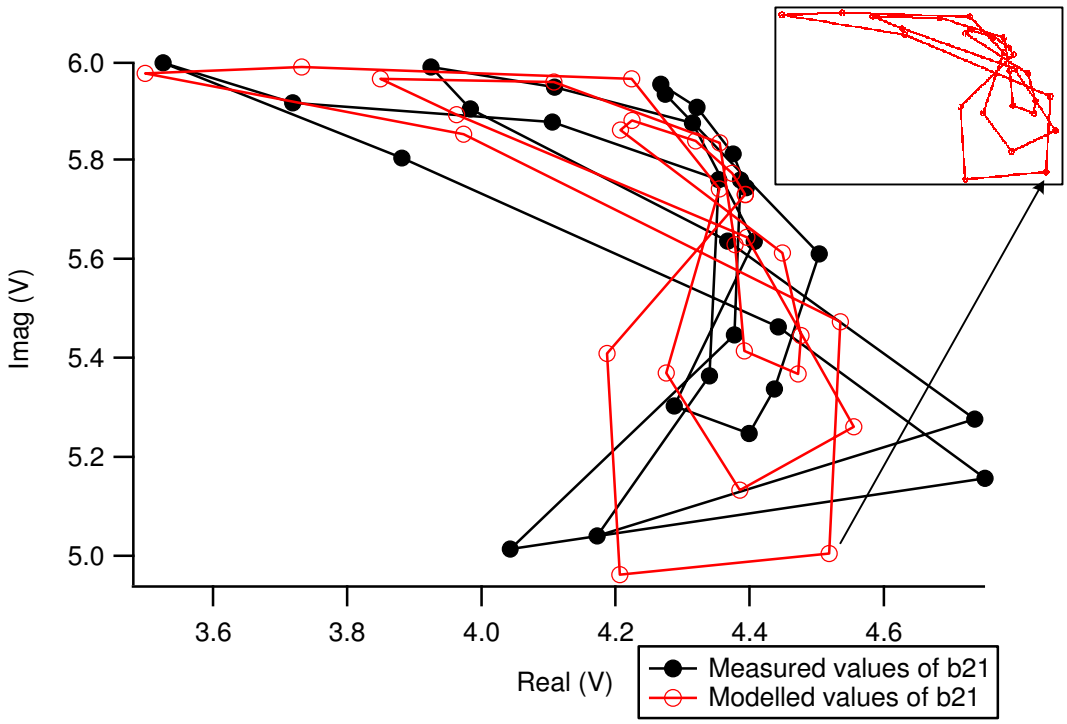

Figure IV-7: Measured versus modelled b_{21} responses from a set of harmonic source- and load-pull measurements.

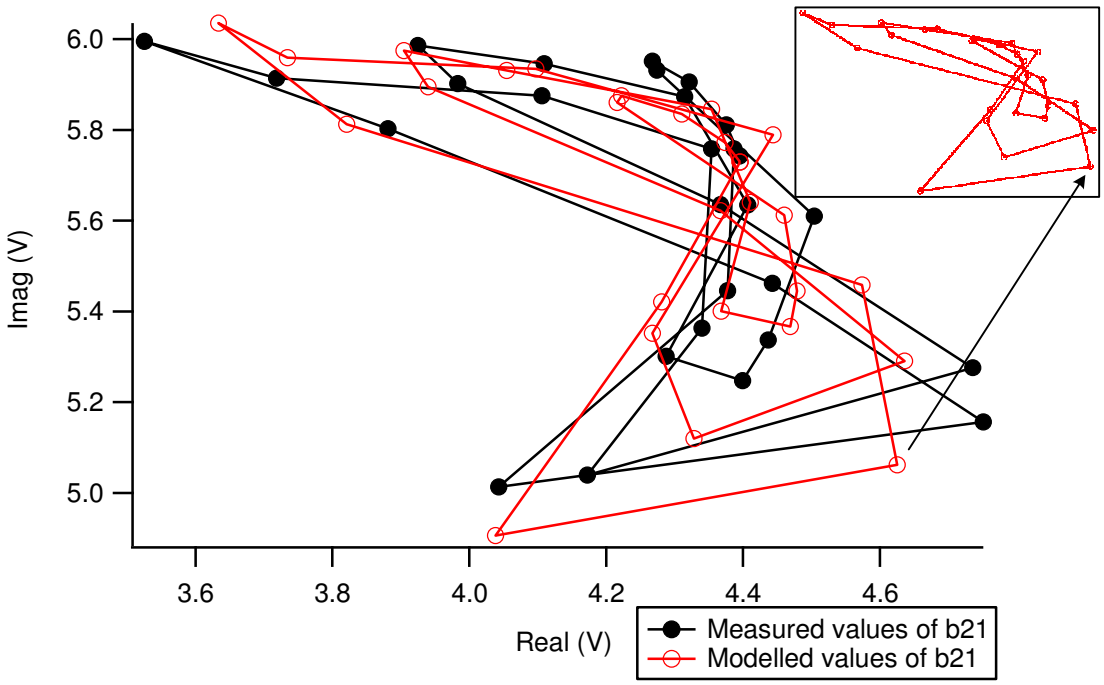

Figure IV-8: Measured versus modelled b_{21} responses from a set of harmonic source- and load-pull measurements.

Figure 8 represents the model fit for the following formulation:

$$b_{2,1} = R_F|a_{1,1}| + R_S(a_{1,2}) + R_T(a_{1,2}) + R^2|a_{1,2}|^2$$

$$+R_S^2(a_{1,2})^2 + R_T^2(a_{1,2})^2 + R_S^3(a_{1,2})^3 + R_T^3(a_{1,2})^3 \quad \text{(V-7)}$$

The model error for increasing model complexity is shown in figure 9. It can be seen that the maximum model error reduces almost linearly until iteration 4 where error reductions plateau. The average error improves the most when the squared phase coefficients are introduced (R_S^2 and R_T^2) on the 3rd iteration, at this point the error has halved. Further model iterations past 3 do not yield as

significant reductions in error. These iterations only act to increase the phase model complexity i.e. increase the indices 'n' of the R_S^n and R_T^n terms.

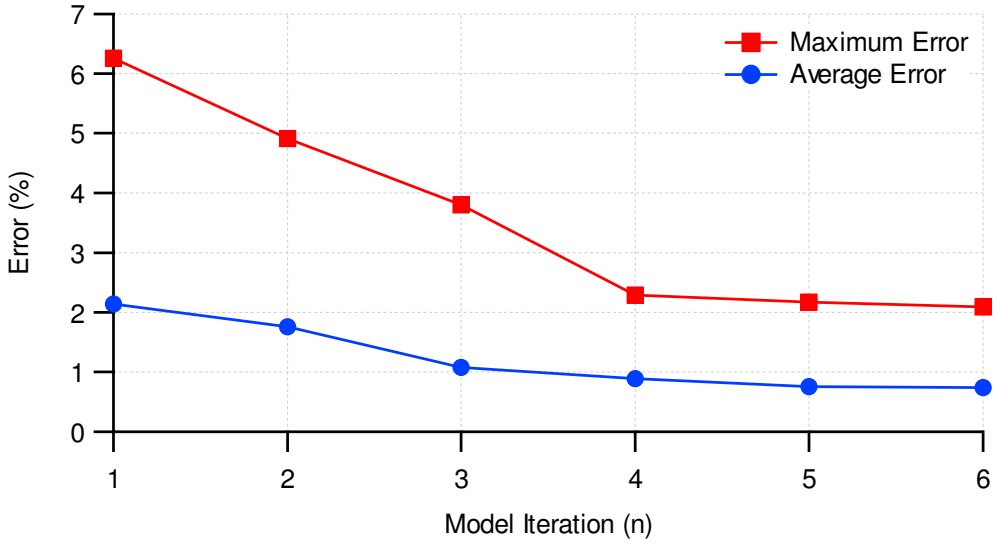

Figure IV-9: The maximum (red) and average (blue) b_{21} model error.

From the error plot and the previous model fit plots it can be seen that a model should be chosen to reflect a quadratic or cubic phase variation, as increases in model complexity provide diminishing reductions in model error.

5.3.3 Input Second Harmonic Mixing Model

The task now is to decide whether there is a need for harmonic mixing between the input second harmonic and output fundamental models. Even a two harmonic output X-parameter model does not require mixing products, although the work by Woodington et al [1-3] has shown that it improves model accuracy. If there was no need for

mixing it would improve the compactness of the model and hint that further harmonic additions might also constitute coefficient addition.

The output fundamental model has been investigated in previous work; therefore it suffices for this work to state that an output fundamental that is quadratic in magnitude and phase was found to model the fundamental b_{21} response correctly, to a confidence of 99.60% at the highest b_{12} power level.

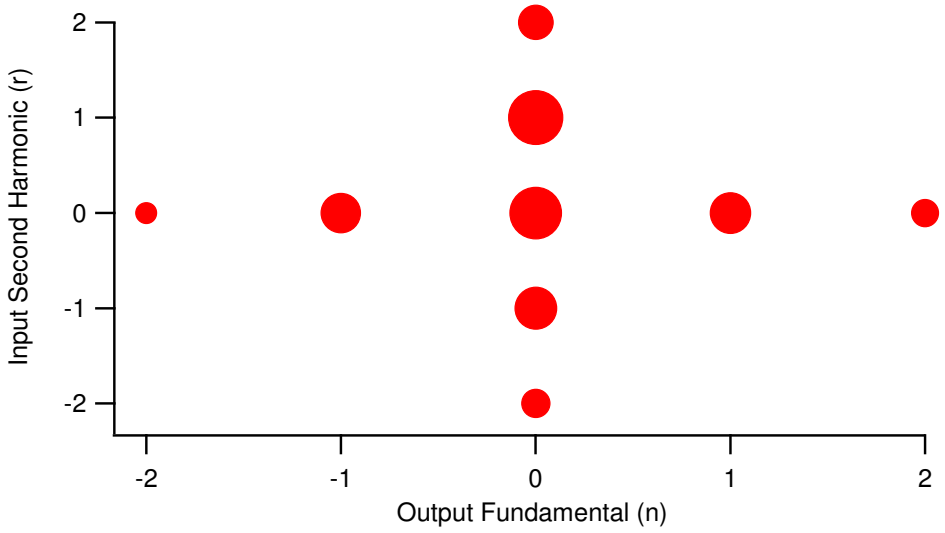

Figure IV-10: The output fundamental and input second harmonic coefficient space.

Figure 10 shows the coefficient distribution if the separate models for the output fundamental and input second harmonic are added together. With this distribution no mixing is taken into account,

therefore its ability to model the data can be analysed. There are actually 11 coefficients in the figure. Two are not visible as they stack at the (0,0) location. These terms are the ones concerning the quadratic variation with the magnitudes of a_{12} and a_{21}, therefore have no phase component and can only reside at the (0,0) location.

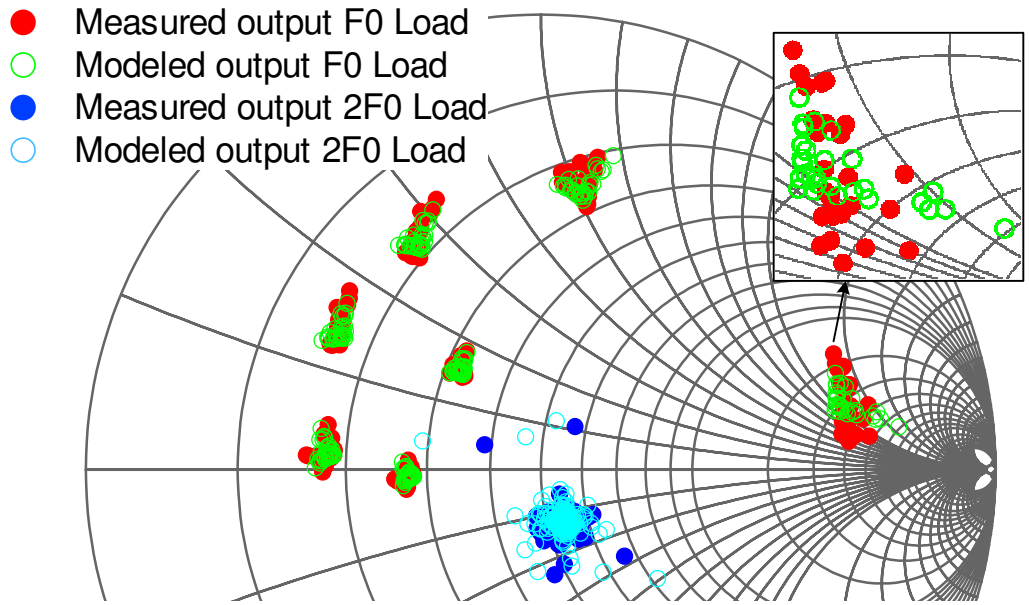

Figure IV-11: The output fundamental (red) and second harmonic (blue) load space.

Figure 11 shows the measured output fundamental and second harmonic loads overlaid with the modelled loads. This figure shows fair agreement of the fundamental loads at low mismatches; however this becomes worse for larger mismatched conditions.

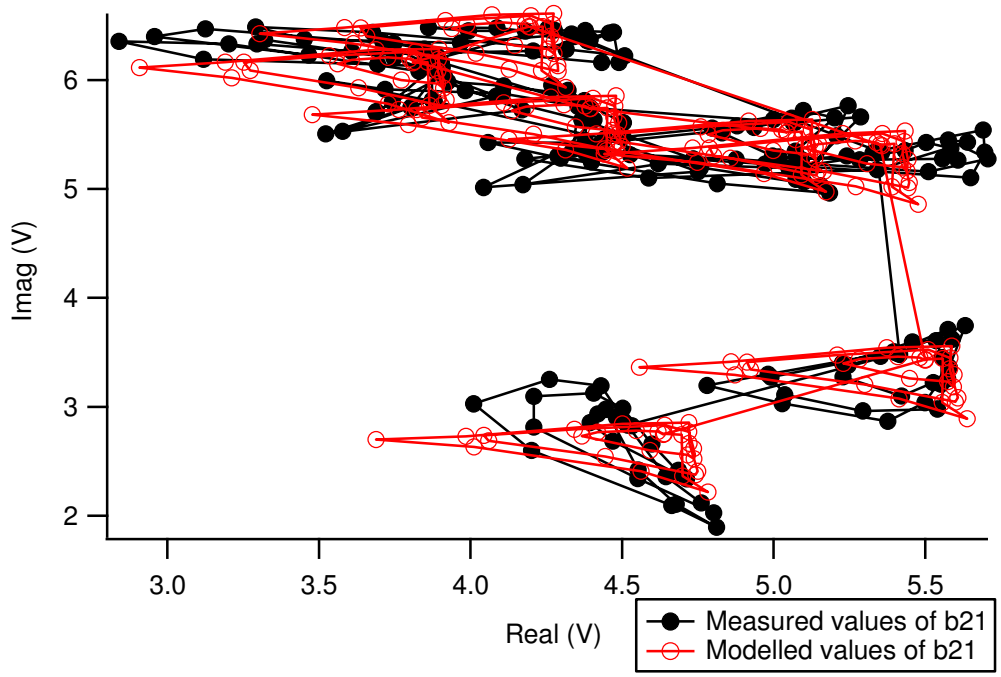

Figure IV-12: Modelled versus measured b_{21} responses.

The difference in fit can be better observed in figure 12, as here the general location of each cluster of points is good. The orientation of the clusters is the same for the modelled trace, however the measured points show rotation occurring.

Table V-1: Additive Coefficient Model Errors

Response	Average (%)	Maximum (%)
$b_{1,1}$	0.97	6.15
$b_{1,2}$	1.95	13.22
$b_{1,3}$	6.65	32.26
$b_{2,1}$	1.91	7.54
$b_{2,2}$	8.38	26.65
$b_{2,3}$	10.75	46.29

This difference from the measurements is reflected in the model errors, as the average b_{21} error is nearly 2% and the maximum error is 7.54%. For comparison, the errors in figure 9, for the X-parameter iteration for the model, show and average error of 2.14% and a maximum error of 6.26% this response is depicted in figure 5, where the modelled trace is quite different from the measurements. All responses suggest that improvements could be made by extracting a mixing model.

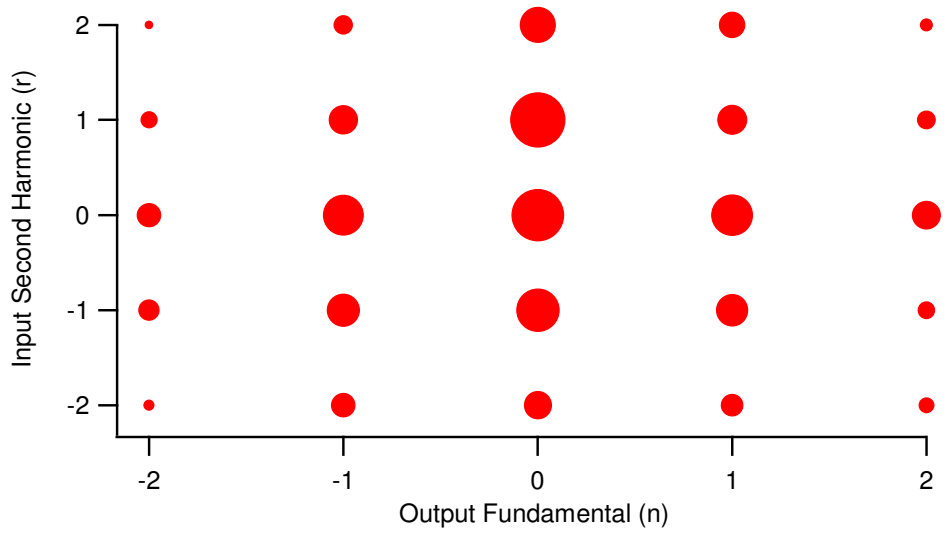

Figure IV-13: The output fundamental and input second harmonic coefficient space.

Figure 13 shows the coefficient distribution that accounts for mixing of all coefficients, it should be noted that here there are 36 coefficients compared to the 11 before. The observed model fit in figures 14 and 15 is noticeably better than before. Figure 14 shows

improved impedance comparison and figure 15 shows that now the rotation of the point clusters has been described by the model.

When comparing figures 12 and 15 it should be clear that correct point cluster orientation was what was going to arise from mixing the coefficient sets. Since both the shapes of the individual $b_{1,2}$ and $b_{2,1}$ responses had been modelled by their respective model coefficients; the missing element was orientation or rotation.

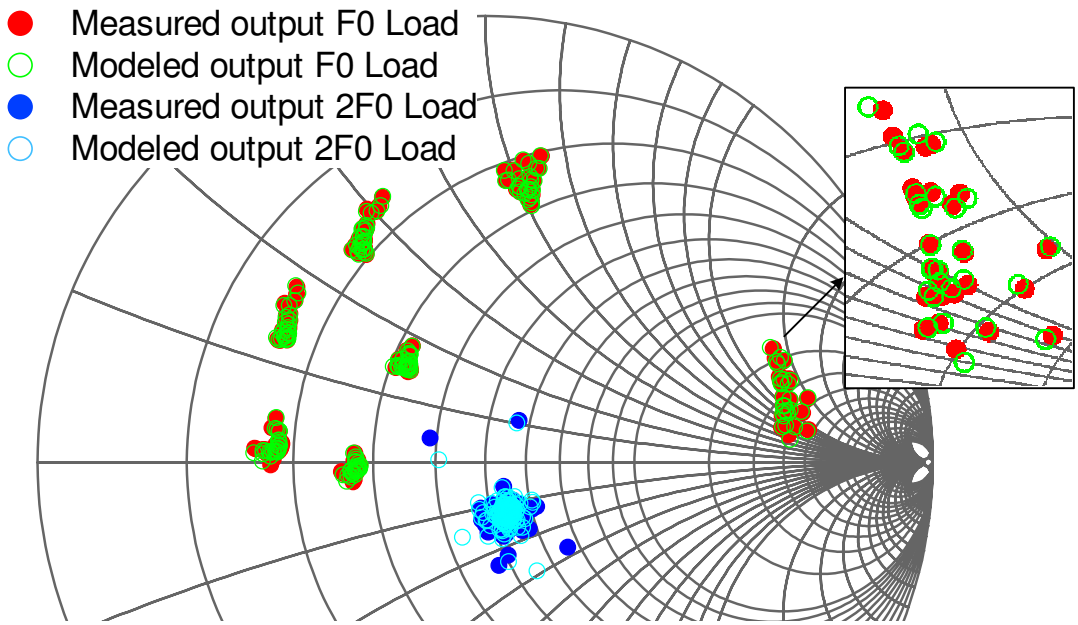

Figure IV-14: The output fundamental and second harmonic load space.

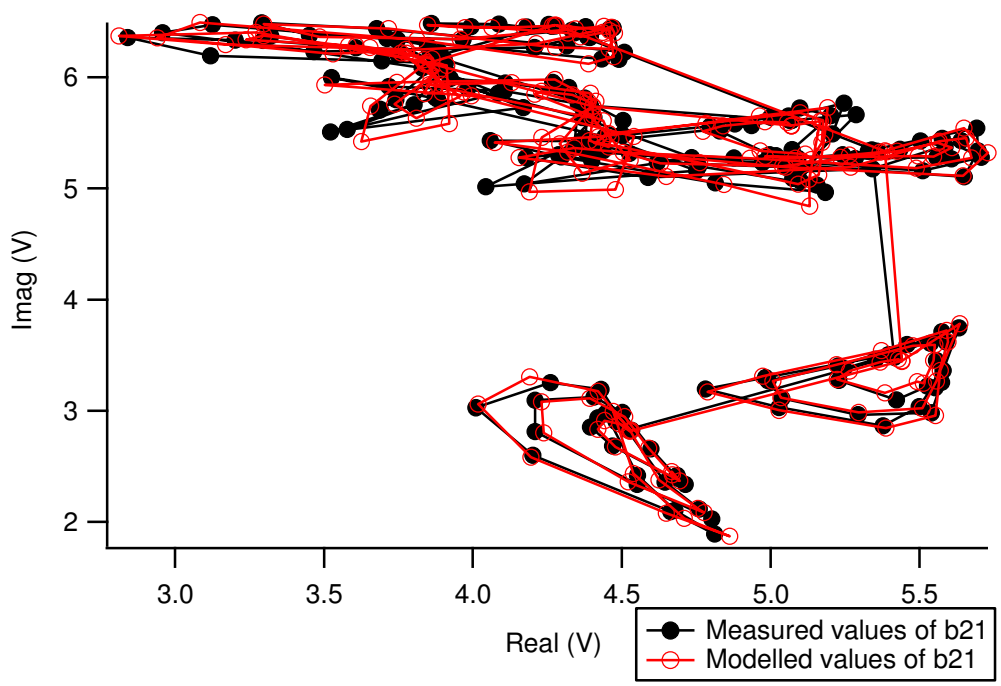

Figure IV-15: Modelled versus measured b_{21} responses.

Table V-2: Mixing Coefficient Model Errors

Response	Average (%)	Maximum (%)
$b_{1,1}$	0.26	1.03
$b_{1,2}$	0.55	2.12
$b_{1,3}$	1.76	7.27
$b_{2,1}$	0.59	4.48
$b_{2,2}$	2.43	16.38
$b_{2,3}$	2.43	11.65

Table 2 shows good improvements in all of the harmonic responses, particularly the reduction of all the maximum errors from table 1. However, although the model fit is good the downside to modelling like this is the number of coefficients needed. Gains in model accuracy are achieved when going from the coefficient distribution shown in figure 10, of 11 coefficients, to the one in figure 13, with 36

coefficients. Therefore, these accuracy gains are not wholly bolstered by the increase in model complexity, as ultimately an increase in model complexity produces an increase in model file size. If the desired model is to cover sets of bias, frequency, and power data an increase in model complexity will be multiplied by the amount of measurements in the bias, frequency, and power data when it comes to the file size. When viewed from this perspective it can be seen that the application to which the model is being used is also key in determining the complexity of the model. Therefore, it is not recommended that full mixing of coefficients be performed for models measured over many harmonics for multiple operation levels. In these cases mixing truncation can be performed on high order mixing terms to reduce the overall amount of coefficients needed whilst preserving model accuracy.

5.3.4 Higher Harmonic Mixing

There are observable matches between measured and modelled data sets in the above case when mixing was taken into account. However, it is hoped that higher harmonic mixing products can be ignored since this would result in a more compact model file for three or more harmonic models. To investigate higher harmonic model interactions extensive measurements were performed with fixed bias, frequency, drive power, and a_{21}; perturbations were made with a_{12} and a_{21}.

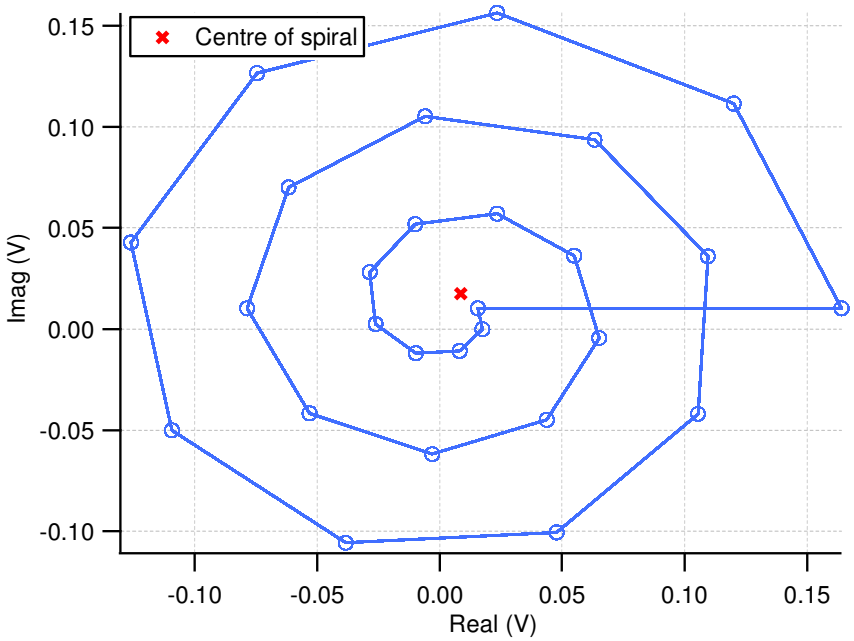

Figure IV-16: The $a_{2,2}$ stimulus points at 18GHz in the complex plane.

Both a_{12} and a_{21} spirals were offset towards a short circuit as this is where best efficiency can be achieved, hence is the most important impedance area. Figure 16 shows the $a_{2,2}$ spiral and is representative of all the perturbation grids in this chapter. A spiral similar to figure 16 was also use for the $a_{1,2}$ perturbations.

By isolating the $a_{1,2}$ and $a_{2,1}$ signals and creating models for them separately, it was found that both could be modelled by a coefficient distribution that was quadratic in phase. The mixed coefficient distribution is shown in figure 17.

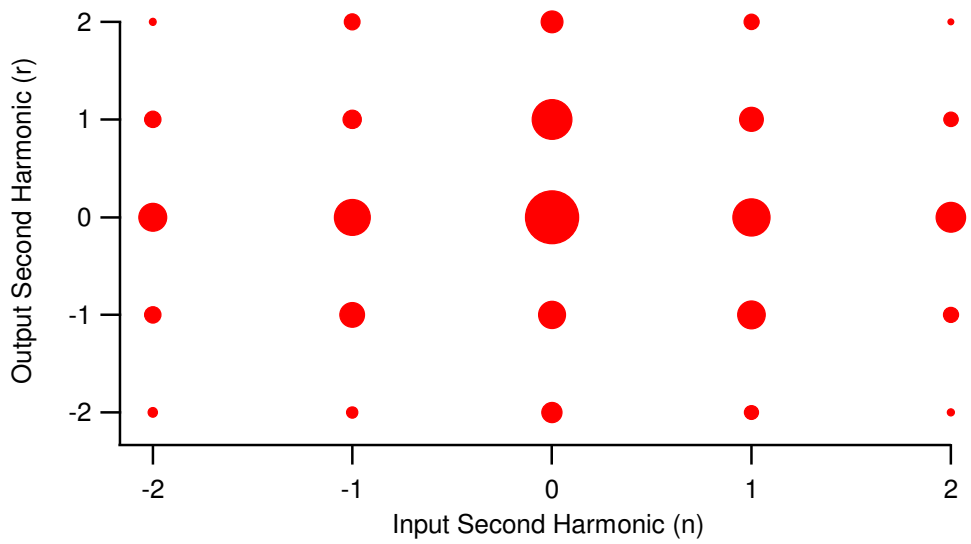

Figure IV-17: The input second harmonic and output second harmonic coefficient space.

Figure 18 shows the resulting $b_{1,2}$ model fit against the measured data for the mixed coefficient distribution and table 3 shows the associated average and maximum errors for all the harmonics. The modelled point clusters in figure 18 are very well matched to the measured data this is corroborated by the low average and maximum errors for $b_{1,2}$ in table 3. It should be noted that point clustering like this is a result of performing nested measurement sweeps. Interestingly, figure 18 shows that the $a_{2,2}$ injection results in small perturbations of the $b_{1,2}$ spiral points.

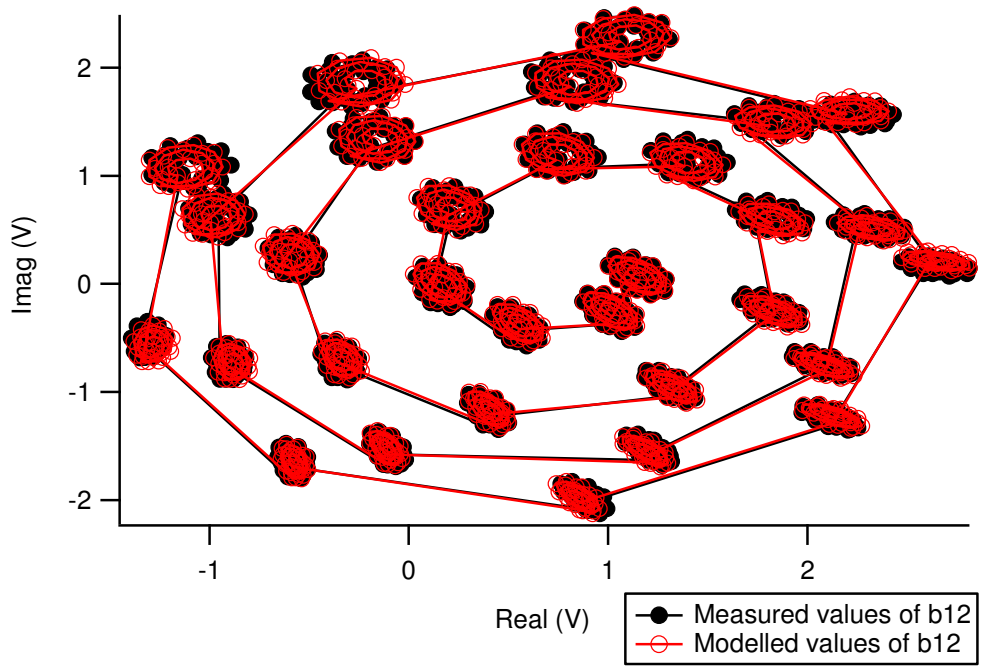

Figure IV-18: The $b_{1,2}$ modelled versus measured responses.

TABLE V-3: Mixing Model Errors

Response	Average (%)	Maximum (%)
$b_{1,1}$	0.56	2.26
$b_{1,2}$	0.68	2.77
$b_{1,3}$	2.45	8.71
$b_{2,1}$	0.31	1.08
$b_{2,2}$	2.60	10.41
$b_{2,3}$	2.01	8.84

Figure 19 shows the $b_{1,2}$ fit for the additive coefficient distribution. It is obvious here that the two harmonics cannot just be treated separately, therefore the mixing rationale holds. The large average and maximum errors are not satisfactory and so modelling with an additive coefficient distribution resulted in a skewed model fit.

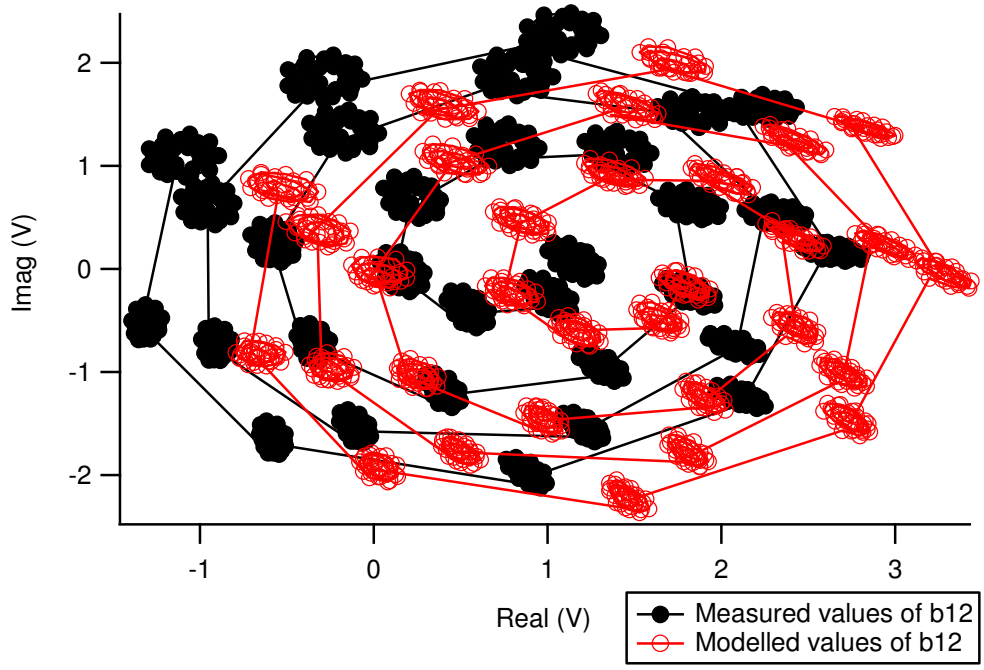

Figure IV-19: The $b_{1,2}$ modelled versus measured responses.

TABLE V-4: Additive Model Errors

Response	Average (%)	Maximum (%)
$b_{1,1}$	84.84	94.07
$b_{1,2}$	27.24	42.68
$b_{1,3}$	15.73	38.17
$b_{2,1}$	84.81	90.54
$b_{2,2}$	37.73	108.00
$b_{2,3}$	76.16	105.59

Table 4 shows the errors for the harmonics and, as expected, all other harmonics corroborate the bad model fit that is displayed in figure 19.

If the model interactions between the output fundamental and input second harmonic, and the input second harmonic and output second harmonic are compared, it can be seen that the output second harmonic is more sensitive to variations of the input second harmonic. It is suggested that this relationship will also extend to higher harmonics, where ultimately there is probably little interaction with the input and output n^{th} harmonics and the fundamental but large interaction between the input and output n^{th} harmonics. In terms of coefficient distributions this would suggest that the fundamental and n^{th} harmonic interactions would be characterised by additive coefficient distributions and n^{th} harmonic interactions would need mixing coefficient distributions for them to be modelled accurately.

5.4 OVER DETERMINATION OF HARMONIC AND DC DATA

The models created up to this point have treated all the harmonics the same. Therefore, if a mixing model, between the fundamental output and input second harmonics, required 36 coefficients to correctly describe the mixing and nonlinearities then those coefficients were used to model DC as well. The issue here is that the unrelated harmonics, in terms of mixing, may not need such complexities in order to be modelled correctly. The reduction in total coefficients will also reduce the model file size, which is a nice by-product.

There are two ways to re-determine the separate harmonic model coefficients. The first would be to simply truncate the existing determination of the model by replacing the least important coefficient results by zero. The second would be to truncate the coefficients before their calculation and then recalculate the specific, changed, harmonic models according to the new coefficients.

To compare the two methods, using isolated measurement data from the previous section, an input second harmonic spiral of data points will be modelled; firstly, by the truncation method, and then by the recalculation method. The model errors can then be compared against each other and the errors of a six coefficient model. The level to which the DC and third harmonic components will be truncated represents the maximum recommended truncation. The DC components ($b_{1,0}$ and $b_{2,0}$) will be modelled by only one coefficient and the third harmonic components will be modelled by the X-parameter coefficient set. The measurement data being used is for an output fundamental and input second harmonic model; the input second harmonic response has been isolated for the test. This means that truncations and recalculations should be performed on the DC and third harmonic components, as these have weakest correlation to the measurements that were performed.

Tables 5, 6, and 7 show the errors for the original 6 coefficient model, the model after it has been truncated at DC and the third harmonic, and the model with the recalculated coefficients. Both the truncated and recalculated models show improvements in the DC components, on both ports, compared to the original model extraction.

TABLE V-5: Model Errors for the 6 Coefficient Model

Response	Average (%)	Maximum (%)
$b_{1,0}$	0.04	0.18
$b_{1,1}$	0.15	0.50
$b_{1,2}$	0.41	1.55
$b_{1,3}$	1.25	3.21
$b_{2,0}$	11.72	14.66
$b_{2,1}$	0.21	0.75
$b_{2,2}$	0.50	1.40
$b_{2,3}$	1.15	5.82

TABLE V-6: Model Errors after Truncation

Response	Average (%)	Maximum (%)
$b_{1,0}$	0.03	0.05
$b_{1,1}$	0.15	0.50
$b_{1,2}$	0.41	1.55
$b_{1,3}$	7.60	28.87
$b_{2,0}$	11.05	11.06
$b_{2,1}$	0.21	0.75
$b_{2,2}$	0.50	1.40
$b_{2,3}$	4.23	18.43

TABLE V-7: Model Errors after Recalculation

Response	Average (%)	Maximum (%)
$b_{1,0}$	0.02	0.04
$b_{1,1}$	0.15	0.50
$b_{1,2}$	0.41	1.55
$b_{1,3}$	5.91	15.16
$b_{2,0}$	11.72	11.74
$b_{2,1}$	0.21	0.75
$b_{2,2}$	0.50	1.40
$b_{2,3}$	4.31	16.32

The $b_{1,3}$ and $b_{2,3}$ errors are clearly worse after truncation and recalculation, however, the average errors are both under 10% and since there was no effort to control the third harmonic this error would not constitute to huge differences between modelled and measured I-V waveforms. Large maximum errors in the uncontrolled harmonics usually arise from trying to model noise not very well, therefore, differences in these values constitutes a difference in the model's ability to model the smallest $a_{p,h}$ in the dataset. The difference between the truncated and recalculated average errors, although small, shows that the over determined model does a good job of modelling the R_F, R_S, and R_T components for DC and the third harmonic respectively. However, if it is necessary to preserve accuracy then the recalculation method is suggested.

The same principles can be applied to mixing models with the potential of producing less error in the uncontrolled model responses. This is by virtue of the little importance higher order terms have in the power series, unless harmonics interactions are strong, therefore removing them would do little to model errors.

5.5 HF Amplifier Design and Measurement Implications

The source- and load-pull measurements thus produced an improved model implementation within CAD, that allow for detailed

analysis ("data mining"), from an amplifier design perspective, of the GaAs pHEMT device. It was known from [5] that gains in PA efficiency can be achieved by manipulating the input second harmonic of a device. In an effort to explore these phenomena at X-band, and test the model extraction and CAD implementation, the resulting model from the input second harmonic and output second harmonic mixing model, measured about Class-B impedance areas, was used in ADS.

To better understand where any efficiency gains are coming from in the Class-B waveforms, the theory outlined in [6] will be used. Since waveform analysis is to be used, the model needs to accurately describe the harmonic nonlinearities in the I-V waveforms.

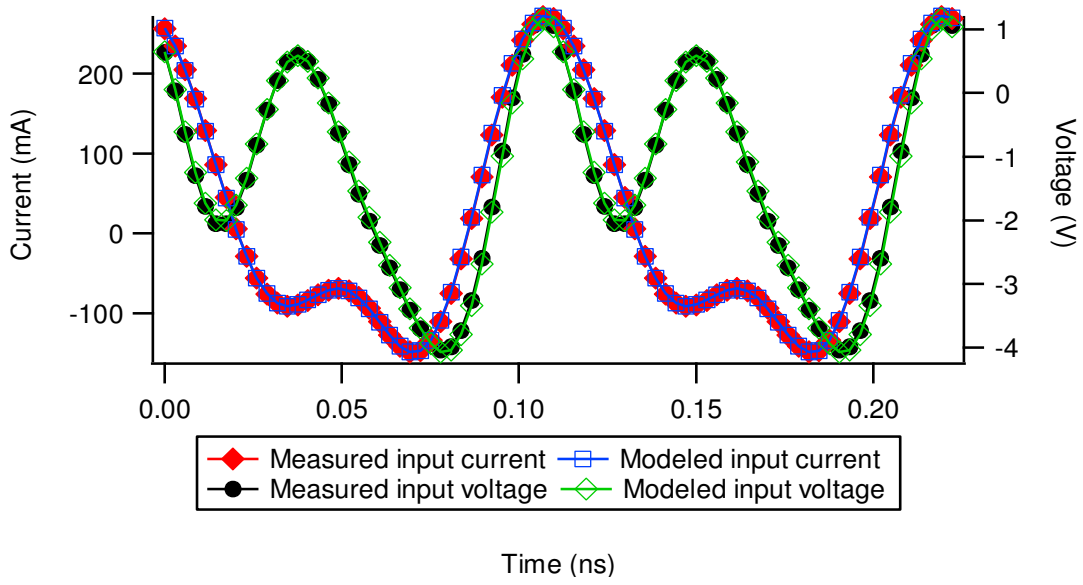

Figure V-20: Input measured and modelled I-V waveforms.

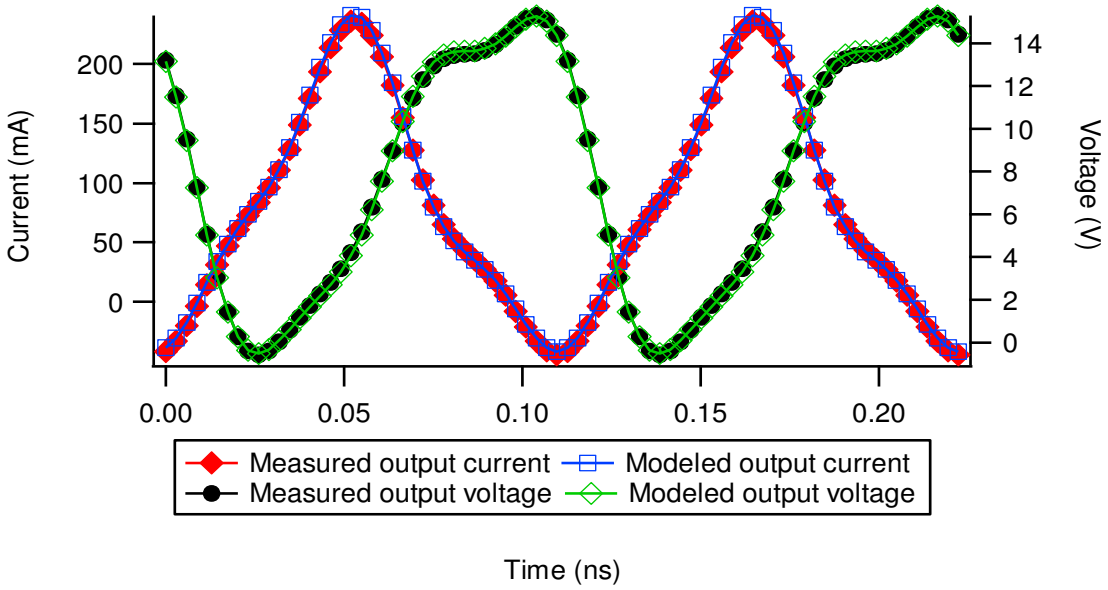

Figure V-21: Output measured and modelled I-V waveforms.

Figures 20 and 21 show a single input and output current and voltage waveform instance of the measurement results with the modelled waveforms overlaid. In both traces the modelled waveforms are almost exact replicas of the measurements, which were the case for all instances of measured waveforms, thus validating the models capability of replicating measured waveforms.

The measurements alone were not positioned well enough to analyse certain conditions that arise when manipulating the input second harmonic about its short circuit point. The conditions in question were an extrinsic input second harmonic short circuit, an intrinsic input second harmonic short circuit, and input second harmonic impedance that would half rectify the input voltage at the intrinsic

plane. Therefore, in order to investigate these conditions, a model was imported to ADS and simulations were performed.

Table V-8: Fundamental and Second Harmonic Model Errors.

Response	Average (%)	Maximum (%)
$b_{1,1}$	0.56	2.26
$b_{1,2}$	0.68	2.77
$b_{2,1}$	0.31	1.08
$b_{2,2}$	2.60	10.41

Table 8 shows the harmonic model errors that pertain to the ADS simulations. The omission of the third harmonic model errors was by virtue of the harmonic balance simulator being set up to observe two harmonic interactions; hence the third harmonic was being ignored on both ports. The waveform analysis was clearer without acknowledging the contributions of the third harmonic.

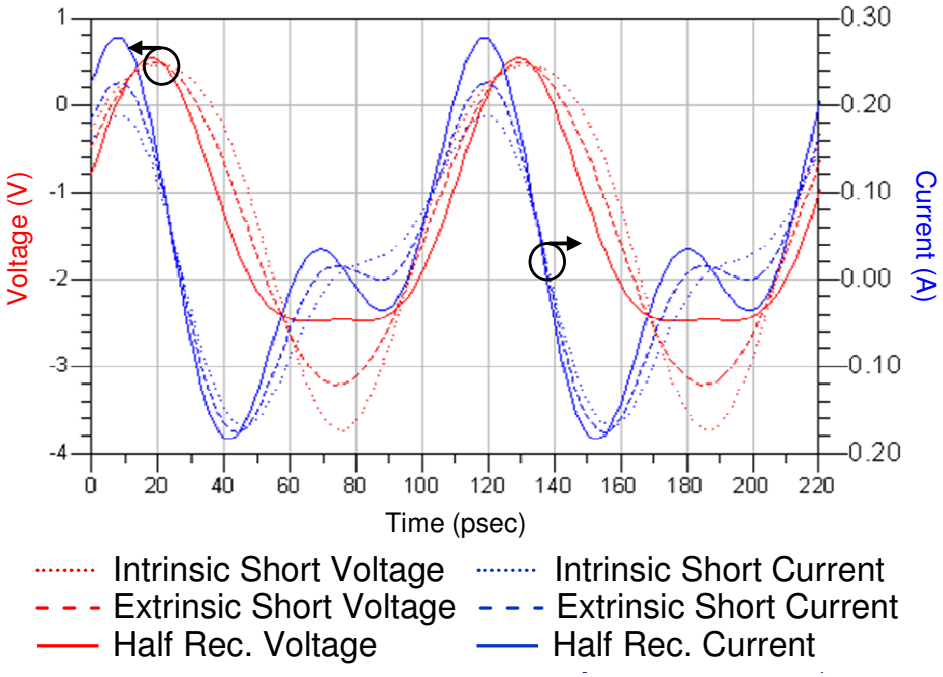

Figure V-22: The simulated de-embedded input I-V waveforms.

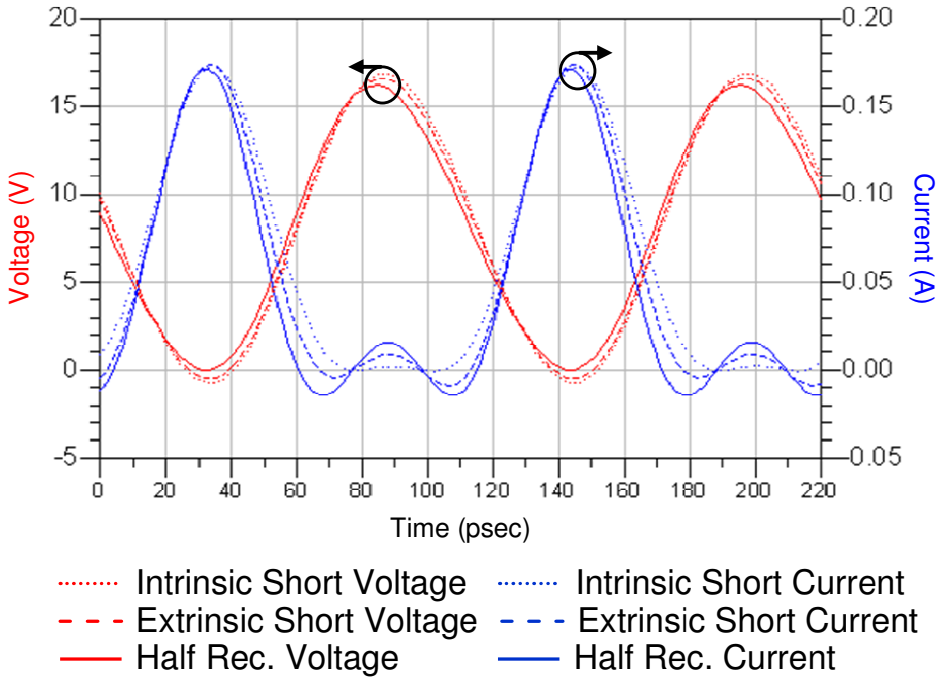

Figure V-23: The simulated de-embedded output I-V waveforms.

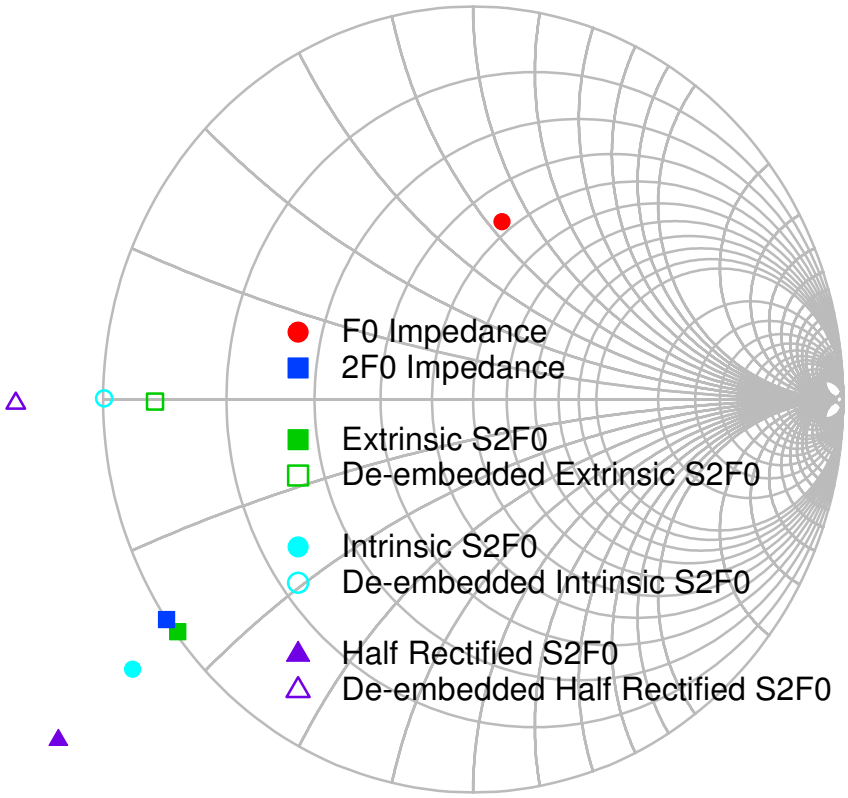

Figure V-24: The simulated input and output impedances.

Figures 22 and 23 show the de-embedded input and output I-V waveforms for the aforementioned conditions. The dashed traces are for the extrinsic input second harmonic short condition, the dotted traces are for the intrinsic input second harmonic short condition, and the solid traces are for the input half-rectified voltage case. Figure 24 shows the simulated input impedances for the three cases as well as the Class-B output impedances for optimum efficiency. The actual impedances that would be seen on a measurement systems' analysis window have been included with the de-embedded input second harmonic impedances to contrast measurement and device planes. It should be noted that the de-embedded half rectified

input second harmonic reflection coefficient was -1.23-j0.009 to achieve the desired input voltage waveform shape.

The three conditions' respective drain efficiencies are 77.31%, 78.72%, and 73.35%. This shows that of the three conditions, the intrinsic short circuit is the best for drain efficiency and that device robustness improvements can be made, by half rectifying the input voltage waveform and reducing the voltage swing, without compromising too much in efficiency. The output power range for the three cases was 25dBm ±0.5dBm.

The intrinsic output waveforms look very similar to ideal Class-B output waveforms. The other cases' variations away from the ideal are reflected in the loss in drain efficiency. It should be noted that theses waveforms cannot be obtained under normal load-pull conditions, with the input second harmonic at 50Ohms, therefore one would not be able to observe efficiencies from devices measured at X-band that are in accord with the theoretical predictions without source-pull. Implementing an input second harmonic short circuit via a stub on a test MMIC (Monolithic Microwave Integrated Circuit) structure would be a way to aid measurement, for future output investigations, and would enable three harmonic load-pull by releasing a source. In the future it would be good to perform

investigations into the breakdown of ideal Class-B waveforms as the operation frequency is increased and how to combat it with input second harmonic impedance tuning.

5.6 SUMMARY

This chapter has detailed the rationale behind conducted model measurements, the model extraction, and model filtering or truncation. The measurement of the models needed to be addressed since fundamental analysis about the created model's relationships to the model order had been performed in earlier work. This allowed for magnitude and phase variance in the measurements of the model. The corollary of this is that spirals, instead of offset circles, could be used. This measurement approach reduces the total number of measurements needed to cover an impedance area of interest for a particular harmonic. The measurement reductions, i.e. time reductions, for model sweeps over many harmonics are multiplicative, which is favourable for the generation of model for more complex data.

In order for there to be proper analysis of the input second harmonic models, there was an issue concerning model formula augmentations that had not previously been addressed that needed to be investigated. In previous work, asymmetric coefficient distributions

were allowed when gains to mode accuracy were sufficient. However, no comparison of what happened at DC, with symmetric and asymmetric coefficient distributions, was performed. The data clearly shows that, at both the input and output ports, asymmetric model coefficient distributions lead to non-cancelling imaginary components at DC, whereas the imaginary components at DC produced by symmetric coefficient distributions were complex conjugates and therefore cancelled.

The characterization of the input second harmonic model from measurement data obtained from a GaAs pHEMT was performed, at first, with it in isolation and then model mixing phenomena were assayed. The comparison of the input second harmonic model's minimum and maximum errors showed that a plateau in error reductions at around the 3rd or 4th model formula expansion. These constituted models, describing the response of the input second harmonic, with a quadratic dependency in magnitude and a quadratic (3rd expansion) or cubic (4th expansion) dependency in phase. Due to the gains in average model error being more important than gains in maximum model error, and having a tendency toward models with reduced complexity, the input second harmonic model was created with a quadratic phase dependency.

Input second harmonic and output harmonic mixing was, at first, hoped to be negligible. The results from testing a model with additive harmonic coefficients, for the input second and output fundamental, did not reflect this initial hope. The shape of the $b_{2,1}$ response in figure 12, in terms of the output fundamental model, was good. The point clusters in the response, defined by the input second harmonic model, were good too. However, they were misaligned and did not exhibit similar rotation to the measured $b_{2,1}$ response. A full mixing model was created and the model fit was observably better, however, the gains in model complexity were not bolstered by the reductions in model error. As such, it would be acceptable to perform some filtering on the fully mixed model, keeping a symmetric coefficient distribution, as a compromised solution preserving model accuracy without overly increasing model complexity.

The investigations into model mixing phenomena between the input and output second harmonic components yielded a similar result as above. The additive coefficient model manifested a shift in the $b_{1,2}$ trace that was clearly rectified by the introduction of a fully mixed model. In this case, the average model errors for the $b_{1,2}$ and $b_{2,2}$ responses were improved by over a factor of ten. There was a clearly indicated sensitivity between harmonic components at the same frequency, whereas fundamental sensitivities were comparably less.

The over determination of harmonic and DC data occurs every time a model is created. This is because, until now, there has been no truncation applied to the model. The truncation method was divided into two: first, unnecessary coefficients could be replaced by zeros; second, the harmonic models could be recalculated at the desired model order then the removed coefficients could be padded with zeros after calculation. Comparison between original, truncated, and recalculated model errors showed that the DC component errors improved for both truncations however the third harmonic component errors worsened. The increase in third harmonic errors was not necessarily a significant issue due to the third harmonic, in this case being very small, hence exhibiting minimal effects on the I-V responses. However, behavioural models for amplifier modes that clearly utilize the third harmonic would not have this truncation performed. The effects of the truncations would be less for mixing model cases due to coefficients, representing high orders of non-linearity, and mixing at uncontrolled harmonic components, having ever decreasing effects on the I-V responses.

The position, on the Smith Chart, of the model measurements allowed for more than just model analysis to be performed. Simulation of three input second harmonic impedance cases, with optimum Class-B output load impedances, was undertaken to investigate improvements of drain efficiency, and to exercise the

dynamic CAD implementation. To be able to analyse the I-V waveforms, it was found that removing the third harmonic component unveiled waveforms close to theory. The comparison of the drain efficiencies showed that and intrinsic short circuit produced the best drain efficiency, 78.72%, and that only small reductions in efficiency would occur if the input voltage waveform was half-rectified to improve device robustness. The measurement implications, of measuring in a 50Ohm system rather than shorting the input second harmonic, were made apparent, as it would be impossible to recreate waveforms observed at lower frequencies. The results obtained represent state of the art X-band performance comparable with device performance at lower frequencies and are only obtainable through input waveform engineering. Therefore future measurements would require a shorted input second harmonic component either by source-pull or by the fabrication of an appropriate MMIC test structure.

5.7 REFERENCES

[1] S. Woodington et al, "A Novel Measurement based Method Enabling Rapid Extraction of a RF Waveform Look-Up Table Based Behavioural Model," IEEE MTT-S International. Pg 1453-1456. Jun 2008.

[2] S. Woodington et al, "*Behavioural Model Analysis of Active Harmonic Load-Pull Measurements,*" IEEE MTT-S International. Pg 1688-1691. May 2010.

[3] S. Woodington, "*Behavioural Model Analysis of Active Harmonic Load-Pull Measurements,*" Doctoral thesis submitted to Cardiff University. 2012.

[4] R. S. Saini, "*Intelligence Driven Load-pull Measurement Strategies,*" A Doctoral Thesis submitted to Cardiff University. 2013.

[5] P. Colantonio, F. Giannini, E. Limiti and V. Teppati, "*An Approach to Harmonic Load- and Source-Pull Measurements at X-Band,*" IEEE Transactions on Microwave Theory and Techniques, Vol. 52, No 1, Jan. 2004.

[6] S. Cripps, "*RF Power Amplifiers for Wireless Communications*," Norwood, MA: Artech House, 1999.

CHAPTER VI
CONCLUSIONS AND FUTURE WORK

The work presented in this thesis has covered the processes involved in a measurement-to-CAD modelling cycle, whilst also providing key analysis of input and output harmonic model interactions. Although the past and present modelling techniques, from S-parameters to the Cardiff Model, are unquestionably linked, the Cardiff Model has its place at the forefront of current behavioural modelling trends. This thesis has realised behavioural models that consider the interactions between the input and output harmonics, and outlined the necessary framework in order to develop and augment said models. The development of the measurement system and improvements to past model implementations have been included to show the necessary steps for the measurement and simulation of input and output harmonic models. Without a developed measurement platform and dynamic model implementation

in CAD, measurement and analysis of the mixing models would not have been possible.

6.1 CONCLUSIONS

The investigations into input second harmonic modelling and the model's interactions with output harmonic models have conveyed its limits and have shown that the modelling process is application specific. Each chapter has had its conclusions raised and here they will be highlighted.

Chapter III details the design of a coherent carrier system. In the testing phase it was observed that upon measurement of some points in a multi-harmonic grid, the PSG attached to port 4 of the system became unlocked. This was, in part, due to the variation of the internal workings of the HCC options across the PSGs, and variation in the carrier distribution system's cable attenuation, but mainly due to a non-ideal input power to one of the system PAs. The problem was rectified by reducing the attenuation at the input of the system by 1dB. The coherent carrier distribution system overcame the frequency selectivity of the previous implementation and allowed for the first time harmonic load-pull measurements to be performed at X-band. Although the coherent carrier distribution system was fit for purpose future measurement system augmentations would not be

accommodated. This setback promotes VNA measurement solutions where four port (source) analysers are standard.

Chapter IV outlines the procedure taken to improve the CAD implementation of the Cardiff Model. Although the fundamental components in ADS, the FDD and DAC component, have not changed the formulaic and function structure has been transformed a lot. The implementation now uses the simple matrix equation [B] = [R] x [A] to calculate the system response for any type of model or harmonic complexity. To be able to use such a simple formula, the schematic needs to be populated by an AEL script run from the command line window within ADS. This implementation has significantly improved the model implementation's usability, whilst also overcoming the challenges of dealing with different model complexities.

Chapter V addresses augmentations to the model formulation, from which it is clear that additions to the formulation must consist of a model parameter and it's conjugate. Furthermore the chapter clearly highlights saturation of model accuracy for the addition of parameters that imply higher than cubic phase dependency. Therefore a model with cubic phase dependency is considered the most complex model that would be necessary for an isolated measurement harmonic. The analysis of mixing models has shown

that they are beneficial for input second harmonic mixing with both the output fundamental and output second harmonic. However, despite the gains in model accuracy, filtering of the coefficient distributions would be necessary for more complex measurement scenarios, for example: the measurement of the Class-F amplifier mode. The filtering would be necessary to reduce mode file size, which ultimately will help the simulator. Since high order mixing terms have diminished effects on model accuracy their removal would result in a slight decrease in model accuracy. Finally, through simulation of impedance conditions about a short circuit, it is concluded that to be able to measure device performance, at X-band, in accord with theory and comparable to performance measured at lower frequencies the input second harmonic must be presented with a short circuit. This can be achieved by engineering the input waveform through the design of MMIC test topologies or by performing source-pull.

6.2 FUTURE WORK

The framework for the Cardiff Model has certainly been established for the input and output stimuli. However, there is still much that can be done to bolster previous efforts as well as the developments contained in this thesis. Currently the magnitude of $a_{1,1}$ is an independent variable therefore if variations in the model coefficients, up until $R_{p,h}(a_{p,h}^{*})^{3}$, are observed against variations of $|a_{1,1}|$

mathematical relationships could be defined and hence $|a_{1,1}|$ could be absorbed in the coefficient block leaving just bias and frequency as the independent variables.

The scalability of the model has been investigated in [1], however, that is for device size only. It would be beneficial if the model was scalable over frequency, as models could be extrapolated for measurement scenarios at frequencies not possible with standard industry network analyser systems. The scaling could be realised by contiguous circuitry, to perform the scaling within CAD, or it could be done formulaically.

The CAD implementation demonstrated in this thesis is by no means a final iteration. The approach that has been developed has given an indication to the sort of Netlist file that needs to be written for ADS to use at simulation run-time. The next iteration would only produce a Netlist based on the model file that follows the template of what ADS produces. This would significantly reduce the initial loading time before each simulation of the Cardiff Model, by virtue of there being only one load of a file, the Netlist.

The termination of the input second harmonic impedance into a short circuit showed that efficiency close to theory and results obtained at

lower frequencies, for a Class-B amplifier, could be obtained. This suggests that designing MMIC test structures that short circuit the input second harmonic would allow measurement of device performance representative of theory. The recovery of the waveforms and efficiency, by applying and intrinsic short circuit to the device over frequency, can be investigated to better demonstrate the need for MMIC test structures when measuring at X-band.

6.3 REFERENCES

[1] M. Koh et al, "X-band MMIC Scalable Large Signal Model based on Unit Cell Behavioral Data Model and Passive Embedding Network," Selected for presentation at IMS 2013.